# Development of novel imaging technology to study cell signalling

## Bing Li



Supervisor: David Klenerman

Department of Chemistry

University of Cambridge

This dissertation is submitted for the Doctor of Philosophy

October 2022

Downing College

# Declaration of Authorship

I, Bing Li, declare that this thesis titled, 'Development of novel imaging technology to study cell signalling' and the work presented in it are my own. I confirm that: This dissertation summarises research carried out in the laboratory of Professor David Klenerman at the Department of Chemistry, University of Cambridge, between October 2018 and October 2022. The work described in the dissertation is my own. It is not substantially the same as any that I have submitted for a degree or diploma or other qualification at any other University and no part has already been, or is concurrently being, submitted for any degree, diploma, or other qualification. The length of this dissertation does not exceed the word limit of the degree committee.

Signed:

Date:

# Abstract

# Development of novel imaging technology to study cell signalling

# Bing Li

Currently it is difficult to study signalling on living cells at the single molecule level. One problem is that it is not possible to trigger signalling in a controlled manner and there is no effective method that can both introduce a precise amount of molecules onto or into a single cell at a specific position and then simultaneously image the cellular response using single molecule fluorescence. Here, we have developed local-delivery selective-plane illumination microscopy (ldSPIM) to address this issue. ldSPIM uses a nanopipette to accurately deliver individual proteins to a defined position. For single-molecule fluorescence detection, we implemented single-objective SPIM using a reflective atomic force microscope cantilever to create a 2 µm thick light sheet. Using this setup, we demonstrated that ldSPIM can deliver single fluorophore labelled proteins onto the plasma membrane of HEK293 cells or into the cytoplasm and characterise the interaction between cells and the delivered molecules in 3D at the same time. Then, we applied ldSPIM to characterize TLR4 activation and Myddosome signalling. The TLR4 agonist lipopolysaccharides (LPS) and aggregates of amyloid-β, which are supposed to be one of the key toxic species in Alzheimer's disease, were delivered onto single macrophage stably expressing a MyD88-eGFP fusion construct. Whole-cell 3D light sheet imaging enabled the live detection of MyD88 accumulation and the formation of the Myddosome signalling complexes. Kinetics analysis of the trajectory of the assembly of individual Myddosomes suggested that amyloid-β triggered a significantly different Myddosome response compared with canonical LPS-triggered signalling. The nanopipette was also used to locally deliver interferon β onto mouse embryonic fibroblasts, to trigger the interaction between the interferon alpha and the beta receptor subunit 1 and the interferon alpha and beta receptor subunit 2. Lastly, in order to improve the light sheet imaging capability, we designed and assembled an epi-illumination SPIM (eSPIM), which is a next generation single-objective light sheet microscope with much faster scanning and is compatible with all kinds of sample dishes including multi-well plates. Overall, this thesis describes the building of new instrumentation to study cell signalling at the single molecule level, combining controlled delivery, via a nanopipette, and light sheet imaging, and the application of this instrumentation to study TLR4 signalling and the kinetics of Myddosome formation.

# Acknowledgement

Firstly, I would say thank you to Prof. Sir David Klenerman. Thank you very much for giving me an opportunity to work in such a fantastic group, your enthusiasm in science and your brilliant idea to assist me finishing my PhD.

Secondly, I appreciate all my colleagues. I would like to thank Dr Aleks Ponjavic for teaching me how to build and use Light Sheet Fluorescence Microscope. I would like to thank Dr Wilson Chen for giving all components of his Scanning Ion Conductance Microscope to me generously. I would like to thank Dr Yu Ye and Jason Sang for giving me HEK cells and teaching me how to cultivate them. I would like to thank you Dr. Lee Hopkins, Dr Jack Brelstaff and Prof. Clare Bryant for giving me the macrophages. I would like to thank Prasanna Suresh for helping analysing the Myddosome data and proofreading my thesis. I would like to thank Ziwei Zhang for building the eSPIM together with me, without her help I cannot make eSPIM a complete chapter in my thesis. I would like to thank Prasanna Suresh and Dr Jack Brelstaff again as well as Jonathan Meng, Gabrielle McClymont and Jeff Lam for helping me proofread the thesis.

Thirdly, I want to say thank you to Cambridge Trust and China Scholar Council, without their funding I could not come and study in Cambridge.

Finally, I want to say thank you to my family and especially to Miss Xiaohua Chen, for always being there with me.

I could not have done it without you.

Thank you, from my heart.

# Contents

# Abbreviation

| | |
|---|---|
| **Aβ** | Amyloid-beta |
| **AD** | Alzheimer's disease |
| **AFM** | Atomic force microscopy |
| **AICD** | Amyloid precursor protein intracellular domain |
| **APP** | Amyloid precursor protein |
| **BACE1** | β-secretase 1 |
| **DAMPs** | Danger-Associated Molecular Patterns |
| **EMCCD** | Electron Multiplying Charge Coupled Device |
| **eSPIM** | epi-illumination Selective Plane Illumination Microscopy |
| **FACS** | Fluorescence activated cell sorting |
| **FOV** | Field of view |
| **FPGA** | Field Programmable Gates Array |
| **FWHM** | Full Width at Half Maximum |
| **GFP** | Green Fluorescent Protein |
| **HEK** | Human Embryonic Kidney *cell* |
| **HILO** | Highly Inclined and Laminated Optical sheet |
| **iBMMS** | immortalised bone marrow derived macrophages |
| **ldSPIM** | local delivery Selective Plane Illumination Microscopy |
| **IFNs** | Interferons |
| **IFNAR1** | Interferon Alpha And Beta Receptor Subunit 1 |
| **IFNAR2** | Interferon Alpha And Beta Receptor Subunit 2 |
| **IRAK2/4** | Interleukin-1 receptor-associated kinase-like 2 |
| **LPS** | Lipopolysaccharide |
| **LSFM** | Light Sheet Fluorescence Microscopy |
| **MEFs** | Mouse embryonic fibroblasts |
| **MyD88** | Myeloid differentiation primary response 88 |
| **NA** | Numerical aperture |
| **NF-κB** | Nuclear factor kappa-light-chain-enhancer of activated B cells |

| | |
|---|---|
| **NO** | Nitric oxide |
| **PA** | photoactivatable |
| **PAMP** | Pathogen Associated Molecular Pattern |
| **PRRs** | Pattern recognition receptors |
| **sAPPα** | Soluble peptide APP-α |
| **sAPPβ** | Soluble peptide APP-β |
| **SICM** | Scanning Ion Conductance Microscopy |
| **SimPull** | Single molecule pull down |
| **SMOC** | Supramolecular Organizing Center |
| **SNR** | Signal to noise ratio |
| **SPM** | Scanning Probe Microscopy |
| **SPIM** | Selective Plane Illumination Microscopy |
| **TIRF** | Total Internal Reflection Fluorescence Microscope |
| **TLR** | Toll-Like Receptor |
| **TNF** | Tumor Necrosis Factor |
| **UPS** | Ubiquitin-Proteasome System |
| **WGA** | Wheat Germ Agglutinin |
| **°C** | degree(s) Celsius |

# Chapter 1
# Introduction to light sheet microscopy, nanopipette based local delivery technology and Toll-like receptor 4 mediated inflammatory signalling.

This chapter introduces the key elements of this thesis. Firstly, it discusses light sheet microscopy which is used in this work to image cells. Scanning ion conductance microscopy (SICM) and nanopipette delivery is then introduced which are used for controlled local delivery of molecules in combination with light sheet imaging. This novel instrumentation is then applied to study the triggering of the toll like receptor 4 (TLR4), so TLR4 mediated inflammation is introduced before an overview of the aims of this thesis is presented.

**1.1 Light sheet microscopy**

Optical microscopy collects visible light passed through or emitted from a sample to create an image of the sample. Fluorescence microscopy is a form of optical microscopy that uses the excitation and emission of fluorescence. Targets within the sample are initially labelled with fluorescent probes at the beginning of the experiment. Once excited by lasers with certain wavelength, the fluorescence emitted from these probes is collected by an objective lens and projected to form an image, allowing direct visualisation of specific biological components and processes in live and fixed cells.

Fluorescence microscopy is an important tool in biophysical and biomedical research owing to its capability of visualizing bright subcellular components on a dark background and its versatile compatibility with various illumination modes to achieve single molecule resolution[1–9]. For instance, single-molecule imaging of live cells has already been achieved in the past by epi-fluorescence microscopy and total internal reflection fluorescence microscopy (TIRF)[2,6,7]. In particular, conventional epi-fluorescence microscopy is a wide-field illumination configuration, in which the excitation laser light passes through the whole specimen and non-specifically excites all the fluorophores inside the sample not only the fluorescence in focal plane but also those above and below focal plane along the optical axis . Therefore, the wide-field excitation configuration often results in three undesired effects[10,11]: 1. inefficient use of fluorophores, 2. Out-of-focus fluorescence signals that reduces the signal to noise ratio (SNR), and 3. the phototoxicity of live specimen due to photobleaching of both fluorophores and many endogenous organic compounds. On the other hand, TIRF employs an incident laser beam passing through the substrate liquid interface obliquely at an angle greater than the critical angle of refraction. Above this angle, the laser beam is totally reflected, generating an evanescent wave to illuminate and excite a restricted region just above the substrate liquid interface with ~200 nm thickness. Compared with epi-fluorescence microscopy, TIRF is able to eliminate the out-of-focus fluorescence signals by exciting a thin section of a specimen and illuminate fluorophores only inside the focal plane. However, the thin evanescent field greatly limits the capability of TIRF to probe molecules of interest inside the specimen[12], making TIRF unable to image samples in 3D.

In order to acquire 3D images of cell samples and visualize single molecules in living cells, selective plane illumination microscopy (SPIM) has been developed recently. In contrast to

conventional epifluorescence microscopy that excites all fluorophores in a sample, SPIM generates a light section inside the sample and only fluorophores within the section are able to be illuminated while fluorophores outside the section remain unexcited. Fluorophores can be used effectively, and on the other hand, the out-of-focus signals[13–15] , and phototoxicity can be minimized signficantly[16]. For example, when SPIM is used to image the zebrafish, the specimen receives 300 times less energy than conventional microscopy and 5000 times less energy than epi-fluorescence microscopy[17]. By adjusting the position of the light section of the sample stage, the entire sample can be imaged with tuneable scanning step size to render whole 3D imaging possible.

Highly inclined and laminated optical sheet (HILO) microscopy is a commonly used form of SPIM[18]. HILO generates a light section by positioning an incident laser beam at the edge to the objective lens, similar to TIRF, with a smaller incline angle of the laser beam. The laser beam is highly inclined by large refraction at the glass-specimen interface and laminated as a thin optical section penetrating the specimen. (Figure 1.1). The laser section is able to be moved along the Z axis to scan the whole specimen. Compared with TIRF, HILO is able to provide detailed information inside the cell and has the potential to determinant 3D architecture of a living cell. However, for whole cell imaging, the minimal thickness of the illuminated volume with HILO is 5~6 μm. Given the normal cell size is around 15 to 20 μm, the light section generated by HILO does not offer sufficient spatial resolution for a 3D cell scan.
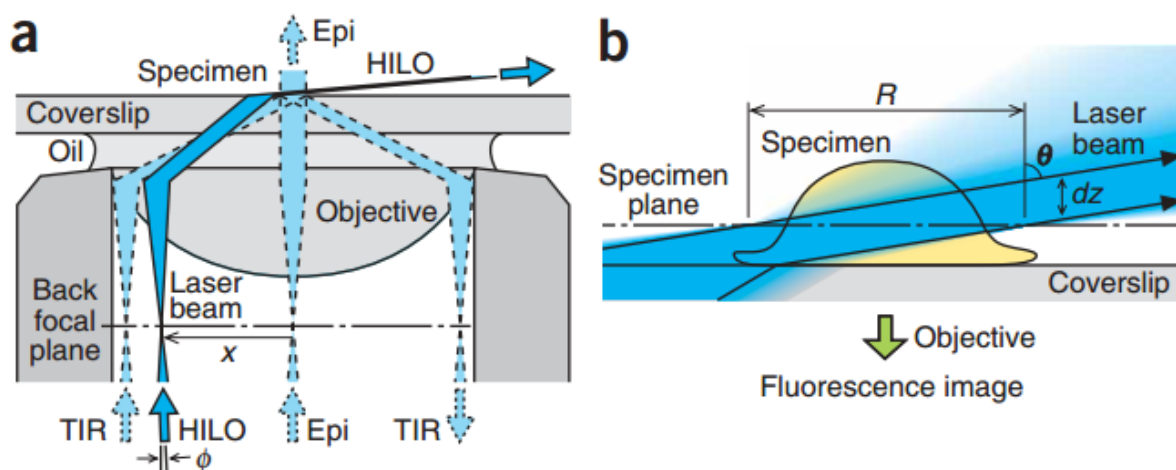
**Figure 1.1.** Optical pathway of TIRF, HILO and epifluorescence microscopy. (a) Different incline angles of laser beam result in different microscopy modes. TIR, HILO and Epi represent the total internal reflection fluorescence microscopy, highly inclined and laminated optical sheet microscopy and epifluorescence microscopy, respectively. (b) Highly reflected laser beam is laminated to form a light section illuminating the structure inside a cell specimen. Adapted from M. Tokunaga *et al*[18].

To further optimise the light section thickness inside the sample and therefore spatial resolution of 3D scanning, light sheet fluorescence microscopy (LSFM) has been developed[19]. Using a cylindrical lens[20], LSFM can generate a light sheet from the side of the specimen with a thickness less than 1 μm (Figure 1.2). The ultra-thin light section can further reduce background signal and achieve superior contrast for single-molecule fluorescence imaging. To introduce the light sheet into biological samples, a two objective lens geometry is commonly used (Figure 1.2). A secondary objective lens is positioned perpendicular to the detection objective to introduce the light sheet from the side of the sample. In this platform, the two objective lenses are often positioned near each other. As a result, this limits the numerical aperture (NA) of the two objective lenses which in return reduces the axial resolution and collection efficiency, but also restricts the sample mounting format that can be used. Normally a tube or cylinder containing agarose gel is used for fixed cell imaging and a customised chamber that has a flat interface through which the light sheet can enter is used for live cell imaging. The customised sample chamber fabrication is highly complicated and not compatible for high-throughput imaging. Furthermore, the chamber is made by combining two coverslips with adhesive and the sample area is regulated by PAP pen, which makes the chamber not suitable for cell culturing, therefore not compatible with cells such as macrophages that need to be seeded and cultured before imaging.
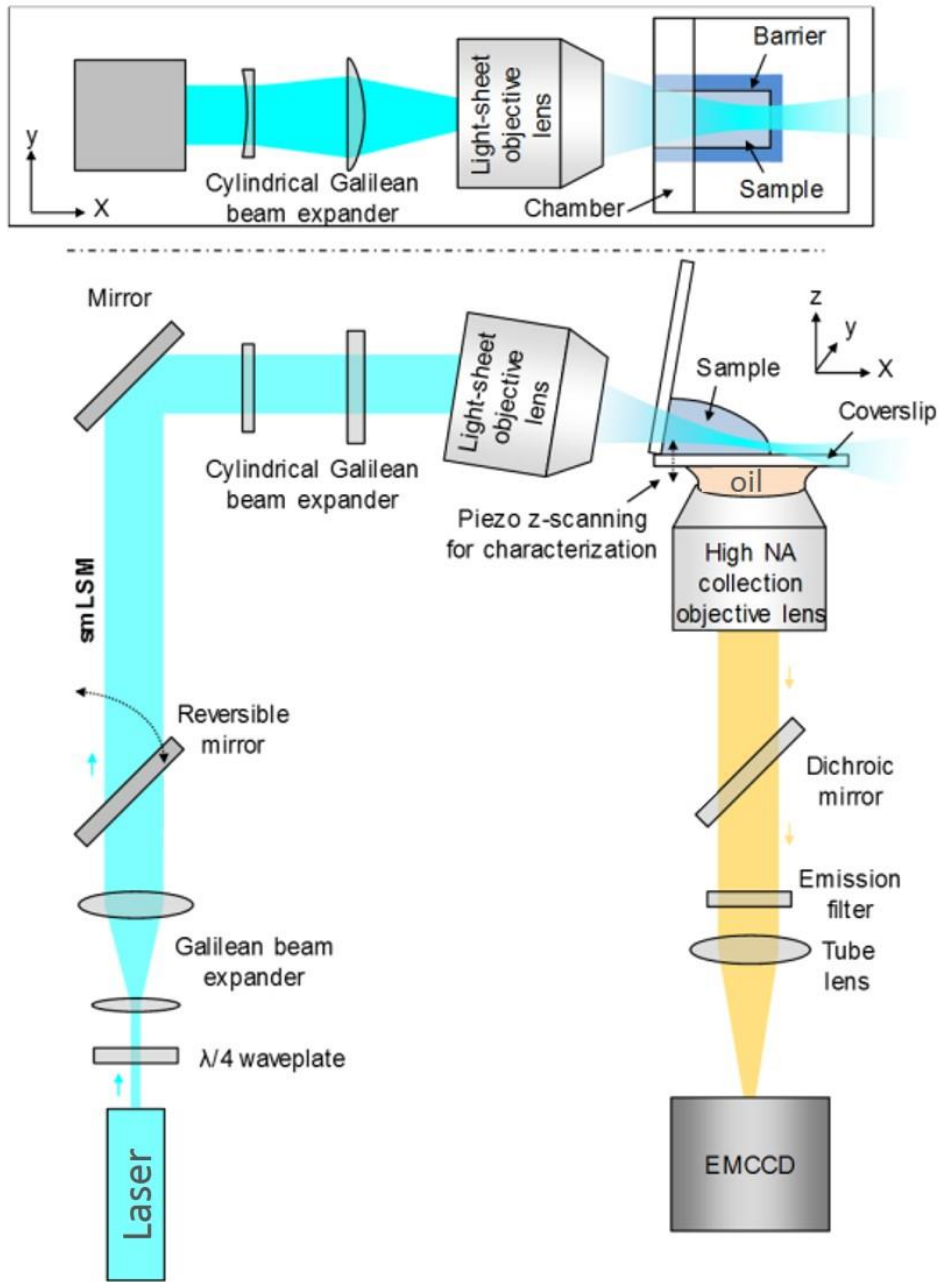
**Figure 1.2.** The optical pathway of light sheet fluorescence microscopy. Two orthogonal optical pathways operate fluorophores excitation and fluorescence signal collection separately. A cylindrical lens is employed to generate a laser beam which is collimated in the XY direction and focused on the Z direction. Adapted from A. Ponjavic *et al*[21].

To fit a standard sample dish within the LSFM setup, an alternative way to structure the two objective lenses is devised placing a reflective atomic force microscopy (AFM) tip in the cell medium as a mirror near the cells. The light sheet is then introduced by the objective lens from the top and reflected to the sample by the AFM tip[22,23]. However, due to the size of the objective lens, this particular platform is incompatible with the multi-well plates such as 96-well plates, the imaging through-put is still low (figure 1.3). Moreover, oblique angle LSFM was developed to achieve light sheet imaging with a single-objective lens[24,25]. Similar to HILO, the oblique angle microscopy LSFM generates a highly angled light sheet and tilts the imaging plane using an additional objective. This single-objective geometry is compatible with 96-well plates. Yet, the NA of the lens to produce highly angled light sheet and the light collection efficiency is low, which prevent it from being applied to single molecule imaging.
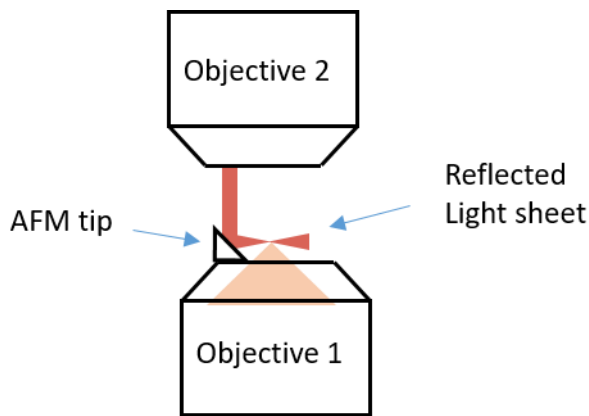
**Figure 1.3.** Schematics of dipping objective lens geometry and AFM tip reflection.
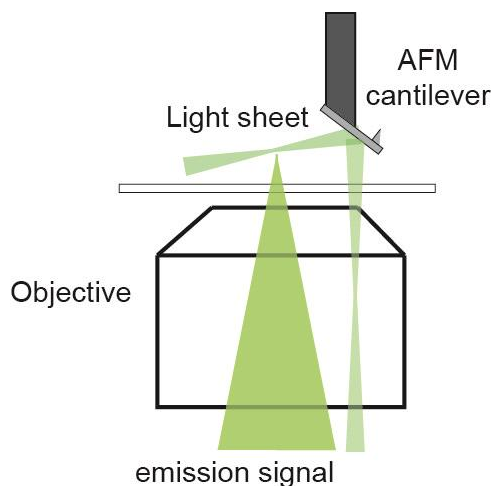
**Figure 1.4.** Schematics of single-objective AFM cantilever light sheet microscopy.

Taking advantages of the AFM tip reflection and single-objective geometry, our lab put forward a new design of single-objective AFM cantilever reflective LSFM (Figure 1.4). The light sheet is introduced from a high NA objective lens on an inverted microscope. On top of the lens, an AFM cantilever—which can be moved freely in all XYZ directions—is placed near the sample to reflect the light sheet. The excitation fluorescence signal is acquired by the same objective lens. The high NA objective lens enables single-molecule sensitivity, and the flexibility of the AFM cantilever helps us achieve high throughput and versatility with different cell culture formats, such as 96-well plate.

## 1.2 Scanning ion conductance microscopy and nanopipettes

Scanning ion conductance microscopy (SICM) is designed to image the surface morphology of soft biological samples such as live cells in water solution. SICM uses a nanopipette as the scanning probe, which is a quartz tube fabricated by a laser puller to form a conical tip with an opening approximate 100 nm wide. Two Ag/AgCl electrodes are used. One electrode is put into the nanopipette which is filled with electrolyte and the other is placed in the bath solution which holds the cell samples (Figure 1.5). Feedback control is achieved by applying a potential between two electrodes and measuring the current induced by ion flow through the nanopipette. When the nanopipette is far away from the sample surface, ions are capable of flowing through the nanopipette without any restriction so that the ion current is large. As the pipette approaches the sample surface, the space between the pipette and sample surface becomes narrowed and fewer ions passing through the nanopipette. Therefore, the ion current decreases with the decreasing distance between the pipette and surface. Usually, when the size of the nanopipette is ~100 nm, a 1-2% current drop indicates the distance between the pipette and sample surface is around 100-200 nm. (Figure 1.6)[26]. Based on this current drop, when the nanopipette is approaching different positions on sample surface, the distance that nanopipette travelled to reach the current is represent as the relative height of the corresponding position. Assembled together it can generate a topographic image of the scanned sample surface.
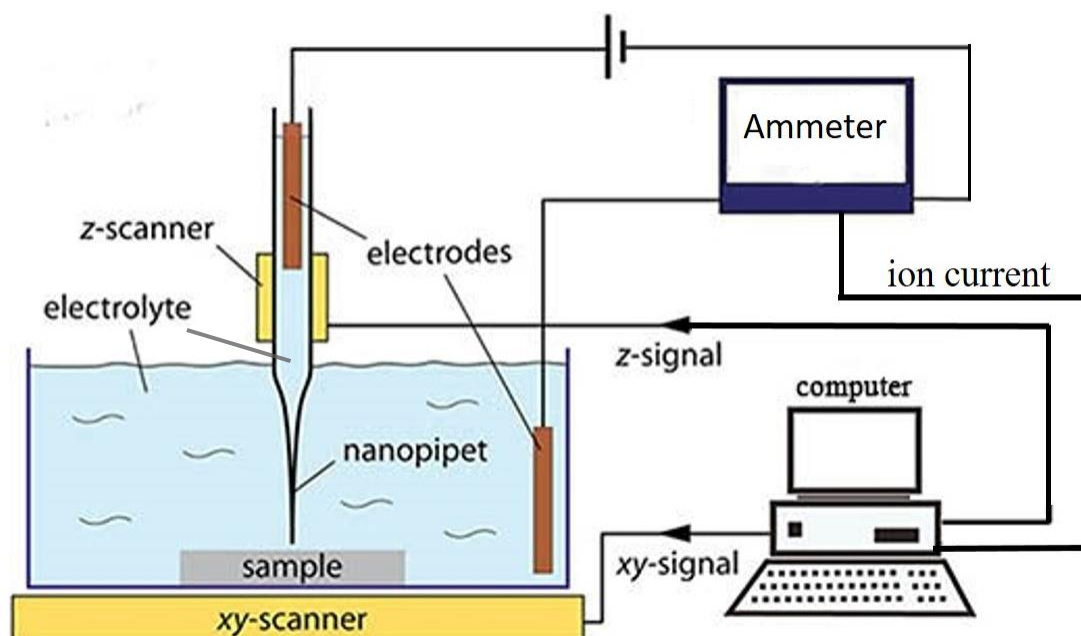


**Figure 1.5.** Schematic set up of scanning ion conductance microscope. A nanopipette is employed to work as scanning probe controlled by the piezo scanner. Two electrodes are put inside the nanopipette and bath to form a circuit and generate the feedback ion current.
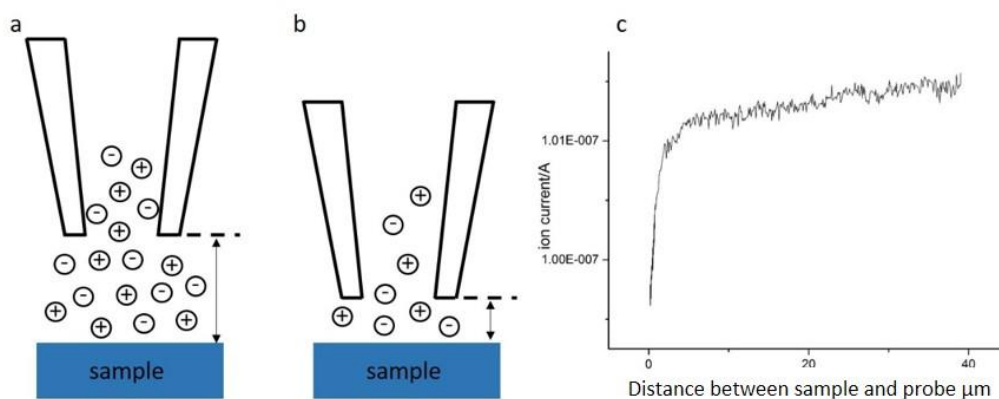
**Figure 1.6.** The relationship between the value of the ion current and the distance between the sample surface and probe. (a) When the probe is far away from sample surface ions flow through the tip without any restriction and the current value is large. (b) When the probe approaches the sample surface, the space between nanopipette and sample is narrowed thus few ions pass through the nanopipette, resulting in the decline of the current. (c) The relationship between the ion current and the distance between the sample surface and nanopipette. When the nanopipette gets close to the sample surface, ion current declines exponentially.

Since SICM uses a hollow nanopipette as its scanning probe, it can also work as a local delivery vehicle[27–29]. Target molecules can be loaded into the nanopipette and delivered to a certain position by using extra voltage or pressure. For example, if the target molecule has a positive charge when the pipette is far away from the delivery region, a negative potential or pressure can be applied to the nanopipette to attract molecules without leaking out into the solution. When the nanopipette approaches the sample surface, the negative potential and pressure will be reversed for a short period of time to force a controlled amount of the target molecules leave the nanopipette to be delivered to the sample surface.

## 1.3 Local delivery

The development of an efficient and controllable methods to accurately deliver small amount or even single biomolecules to a specific location is important in nanotechnology as well as biotechnology[30]. This is because introducing molecules onto cell surfaces is the most efficient way to study cellular responses *in vivo*, such as membrane receptor triggering and signalling. The conventional method to add molecules onto cell surface is to put target molecules into cell media and let them diffuse to each cell. In this way, all cells in the sample dish would be triggered while only a few could be imaged. In contrast, the local delivery methods can focus the exogenous molecules onto a specific cell while the other cells would remain unstimulated (Figure 1.7). However, commonly used methods do not have the capability of depositing molecules to a specific location on cell membrane[31]. For instance, a conventional method to deliver molecules onto a cell surface is microiontophoresis[32], in which charged molecules in a micropipette are deposited using a voltage pulse. This method has several limitations. Firstly, the aperture of micropipette is larger than 10 μm and thus it cannot focus on a specific area on the cell surface[33,34]. Secondly, it does not have feedback control for sensing the distance between the pipette and sample surface. This makes it more challenging to restrict deposited molecules on a certain cell without leakage. Scanning Probe Microscopy (SPM) can be employed to overcome these problems[27–29,31,35–40]. Specifically, the probe of a scanning ion conductance microscope (SICM), which is a fabricated quartz nanopipette with a conic tip of 100 nm diameter, has been successfully used for local delivery. Ion current flow is used as the feedback signal to control the distance between the nanopipette and the sample surface. An extra voltage or pressure pulse was then used to deliver target molecules to a specific location. If the target molecule has a positive charge, the voltage between two electrodes or negative pressure over the nanopipette is used to keep molecules inside the nanopipette when the pipette is far away from the sample surface. When the nanopipette approaches the sample surface, either the negative pressure or extra voltage is reversed for a short time of dispositing target molecules at the position of the nanopipette (Figure 1.8). reference here

The amount of delivered molecules is regulated by the magnitude of the applied voltage or pressure pulse and the pulse dwell time. Nanopipette-based delivering methods have several advantages over conventional methods. Firstly, the diameter of nanopipette can be less than 100 nm, which is much smaller than cells. It therefore enables delivery of molecules onto

different areas of the same cell. Secondly, these methods have a feedback control to adjust the distance between pipettes and sample surfaces, which can ensure that most of the delivered molecules are deposited on the sample surface rather than diffusing away into the solution. This significantly facilitates calculation of the number of molecules that are delivered onto the cell surface. In addition, since the diameter of the nanopipette is nanometric, it has great potential in single molecule delivery and nano-injection of molecules into the cytoplasm or nucleus.
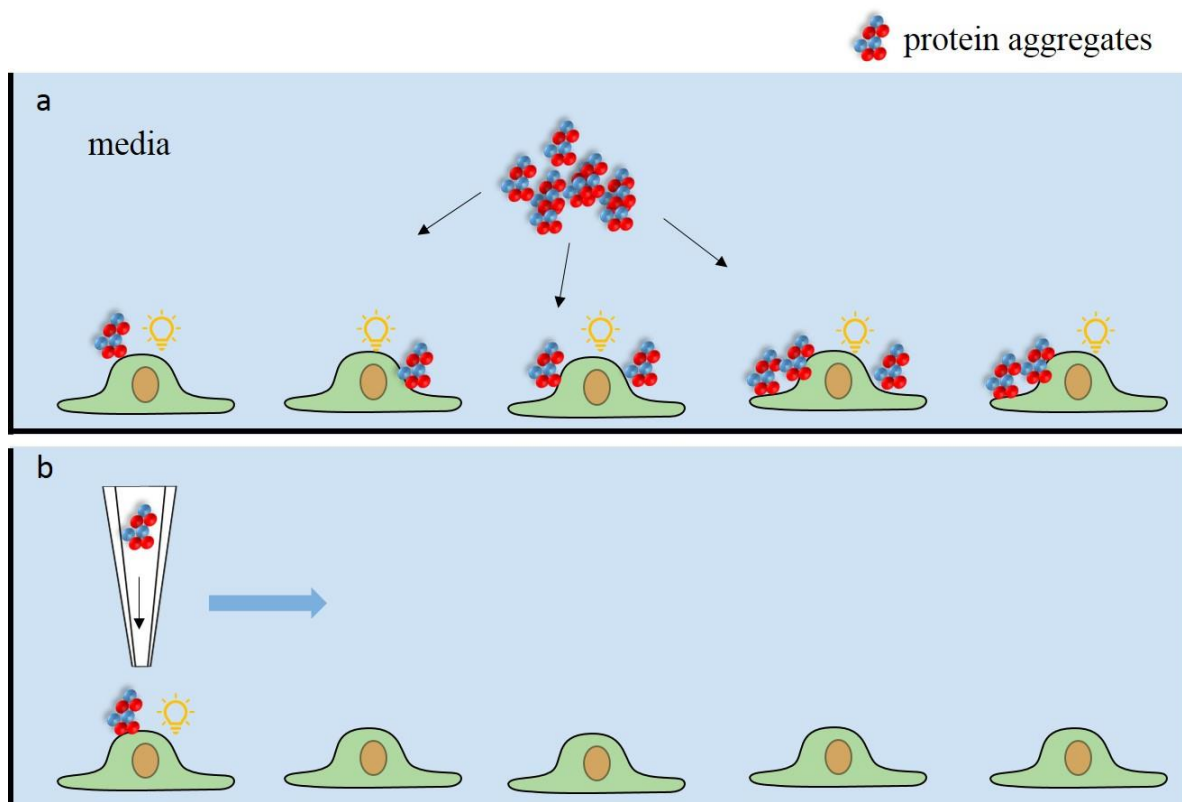


Figure 1.7. Advantage of using local delivery and imaging system to study TLRs triggering and signalling. (a) Molecules are added into media, all cells in the dish will receive different amounts of molecules and get triggered at the same time. (b) The mechanism how the local delivery system works. With the nanopipette working as local delivery vehicle, molecules are able to be delivered onto a specific cell surface in a controllable and repeatable manner. Only the cell that receives delivered molecules is triggered and other cells remain inactivated
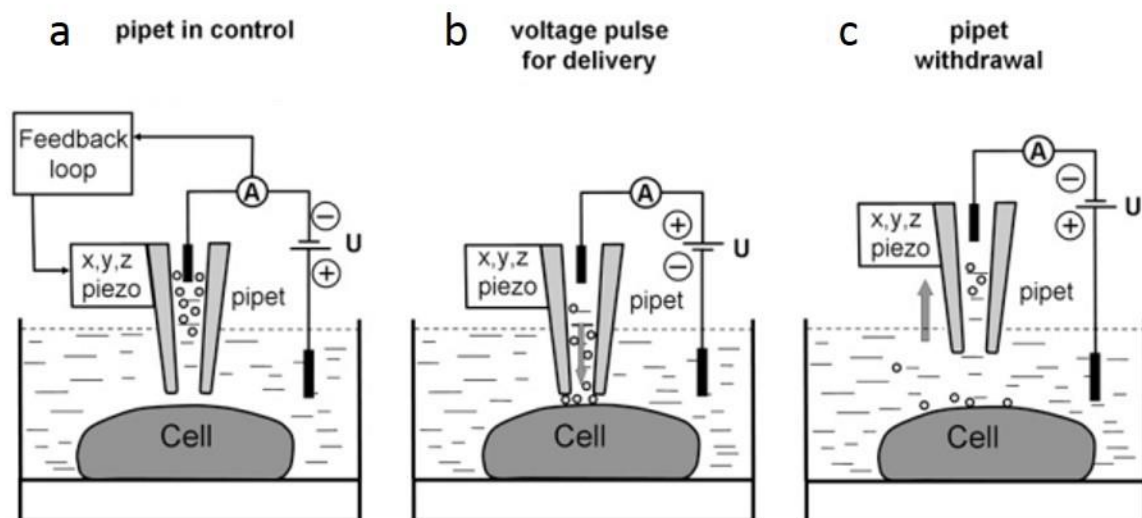
**Figure 1.8.** Schematic of the process describing how positively charged molecules are delivered to a specific position on the cell surface through a nanopipette using a voltage pulse. **(a)** The nanopipette is moved to a location 200nm above the cell surface using a negative potential applied to the electrode inside the nanopipette so that molecules do not exit. **(b)** A positive voltage pulse is applied to drive molecules out of the nanopipette and deliver them to the location underneath the nanopipette. **(c)** When the delivering process is finished, the nanopipette is withdrawn rapidly and carefully at a negative potential to prevent molecules from leaking out into the solution. Adapted from A. Bruckbauer.[31]

## 1.4 Intracellular injection

The development of novel injection tools can introduce extra material inside cells without affecting their viabilities, is key in the development of single-cell analysis as well as modern biophysics[41–43]. Introducing molecule, such as protein, inside cells can help with the understanding of how exogenous molecules interact with subcellular structure and produce cell functions such as proteasome aggregation or other immune responses. The most common method to introduce exogenous molecules inside the cell is adding these samples into the bath solution and letting these molecules to diffuse to a cell and enter the endosome. However, there are several factors that prevent direct addition from being an effective method. Firstly, when adding molecules directly into the bath solution, the location where molecules could enter the cell is random. We cannot introduce molecules to a specific location inside the cell, for example the nucleus or the area that contains more mitochondrion. Secondly, there may be a size bias to protein molecules when they enter the cell, which means some large proteins such fibrils cannot get into the cell via the endosome. Lastly, the throughput is very low as the added molecules diffuse to all cells in the sample dish and trigger cell responses at the same time, and we can only focus on one single cell. If we want to observe another cell response when it receives target molecules, one must use another dish of cell (Figure 1.9 (a)). All these limitations result in inefficient use of target molecules and hence a better method would be injecting target molecules into a single cell directly (Figure 1.9 (b)).

Among various chemical (lipids)[44,45], biological (membrane penetration peptide and virus)[46,47] and physical (particle and microinjection)[48–53] injection methods, microinjection[50] and electroporation[51–53] are the most commonly used directly injection methods. This is because microinjection and electroporation can introduce controllable amounts of molecules into a specific single cell directly and regardless of cell types while other methods always resulted in poor delivery efficiency because the unregulated amounts of molecules are randomly diffused to each cell and the long injecting time period[54,55]. Microinjection employs a fabricated micropipette with outer diameter of several microns to penetrate the cell membrane and then pressure pulses are applied to pump molecules into the cell. Electroporation uses an electrical field to generate transient pores on cell membrane where molecules like DNA and RNA[56,57] can get into the cytoplasm. Electroporation can also use microfluidics or micropipettes to trap single cells and use of electrical field to direct molecules into a specific cell[52,58]. However, they

have several limitations. Firstly, the micropipette penetration may cause huge damage to the cell membrane and high mortality due to the large penetration depth and area[59]. Secondly, the uneven distribution of the electrical field could also cause cell death. Lastly, it is challenging for them to deposit molecules to a specific location inside the cell especially into the nucleus. To overcome these issues, the nanopipette used by SICM could also be applied to inject molecules into the cells[31,38,60]. Due to its small size, the nanopipette can penetrate the cell membrane or nuclear membrane easily with a penetration depth of only a few microns. When the injection process is finished, the nanopipette will be retracted rapidly and move to the next cell. Theoretically, when the injection is operated on one cell, other cells in this dish are all independent and will not be affected.
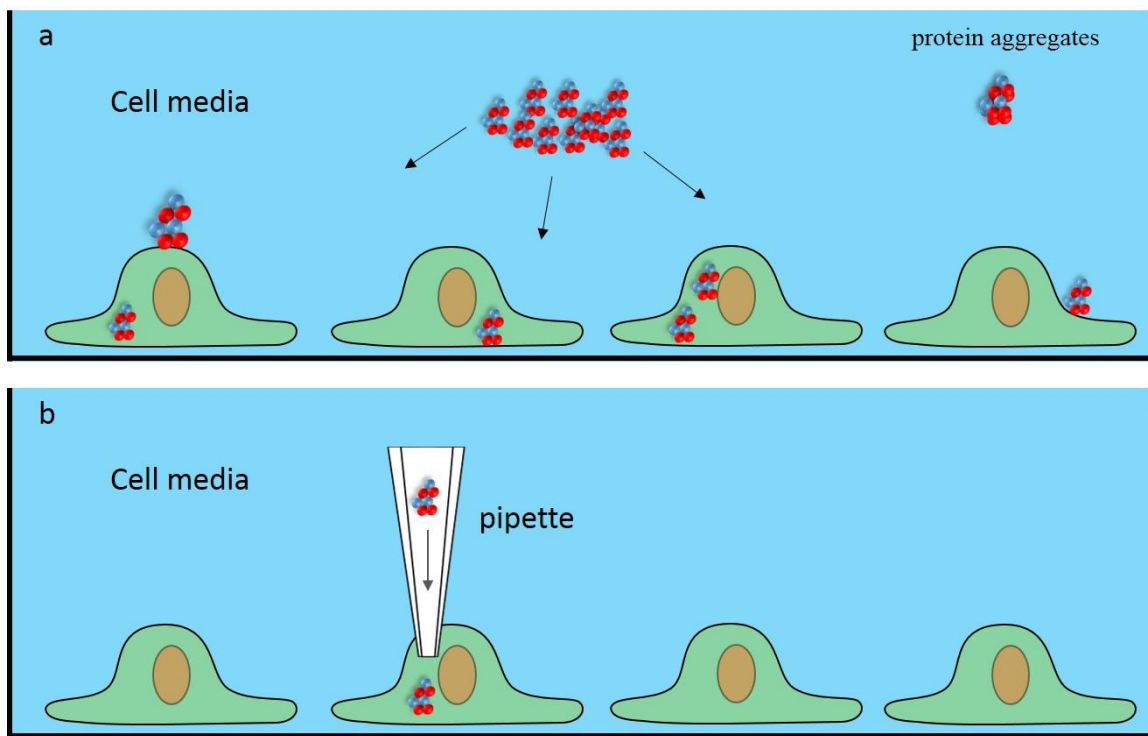


**Figure 1.9.** (a) When target molecules such as protein aggregates are added to cell media, they will diffuse to each cell in the dish and enter cells at a random position. (b) Pipette injects the molecule into a single cell at a specific location without affecting neighbouring cells.

**1.5 Alzheimer's disease**

Dementia is a chronic or progressive syndrome, in which there is a decline in cognitive function that is not caused by normal aging. It affects several intellectual domains, such as memory, thinking, language and learning capacity, which results in loss of capabilities to perform basic activities of daily life. Among the elderly people worldwide, dementia is the main cause of dependency and disability. According to WHO 2022 estimation, over 50 million people are suffering from dementia and every year there are nearly 10 million new cases. It is overwhelming not only for patients who have it, but also for their families, costing hundreds billions of US dollars per year. Dementia results from various kinds of diseases and injuries, a fatal neurodegenerative disorder, Alzheimer's disease (AD), is the most common cause and accounts for 50 to 75% of all cases[61,62]. Since its prevalence increases with life expectancy, individuals older than 65 years are under rising risk of cognitive impairment. AD's seriousness continues to grow because many of global populations are experiencing aging problems. Therefore, understanding the neurobiology mechanisms of AD plays a key role in diagnosis and treatment of AD.

Following Alois Alzheimer's first description of AD in his original paper in 1907, the pathologies of AD were discussed over a hundred years. Currently it has been universally acknowledged that the extracellular deposition of amyloid beta-peptide (Aβ) plaque and intracellular neurofibrillary tangles of hyperphosphorylated microtubule-associated tau proteins are the hallmarks of the disease. In AD, the Aβ plaque and neurofibrillary tangles of tau proteins are mainly observed in brain regions such as the cortex, hippocampus, basal forebrain and amygdala[63]. Anatomy also provides us with evidence that Aβ plaque damages the synapses and neuritis in AD brains resulting in synapses loss, reactive gliosis, microglial activation, and neuroinflammation[64].

## 1.6 The amyloid cascade hypothesis

Among the hypothesis for AD, extracellular accumulation of Aβ is the dominant one that has been emphasized by recent studies and is commonly accepted as a mechanism of AD. Amyloid cascade hypothesis mainly indicates that AD is caused by a sequence of pathological events, starting with the accumulation and deposition of Aβ which leads to plaques. Consequently, these events will cause synaptic and neuronal dysfunction.

Aβ is a peptide that is very hard to undergo proteolytic degradation. Its 1-42 isoforms is believed to be the most hydrophobic and have the greatest cellular toxicity. Due to its physical configuration, it is often presented in a structure of β-pleated sheet, which has high potential to aggregate and form the core of amyloid plaques[65–69]. Aβ is generated in the process of degradation of the amyloid precursor protein (APP) (Figure 1.10). APP is a transmembrane glycoprotein of type I and its processing has two pathways. On one hand, APP can be broken down by enzymes with α-secretase activity, releasing an amino terminal peptide called APPsα, which is soluble and nontoxic, and a fragment of the carboxyl terminal portion. In AD brains APPsα is present at low levels and has been associated with trophic and neuroprotective functions[70,71]. On the other hand, the APP can be processed by a β-secretase, β-site APP cleaving enzyme (BACE 1), yielding a shorter soluble toxic amino terminal portion (APPsβ) and a longer terminal carboxyl fragment (C99)[72]. The further hydrolysis of APPsβ at the γ site produces the Aβ peptide and AICD. The Aβ42 peptide is non-toxic in its monomeric form but is highly prone to misfolding and aggregating into toxic protein species. As aggregation progresses, the amyloid proteins adopt a beta-sheet structure, which is more stable and therefore harder to degrade. The amyloid assembly mechanism follows a lag, elongation and plateau phase.

Although it is generally accepted that Aβ plays an important role in AD pathogenesis, the mechanisms are still vague and need further research. In addition, Aβ aggregation has also been proven to activate microglial cells and lead to the production of inflammatory mediators such as nitric oxide (NO), reactive oxygen species (ROS), tumor necrosis factor (TNF)-α, Interleukins (IL-1β, IL-6, IL-18), and prostaglandins, which promote neuronal death. These suggest that Aβ accumulation directly contributes to neuronal damage or indirectly contribute to activation of inflammatory systems, leading to progression of AD.
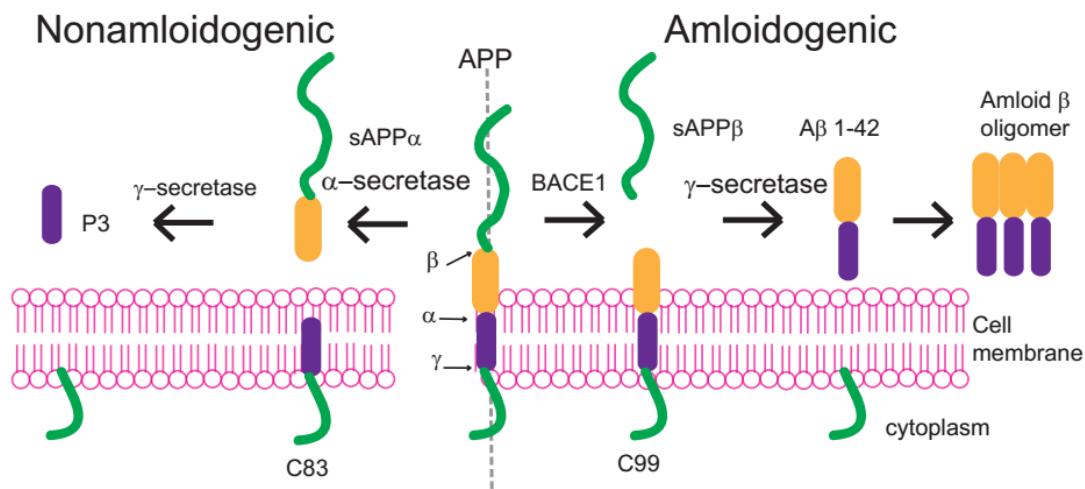
**Figure 1.10.** Schematic representation of APP processing and Aβ accumulation. APP is hydrolyzed by 2 competing pathways, the α-secretase pathway generating sAPPα and C83, and the β-secretase pathway that results in sAPPβ and C99. C99 then is hydrolyzed at γ site producing Aβ42 peptide. Aβ peptide could aggregate into small multimers (dimers, trimers, etc.) known as oligomers.

## 1.7 Toll like receptor triggering and signalling

There are two main immune systems in vertebrates, namely the innate immune system and the adaptive immune system. When the body is exposed to pathogens that are present in the living environment, the innate immune system is the first line of defence[73]. The innate immune system is a nonspecific system that recruits white blood cells, such as macrophages, to destroy invading pathogens and further facilitate presenting specific antigens to cells of the adaptive immune system, such as T and B cells. Recent studies have revealed that the innate immune system can distinguish self-pathogens and non-self pathogens[74]. This recognition relies on a family of pattern recognition receptors (PRRs). PRRs are able to detect a variety of pathogen-associated molecular patterns (PAMPs), which are presented on bacteria, viruses, fungi or danger-associated molecular patterns (DAMPs) released by damaged cells[75–77].

One important group of PRRs is the Toll-like receptor (TLR) family[75]. TLRs are transmembrane receptors that are expressed by a wide range of immune system cells, such as macrophages and dendritic cells[78]. Based on their subcellular distribution and ligand recognition, TLRs can be divided into two categories. TLR1, 2, and 4–6 are distributed on the surface of cell membranes to recognize different pathogens in the extracellular domains[79], while TLR3, 7–9, and 11–13 are located in the endosome components inside the cytoplasm to recognize nucleic acids[79]. In addition to recognition of PAMPs and DAMPs, TLRs are also involved in transducing signals to activate the innate immune response, as well as adaptive immunity[73,80–85]. TLRs contain an extracellular ligand-binding domain and a cytosolic Toll/IL-1R (TIR) domain. Signal transduction is triggered by the dimerization of the ligand-binding domains after binding to pathogens[86]. The dimerization in turn activates the recruitment of adaptor proteins, such as adaptor molecule myeloid differentiation primary-response protein 88 (MyD88) to mediate downstream signal transduction through TIR-TIR interaction between TIR domains on TLRs and adaptor proteins[76].

For instance, during infection and cell stress triggered by lipopolysaccharide (LPS), the TIR domains on TLR4 bind to the TIR domain on MyD88 forming a complex, supramolecular organizing centre (SMOC) called "MyDDosome"[84,87], a protein complex with a stoichiometry of 4 IRAK4, 4 IRAK2, and 6-8 MyD88 molecules[88] (Figure 1.11). The Myddosome is known as a signalling hub which is able to trigger a cascade of signalling events that activates the NF-

κB-dependent expression of cytokines, chemokines[89], and other immunomodulatory factors to drive antipathogen responses and inflammation[86]. It has been shown that rate of assembly, size and total number of Myddosomes formed might correlate with the strength of the immune response[68].

Moreover, the activation of the innate immune system and the subsequent downstream responses, such as inflammation, also play key roles in many disease progressions. Preclinical and clinical studies have proved that the activation of the innate immune system could be involved in the pathologies of neurodegenerative diseases [90–94]. In Alzheimer's disease, both small soluble protein aggregates assembled from *amyloid*-β (oligomers), and large filament components (fibrils) are able to bind TLRs, such as TLR4, and other receptors on microglia, resident macrophage within the brain to activate the immune system and trigger downstream inflammation responses. Thus, introducing controllable amounts of *amyloid*-β aggregation to trigger TLRs and visualizing the kinetics of downstream response are important in understanding the pathologic mechanism of Alzheimer's disease.
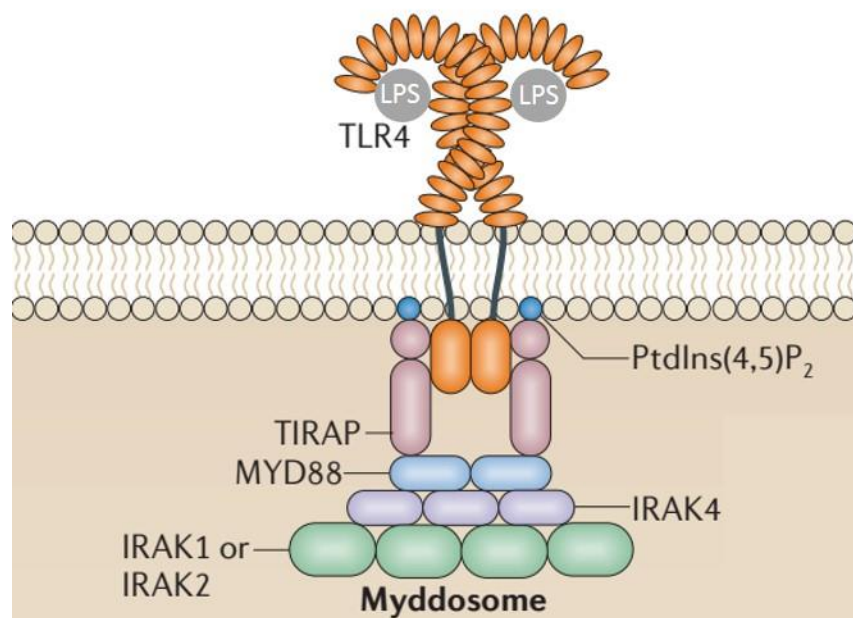


**Figure 1.11.** TLR4 triggered by LPS. TLR4s dimerize and recruit MyDD88 adaptor protein to form a SMOC called Myddosome.

## 1.8 Overview of this thesis

In this thesis, a prototype of local delivery selective plane illumination microscopy (ldSPIM) which combines the core functions of selective plane illumination microscopy and scanning ion conductance microscopy is described first. Four proof of concept experiments show that ldSPIM can accurately sense position, precisely control delivery, deposit single molecules onto a cell surface and perform intracellular injection.

Secondly, one major application of ldSPIM, studying the TLR4 activation and quantitative characterization of the formation of the downstream signaling complex, Myddosome, is described. In this section, the kinetics of Myddosome assembly is characterized and the kinetics for the typical TLR4 agonist LPS and $A\beta$ aggregates, one of the key toxic species in Alzheimer's disease, is compared. Significant differences between the kinetics of LPS and $A\beta$ triggered Myddosome formation were found.

In the third part, a joint project in collaborating with Dr Stephine Huang is described. In this project my work is imaging and characterizing the diffusion coefficient and co-localization coincidence of IFNAR1 and SNAP tagged IFNAR2.

In the last part, I describe building another prototype next generation single objective light sheet microscope, epi-illumination SPIM or eSPIM. To demonstrate the function of eSPIM, three proof-of-concept experiments are performed demonstrating fixed cell membrane imaging, live cell DNA imaging and tracking misfolded protein aggregates in live cells.

# Chapter 2
# Development of local delivery selective plane illumination microscopy (ldSPIM)

This chapter is mainly focused on the building and characterization of the ldSPIM which is capable of delivering precise amounts of molecules onto a cell surface or inside the cytoplasm followed with single-molecule light sheet imaging. Core components and their function are listed with a schematic diagram to present the working mechanism of ldSPIM.

Four proof of concept experiments were performed to quantitatively demonstrate that the ldSPIM is functional in four fundamental aspects: 1) ldSPIM is able to locally deliver target molecules to a pre-defined position on sample surfaces. 2) The amounts of delivered molecules are controllable. 3) ldSPIM is capable of delivering single molecules. 4) ldSPIM can penetrate cell membranes and deliver molecules into the cytoplasm.

Contribution

Bing Li designed the nanopipette based delivery and injection system. Dr Aleks Ponjavic aligned the AFM cantilever light sheet microscope. Bing Li developed the LabVIEW controlling system and analysed the data.

## 2.1 Building the ldSPIM

To address the difficulty of delivering precise amounts of molecules or even single molecules to a specific cell and imaging them simultaneously, we developed a local delivery selective plane illumination microscopy (ldSPIM). ldSPIM was implemented on an inverted optical microscope using a nanopipette under distance feedback control for the delivery of molecules. An AFM cantilever attached to a machined brass rod to introduce a light sheet to the cell sample so that only a single objective was needed for the experiment (Figure 2.1(a) and (c)). The nanopipette used for delivery approached the cell surface at an angle of 45$^o$ and was stopped at a height of approximately 200 nm above the cell surface, as determined by the ionic current dropping by 2% (Figure 2.1(b)). From this position molecules were delivered to the sample surface or intracellularly injected into cytoplasm driven, either by voltage or air pressure. The AFM cantilever was positioned vertically next to the cell to reflect the light sheet (Figure 2.1 (b)). The axial thickness and Rayleigh of the sheet could be calculated by imaging the fluorescence without the cylindrical lens, as was done previously[95]. The light sheet had a thickness of 1.63 μm FWHM with a Rayleigh length of 4.3 μm using a 60x 1.27NA water immersion objective. The sample stage was mounted onto a xyz piezo to enable whole-cell 3D scanning.
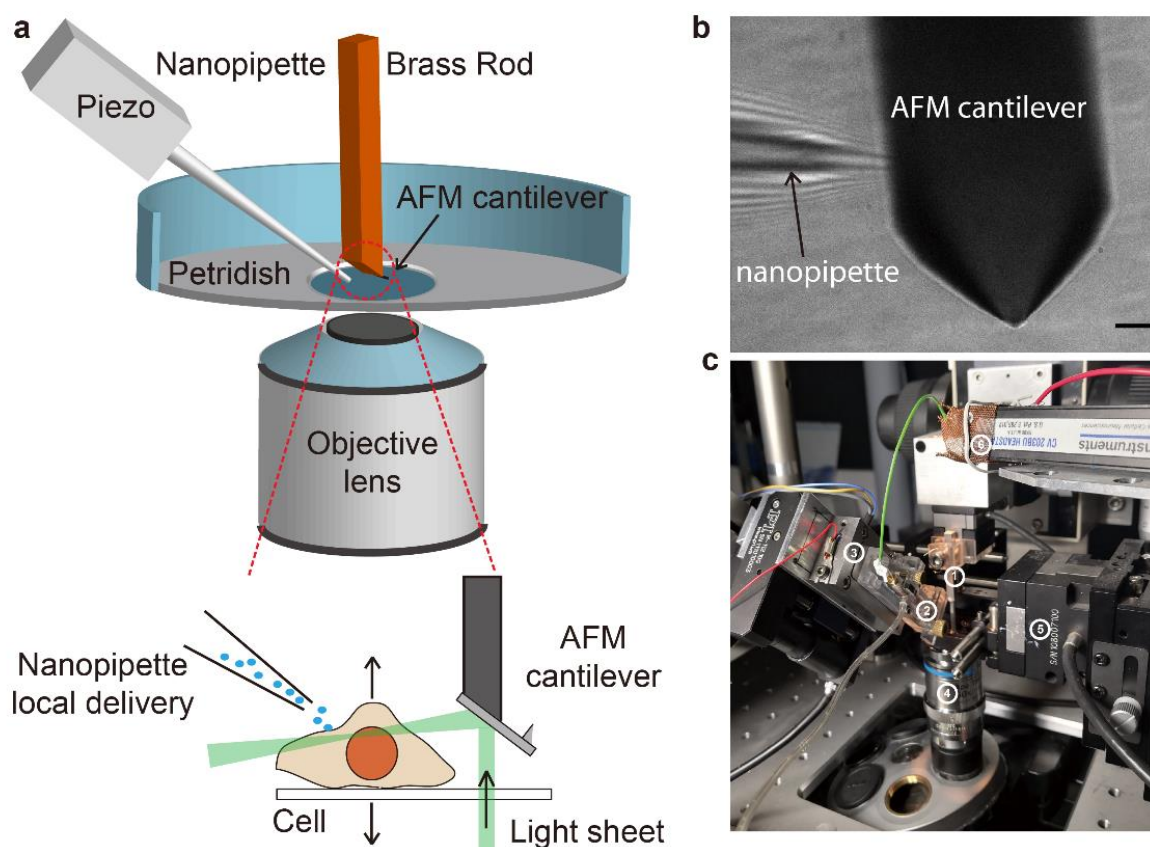
**Figure 2.1.** Set-up of the ldSPIM. **(a)** The schematic of the ldSPIM set up: the combination of piezo controlled nanopipette and reflective AFM cantilever. AFM cantilever is placed above the cell sample to reflect the light sheet and the nanopipette approaches the cell of an angle to locally deliver target molecules onto the sample surface. Scanned by moving the sample stage, the cell can be visualized in a fast 3D live imaging mode. **(b)** The image of the nanopipette and the cantilever is controlled under the brightfield microscope mode. Scale bar is 10 μm. **(c)** Photograph of the ldSPIM setup in use. 1) is the metal rod, 2) is nanopipette on a holder, 3) is the Piezo, 4) is objective lens, 5) is the piezo sample stage and 6) is the detecting head of pitch clamp amplifier, which is used to record the ionic curent.

## 2.1.1 Components of AFM cantilever reflective selective plane illumination microscopy.

In this section the main components of a typical SPIM will be described. Figure 2.2 shows the schematic of SPIM optical pathway. Followed by the sequence of the components listed in the schematic, the excitation and emission path are described first. Then, the instruments responsible for vibration isolation and sample movement are described.

### 2.1.1.1 The excitation optical pathway

**Illumination light source**

Fluorophores in samples are excited by high-intensity monochromatic lasers with powers in the range from 0 to 100mW. In ldSPIM, three laser lines with different wavelengths are co-aligned to achieve multicolour 3D imaging.

**Laser power control**

Illumination power can be controlled either by analog input voltage or neutral optical-density (OD) filters. For analog control, voltage changes from 0V to 5V correspond to the power changing from 0 to 100mW. Neutral OD filters, which are wavelength independent, are able to reduce the intensity of all passing light equally. Its transmission efficiency is defined as OD = $-\log_{10}(I_{out}/I_{in})$, where I is the laser intensity.

**Shutters**

Digitally controlled shutters are installed in each laser beam path, for the purpose of laser safety and fluorophore bleaching protection. Shutters are synchronized with the camera. Only when the camera is taking images the shutter will open.

**Beam expander**

The original size of laser is not large enough to cover the field of view that can be imaged. Therefore, beam expanding optics are used to tune the illumination area. Usually, a Galilean telescope system containing two lenses is used to expand and collimate the beam. The first lens (with focal length f1) diverges the original beam and the second lens (with focal length f2) re-collimated the beam again, magnifying the beam f2/f1 times larger than original one. The distance between two lenses is the sum of the focal length of the two lenses (d = f1+ f2).
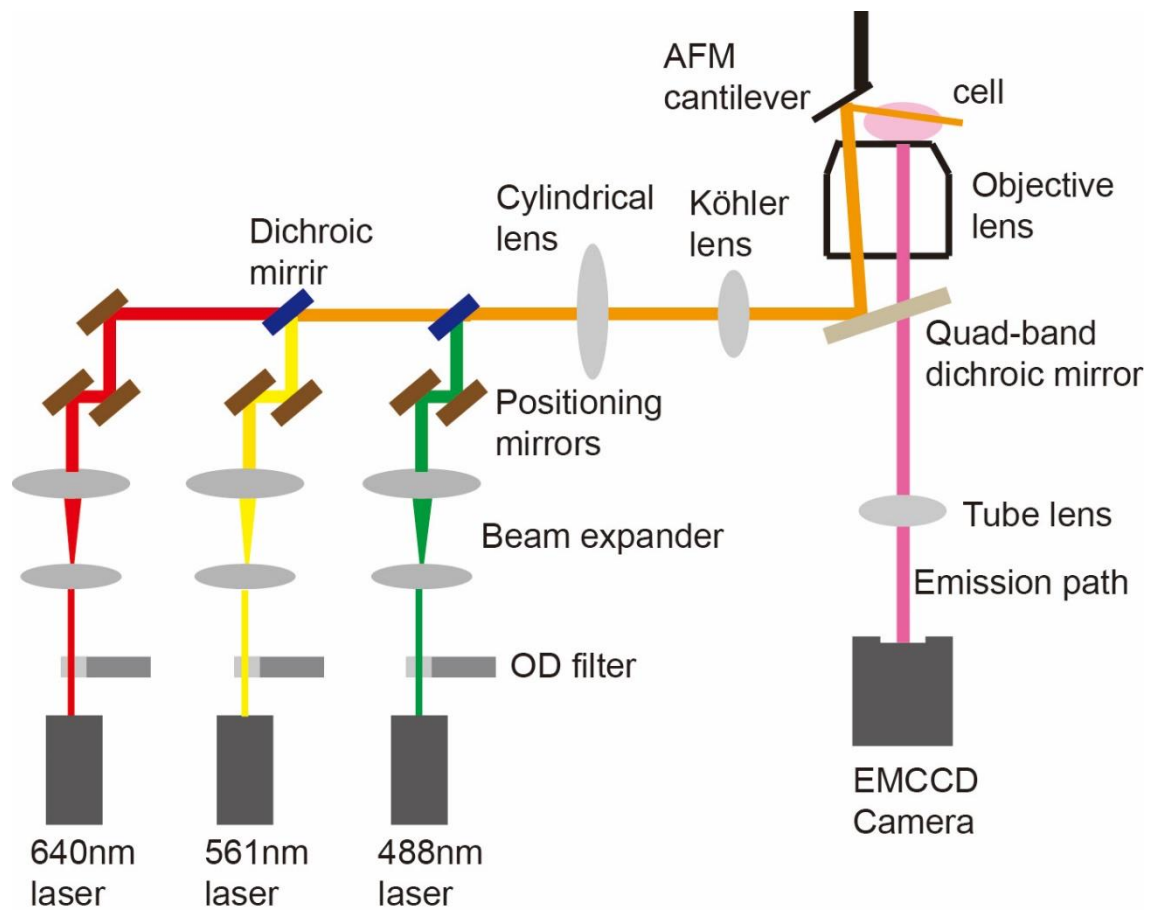
**Figure 2.2.** Schematic diagram of AFM cantilever reflected selective plane illumination microscopy. Three laser lines (640nm, 561nm and 488nm) are collimated expanded and coaxially combined in the common excitation path. Cylindrical lens and Köhler lens are used to generate and introduce the light sheet into objective lens. The AFM cantilever is put on top of coverslip to reflect the light sheet to cell samples. The emission fluorescence signal passes through the dichroic mirror and is refocused by tube lens to the EMCCD camera.

**Positioning mirrors**

Two or three adjustable mirrors are installed in each laser line after the beam expander to precisely control the position and direction of each laser beam, ensuring that all three laser beams are coaxially aligned in the combined common path and their illumination is co-localised on the sample.

**Multi-beam combiner**

Dichroic short wavelength reflecting and long wavelength passing mirrors, are used for multi-colour beam combination. In our set-up, three laser lines with wavelengths 640nm, 561nm and 488nm are arranged from left to right. Correspondingly, two dichroic mirrors are placed in the 561nm laser path and 488nm laser path (figure2.2). For the 561nm laser beam, the dichroic mirror can reflect the yellow laser light while being transparent to the red laser light. For the 488 laser beam, the dichroic mirror can reflect green light but is transparent to the yellow and red laser light.

**Cylindrical lens**

A cylindrical lens is used to generate the light sheet. When the collimated laser beam goes into a normal fourier lens, it will be focused in both the XY and YZ axes to generate a focused point at the lens' focal plane. When the collimated beam goes into a cylindrical lens, the beam is only focused in only one direction while the other direction remains collimated, resulting a light sheet in the focal plane instead a point.

**Kohler lens**

In SPIM or TIRF, the excitation beam should have a wide-field geometry. In order to achieve this, a Kohler lens is used to focus the excitation beam to the back focal plane of objective lens and generate a wide-field excitation geometry at the sample.

**Objective lens**

In contrast to conventional SPIM using two orthogonal lenses geometry to introduce the light sheet, our set-up is a single objective SPIM which means the objective is responsible for both light sheet excitation and fluorescence signal collection. High numerical aperture (NA) oil immersion lenses are used (NA =1.49 for 100X objective lens and NA = 1.27 for 60X objective lens) to gather maximum signal.

**AFM cantilever**

When the light sheet comes through the objective lens, it is vertical and perpendicular to the imaging plane. Therefore, it needs a mirror to reflect it 90 degrees forming a horizontal sheet and to go through cell samples from the side. The commercial AFM cantilever has a reflective aluminium coating and is able to work as a mirror to reflect the light sheet. Attached on a machined brass rod with an inclined surface of 43 degrees, it can be precisely controlled by a XYZ stage to a position above the incoming light sheet to reflect it onto cell samples.

## 2.1.1.2 Emission Pathway

**Separating the excitation and emission fluorescence.**

A quad-band dichroic mirror is used to reflect the excitation beam onto the objective lens while becoming transparent to the emission signals. Usually the quard-band dichroic mirror is embedded in to the microscope body and is suitable for most common laser lines including 640nm, 561nm, 488nm and 405nm.

**Re-focusing tube lens**

When the fluorophores in the sample are illuminated by the excitation beam and imaged by the objective lens, the output signal through the objective lens is collimated. In order to re-focus it to the camera imaging plane, the tube lens is used. The tube lens is also embeded inside the microscope body.

**Emission filters**

The signal to noise ratio (SNR) of the collected images is improved by using emission filters. The transmission wavelength band of the emission filters are chosen to match the emission spectrum of fluorophores, so that the background and noise is reduced and the imaging contrast is enhanced.

**Camera**

Electron mulitiplying charged-coupled device cameras (EMCCD) are most commonly employed in fluorescence microscopy. EMCCD cameras use electron multiplication to convert the signal emmited from photons on the detector, without amplifying the noise, and can have a more than 90% quantum efficeiency.

### 2.1.1.3 Supporting equipment

**Sample stage**

Biosamples are mounted on a stage which is designed to fit on a 35mm glass bottom petri dish. It is controlled by a 3D piezo that can move 200 μm in the XY direction and 100 μm in the Z direction with the resolution of 100 nm and a mechanical XY stage that can move 5cm. Coarse large distance movement is achieved by the mechanical XY stage, while fine movements are controlled by the piezo.

**Optical table**

The entire set-up including all the lasers, mirrors and microscope body is installed on a vibration-isolation damping optical table. Typically the damping optical table can isolate the the microscope from normal environment vibrations, including doors opening and closing and footsteps around the room.

**Live cell incubation unit**

The live cell incubation unit contains two subunits; one has heaters plus a plastic incubator that covers the sample stage to maintain a constant 37 degree celsius sample temperature, the other one is a carbon dioxide sensor plus carbon dioxide cylinder to keep introducing carbon dioxide into the incubator and maintain a 5% $CO_2$ atmosphere.

## 2.1.2 Components of the local delivery system.

In this section, core components of the nanopipette based local delivery system will be described. The local delivery system is developed from scaning ion conductance microscopy (SICM). SICM is a surface topography scanning microsope, using a hollow nanopipette whose tip diameter is less than 50 nm to sense the distance between nanopipette tip and sample surface. Since the nanopipette can not only localllize a certain position on a cell membrane but also has the cavity to load small molecules and macromolecules, we decided to adapt it to make a novel local delivery vehicle.

### Nanopipette as a delivery vehicle

The nanopipette is fabricated by a laser puller. Heated by a focused laser at its middle, a quartz capillary (1mm outer diameter, 0.5mm inner diameter with filament inside) can be equally pulled into two nanopipettes with controllable tip diameter. In our ldSPIM, two sets of tip size are used, one is ~100 nm inner diameter for samll molecule delivery and the other is ~400nm innner diameter for macromolecule delivery. The tip sizes are controlled by the pulling parameters such as the heating temperature, pulling force and speed. With the filament inside the nanopipette, liquid solution containing ions and delivering molecules can be filled into the nanopipette from the back. By either using a pressure or voltage pulse, molecules can be deposited out of the nanopipette onto the sample surface or inside the cell sample.

### Current amplifier

Since the size of the nanopipettes is less than 500nm, the ionic current passing through the nanopipette tip in PBS buffer under 100mV is at nanoampere or picoampere level. Therefore, a current amplifier (Axon Pitch 200b, USA) must be used. Either a commercialized patch clamp amplifier or a lock-in amplifier is used to record the ionic current , because their detection limit is less than one picoampere, which is capable of reading the ion current above the background noise. When connected to an external power source, the amplifier can also deposit molecules on to cell samples by generating a voltage pulse.

### Nanopipette positioning system

The nanopipette positioning system has two stages. One is the piezo stage, the nanopipette and its holder are mounted on a one dimensional piezo (10 μm range and 1nm minium stepsize) which precisely controls the distance between the nanopipette tip and sample surface based on

the feedback ion current. The piezo is also used to drive the nanopipette to penetrate the cell membrane and delivery molecules inside the cytoplasm. On the second stage, the pizeo plus nanopipette is mounted on a XYZ 3 dimensional manipulator (5cm travel and 1 μm minimum stepsize) which can rapidly locate the nanopipette at the center of the field of view.

**ldSPIM central controlling platform**

The movement of nanopipette including approaching the surface, membrane penetration and voltage driven delivery are controlled by a custom LabVIEW (National Instrument 2014) program implemented on a Field Programmable Gate Array (FPGA, National Instruments). The FPGA has 20 analog input/output channels (+/- 10V) through which the voltage can be sent or read directly by the program at ultra fast speed. In our set-up, two channels are used to control the movement of the piezo, one analog output line is used to give a continuously changing voltage to drive movement of the piezo and the other analog input line is used to read the real time position of the piezo. Another two channels are also connected to the patch clamp amplifier. The analog output line is used to introduce a voltage pulse and the analog input line is used to read the ion current from the patch clamp amplifier.
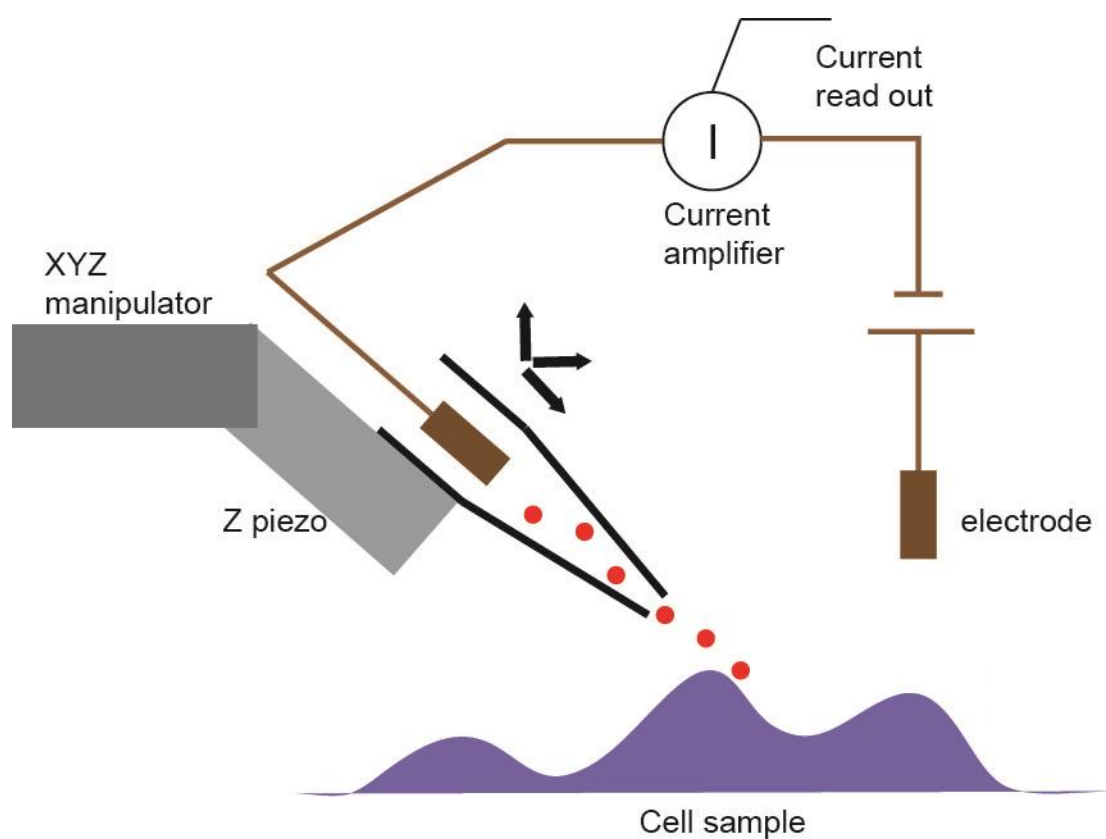
**Figure 2.3.** Schematic of nanopipette based local delivery. The nanopipette is controlled by two stages. The first one is a one dimensional piezo to bring the nanopipette close to the sample surface. The second is a XYZ stepper which rapidly moves the nanopipette to the rough center position of the field of view. An electrode is put inside the nanopipette and inside the media. A current amplifier is used to read the ion current as a feedback position signal.

## 2.2 Characterization of the ldSPIM

A series of proof-of-concept experiments were performed to demonstrate that ldSPIM provided four fundamental capabilities: 1) ldSPIM is able to locally deliver target molecules to a pre-defined position on sample surfaces; 2) the amounts of delivered molecules can be precisely controlled. 3) ldSPIM is capable of delivering single molecules. 4) ldSPIM can penetrate the cell membrane to deliver molecules into the cytoplasm. In these experiments we choose WGA as our model molecule to characterize the delivering function of ldSPIM. WGA is a positively charged molecule that it is able to binds to glycoconjugates on cell membrane as well as the negatively-charged glass surface. When cells are fixed, the glycoconjugates on the cell membrane become immobile so that deposited WGA molecules should be static, making it suitable for single molecule photo-bleaching analysis.

### 2.2.1 Local delivery to specific position

To demonstrate the accuracy of local delivery we firstly used the nanopipette to deposit Alexa-555 labelled WGA molecules at 24 dispersed coordinates in a circlular pattern and 25 dispersed coordinates of a star pattern on a glass surface, one by one. If ldSPIM is able to deliver WGA molecules to these predefined positions, the fluorescence signal of each point should replicate the pattern. The results in Figure 2.4 (a) and (b), show that the nanopipette delivered the Alexa-555 labelled WGA molecules to form the circle and star patterns. Furthermore, the actual deposited areas overlap well with the predefined coordinates labelled in blue spots, indicating that the nanopipette precisely delivered WGA molecules to a specific position.
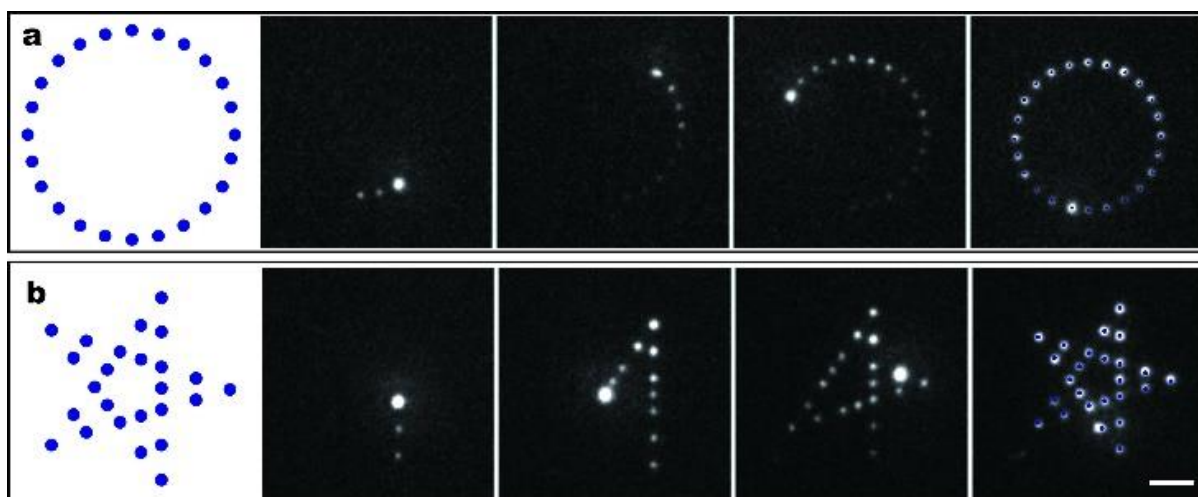
**Figure 2.4.** Accurate delivery of Alexa-555 labelled WGA molecules to specific position on glass surface forming different patterns. The coordinates of a circle and star, the delivering process and the overlay of coordinates and real deposited WGA molecules are shown in **(a)** and **(b)**. The scale bar is 20 μm.

Secondly, Alexa-555 labelled WGA molecules were delivered on the fixed HEK cell surface and the FWHM of the fluorescence intensity at the deposited area was calculated using the protocol described in chapter 2.3.9. The FWHM is used to estimate the size of the area occupied by delivered WGA molecules. Based on B. Babakinejad's work[96], where a nanopipette with ~100 nm diameter is used to deliver target molecules onto a surface using bulk delivery parameters, the simulated FWHM of the deposited area is given by

$$\text{FWHM} \approx 2\sqrt{3}\ h \qquad\qquad\qquad \textbf{Equation (1)}$$

In **Equation (1)**, h is the distance between the sample surface and nanopipette. In my experiment, h is maintained at ~200 nm when the delivering protocol was operated. Therefore, the theoretical FWHM of the fluorescence intensity at the deposited area occupied by Alexa-555 labelled WGA molecules should be ~0.7 μm. If the measured FWHM values are close to the theoretical value, this suggests that the new system is capable of delivering target molecules to the position just underneath the nanopipette rather than other areas on the cell surface.

The labelled WGA molecules were delivered onto three different fixed HEK cell surfaces using bulk delivery parameters. On each cell, the bulk delivery and intensity measurement protocols were repeated ten times to calculate the average and standard deviation of the FWHM value. The results are plotted in a box chart in Figure 2.5. In the box chart, the FWHM values vary

from 550 nm to 800 nm on three different cells and the average values are around 650 nm, which is close to the theoretical value. This suggests that the local delivery and image system could dose molecules to the area just underneath the nanopipette. The difference value of FWHM on three fixed cells is probably due to the different cell topography, which will make the distance between the cell surface and the tip of nanopipette different.
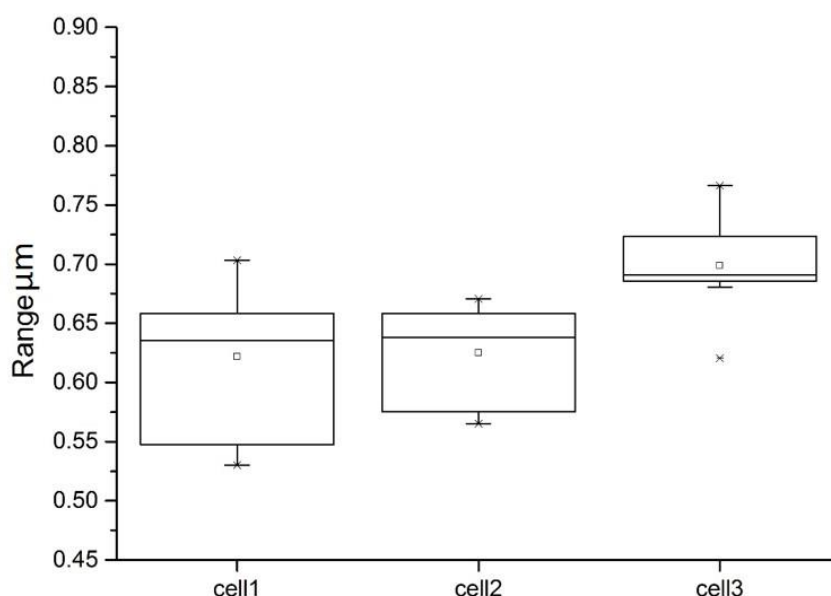


**Figure 2.5**. FWHM values of the deposition area of Alexa-555 labelled WGA molecules on three fixed HEK cell surfaces. On each cell, Alexa-555 labelled WGA molecules were delivered and measured ten times. The FWHM values vary in a narrow range with small standard deviation and the averages are close to 650nm for all three cells.

**2.2.2 Controlling the amounts of molecules deposited**

When a voltage pulse is used to deposit molecules onto a sample surface, there are three parameters that can affect the amount of delivery: the concentration of Alexa-555 labelled WGA molecules in the PBS buffer, the magnitude of the voltage pulse and the pulse dwell time. When a nanopipette is loaded with a certain concentration of WGA solution, it cannot easily be washed and reloaded with a different concentration of WGA solution. Therefore, if we want to use a different concentration of Alexa-555 labelled WGA PBS buffer, we must keep replacing the nanopipette. However, this introduces the inner diameter of the nanopipette as another variable. Based on these two facts, the concentration was kept constant and the magnitude of voltage pulse and the pulse dwell time independently varied in experiments depositing Alexa-555 labelled WGA molecules on a fixed HEK cell surface.

The dwell time was first set at 2s as a constant and voltage pulses with different magnitudes varying from 0 to 900 mV were applied to deliver Alexa-555 labelled WGA molecules. Then voltage value was set at 600 mV and different dwell times, varying from 0 to 7 s, were applied. For each voltage and time value, the delivering protocol was repeated ten times to acquire the average and standard deviation. In contrast to the previous  deposition process where one voltage or time value was repeated ten times before moving to the next value, this experiment consisted of a voltage ramp from 0 mV to 900mVor a time ramp from 0 s to 7 s and repeating the ramp ten times to acquire the average and standard deviation. The fluorescence intensity within the deposited areas was calculated by the method described in chapter 2.3.9 and plotted with the corresponding voltage value and dwell time shown in Figure 2.6. Figure 2.6 (a) - (b) show that the fluorescence intensity of the delivering area could be fitted linearly with different voltage pulse values and pulse dwell times. Most of the standard deviations are less than 20%, indicating that the performance of nanopipette delivering protocol is reliable and repeatable. The linear fit seems to represent the data accurately and the $R^2$ value is close to 1, making the fitting equation a convincing calibration curve. In addition, different nanopipettes and fixed HEK cells were used to repeat this quantitative characterization (Figure 2.6 (c) – (d)). The fluorescence intensity could also be fitted linearly with different voltage pulse values and pulse dwell times under different conditions. The only difference is the slope of the fitting curve. This is because the inner diameter changes slightly from pipette to pipette and the surface conditions are not the same on different fixed cells. Although the slopes of different cells were different, the $R^2$ value was close to 1. Based on these linear calibration curves, it is possible to

claim that once the concentration of delivered molecules is known, the amounts of delivered molecules could be controlled precisely by applying different voltage pulse values and pulse dwell times.
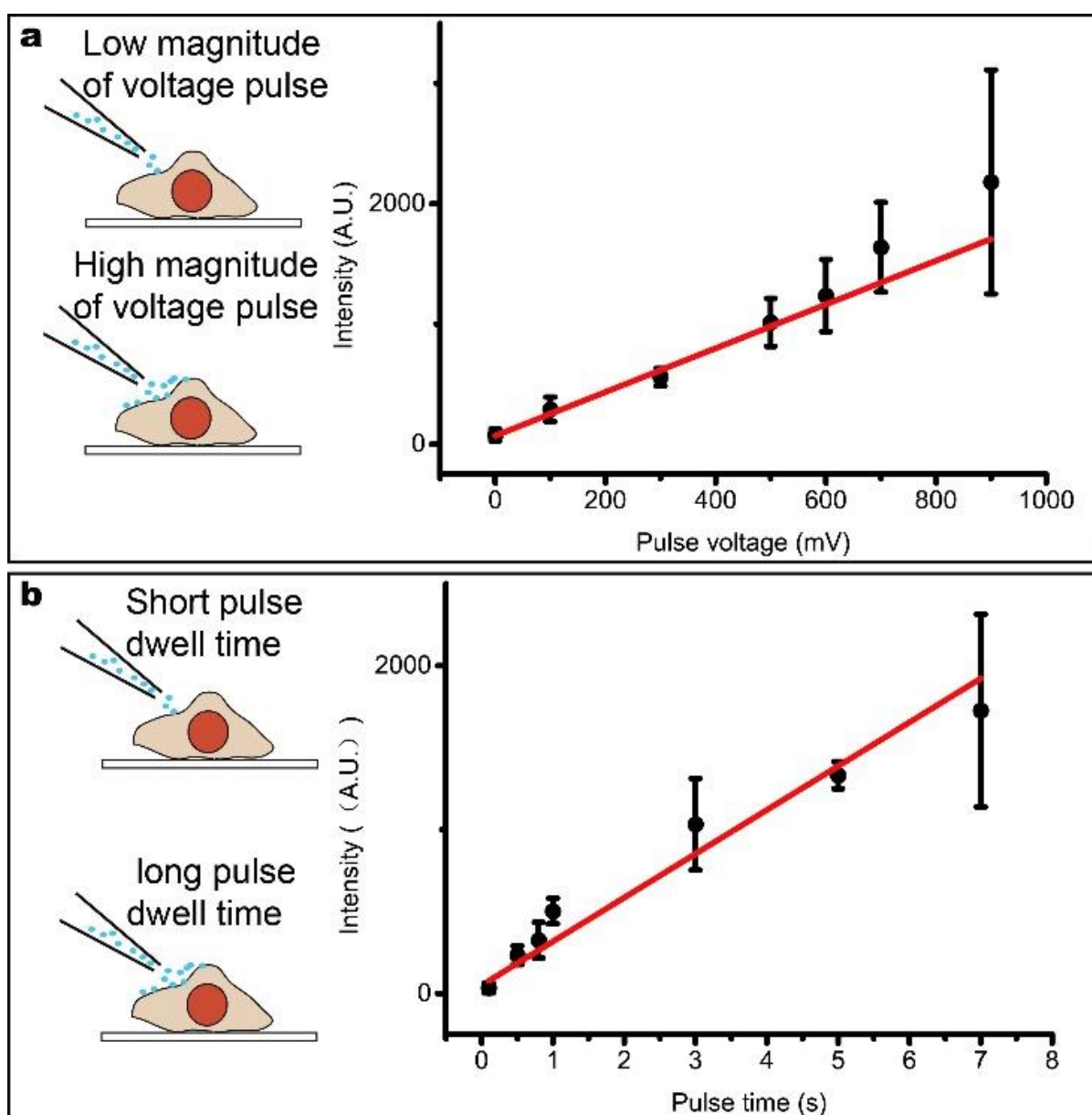
**Figure 2.6.** The amount of Alexa-555 WGA molecule deposited on fixed HEK cell surface is fine-tuned by adjusting the magnitude of voltage pulse and pulse dwell time. Here we use the fluorescence of Alexa-555 WGA molecules deposited on fixed HEK cell surface to represent the amount. **(a)** When the pulse dwell time is fixed at 2s, the fluorescence of deposited Alexa-555 WGA molecule increases linearly when raising the pulse voltage from 0 mV to 900mV. **(b)** When the pulse voltage is a constant of 600mV, the fluorescence of deposited Alexa-555 WGA molecule also has a linear relationship with increase of pulse dwell time from 0s to 7s. The error bar in both **(a)** and **(b)** represents the standard deviation of 6 repeats of each parameter on the same fixed HEK cell.

### 2.2.3 Single-molecule delivery

The capability to deposit single molecules onto the cell surface was demonstrated by depositing Alexa-555 labelled WGA molecules onto the surface of fixed HEK cell. Using a set of delivery parameters for single-molecule delivery, a single spot was delivered onto a fixed HEK cell surface and then was imaged until it photobleached (Figure 2.7(a)). The number of molecules delivered was determined by observing the photobleaching of Alexa-555 (Figure 2.7 (b)). In Fig. 4b, two photobleaching steps could be observed, indicating that there are two Alexa-555 fluorophores on the WGA molecules. Since the degree of labelling of the WGA was 1.6 on average, this result demonstrates the ability to deliver single WGA molecules (on average two dye molecules are corresponding to one single WGA molecule). The single-molecule deposition protocol was repeated 30 times using the auto delivery and imaging algorithm and over half of the replicates showed that on average only one or two single Alexa-555 labelled WGA molecules were deposited on the fixed HEK cell surface (Figure 2.7 (c)).
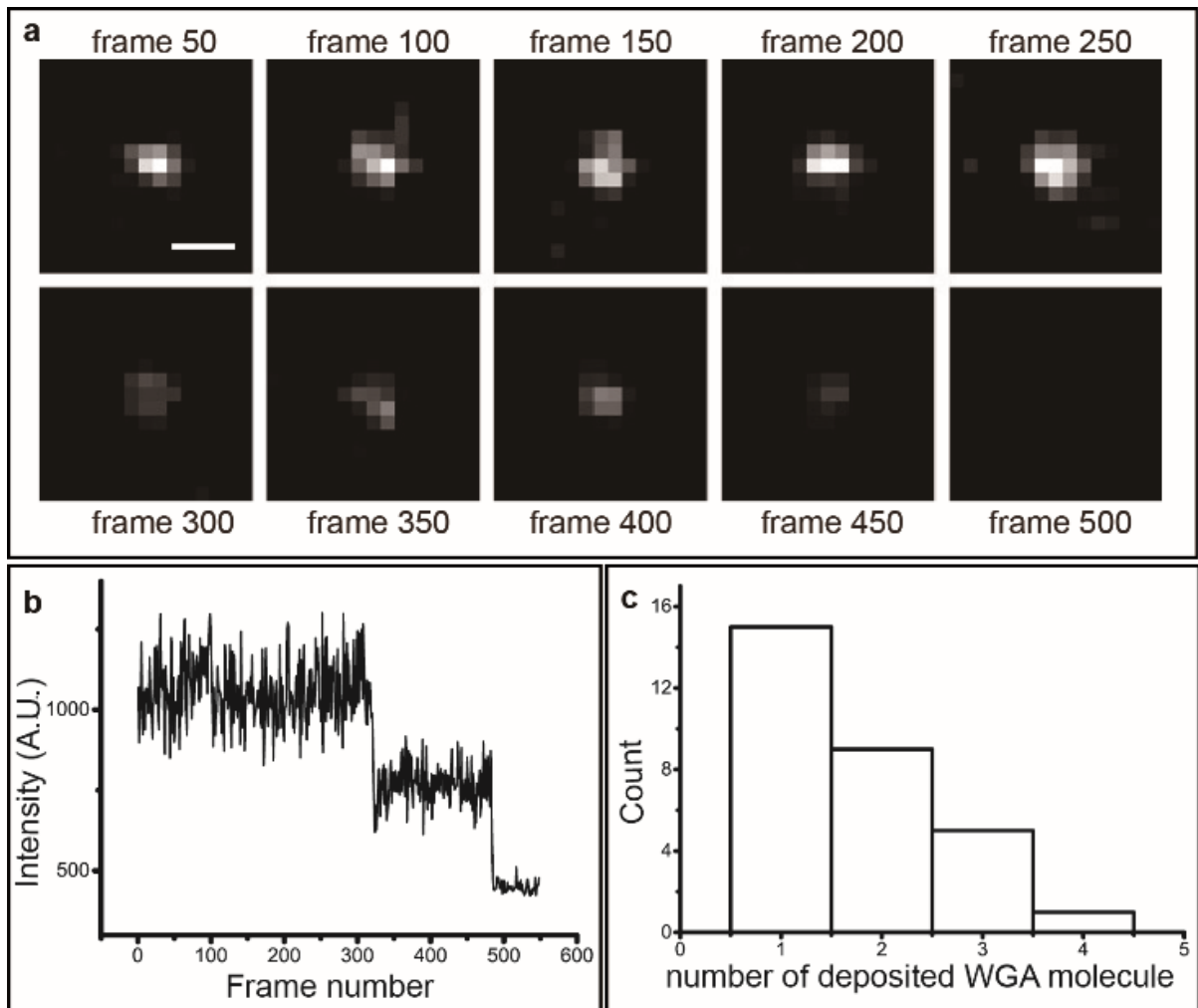
**Figure 2.7.** Single Alexa-555 labelled WGA molecules deposited on fixed HEK cell surface. **(a)** Photobleaching of a deposited WGA molecule. **(b)** Intensity profile of the WGA molecule bleached in **(a)**. The intensity decreases in two steps suggesting the presence of two Alexa-555 dye molecules. As the degree of labelling of our WGA molecules is 1.6:1, this approximately corresponds to a single WGA molecule in **(a)**. **(c)** The distribution of the average number of deposited Alexa-555 WGA molecule over thirty replicates. The scale bar is 500 nm.

## 2.2.4 Intracellular injection

Besides surface delivery, ldSPIM is also able to achieve intracellular deposition by penetrating the cell membrane, followed by direct delivery of molecules into the cytoplasm using a voltage or air pressure pulse. We used Alexa-647 dye (Figure 2.8 (a)) and Alexa-594 labelled α-synuclein aggregates (Figure 2.8 (b)) to demonstrate that ldSPIM can not only introduce small molecules, but also relevant big protein oligomers or aggregates inside the cytoplasm. Before nanopipette penetration, the cell was black without any fluorescence. Once the nanopipette was inserted into the cell, the fluorescence at the tip of nanopipette could be identified as a bright spot inside the cell. During the injection process, the cell was illuminated with fluorescence from Alexa-647 and Alexa-594 labelled α-synuclein aggregates, while the background remain dark. The fluorescence intensity profile of the injected cells changed synchronously with the injection process (Figure 2.8 (c) and (d)). Alexa-647 is small molecule so the fluorescence was uniform and was observed over the whole cell including the nucleus. In contrast, the larger synuclein aggregates could not enter the nucleus. There are also some brighter spots left over the injection point. Since the size of nanopipette's aperture is around 100 nm, it can specifically introduce large aggregates into cytoplasm without affecting the nucleus.
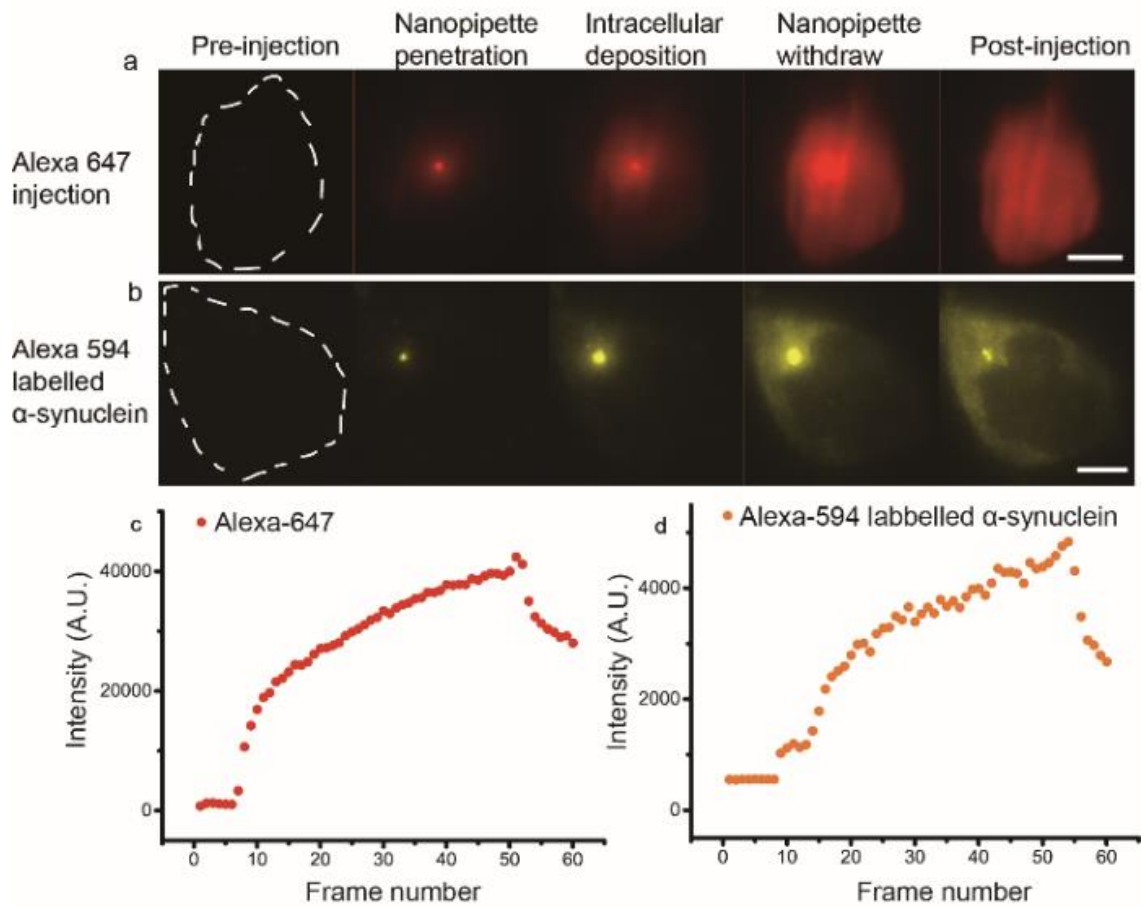
**Figure 2.8.** Nanopipette delivery into live cells. Intracellular deposition of Alexa-647 and Alexa-594 labelled α-synuclein aggregates over time are shown in **(a)** and **(b)**. The dashed lines indicate the outline of the cells. The fluorescence intensity of the deposited molecules inside the cell over injection process are shown in **(c)** and **(d)**. The fluorescence intensity of the whole cell selected in dashed lines increased near frame 10 and kept rising until frame 50 representing the nanopipette penetration and continuous deposition of Alexa-647 and Alexa-594 labelled α-synuclein aggregates. The decrease near frame 55 indicates the withdrawing of nanopipette. The scale bar is 4 μm.

## 2.3 Material and method

### 2.3.1 Single objective cantilever selective plane illumination microscope (socSPIM)

The detailed experimental procedure of single objective cantilever selective plane illumination microscope (socSPIM) imaging has been published[95]. The socSPIM was implemented on a standard inverted microscope (Eclipse TiU, Nikon) with an internal magnification of 1.5×. Fibre-coupled 488 nm (15 mW iFLEX2000, Qioptic), 561 nm (50 mW DPL561, Cobolt) and 640 nm (20 mW iFLEX-2000, Qioptic) diode laser lines and excitation filters (FF01488/625, LL02-561-25 and FF01-640/14-25 Semrock) were used. The illumination power density was controlled by neutral optical-density (OD) filters, Galilean beam expanders which contain two lenses which were used to increase the field of view that can be excited and imaged. The distance between the two lenses is equal to the sum of the two focal lengths in order to maintain the beam collimation. At least two adjustable mirrors were put in each laser path to precisely control the position and angle of the beam so that they can be aligned coaxially in the combined beam path. A cylindrical lens in the combined beam path was used to generate the light sheet and a commercial AFM cantilever (ContAl-G, BudgetSensors), which has a reflect aluminum coating, was attached onto a machined brass rod using cyanoacrylate adhesive to reflect the light sheet onto the cell sample. Either a 100× (150x with internal magnification) 1.49 numerical aperture (NA) oil immersion objective lens (MRD01991, Nikon) or a 60x (90x with internal magnification) 1.49 NA oil immersion objective lens (MRD01991, Nikon) was used to focus the light sheet to the cell and collect the fluorescence emission. An UltraFlat quad-band dichroic mirror (ZT405/488/561/640rpc-UF3, Chroma) was used in the microscope to separate excitation and emission. The emitted fluorescence was filtered by emission filters (LL02- 561-25, Semrock or #67-038, Edmund Optics) and focused onto the EMCCD camera (Evolve 512 Delta, Photometrics) using a tube lens. The sample stage was controlled by an XYZ piezo (P-611.3 Nanocube, Physik Instrumente) to enable 3D scanning with the scanning step 100nm and frame rate at 0.2 Hz. The scanning data was first assembled as a hyperstack and then reconstructed as a 3D projection or 3D volume rendering using the 3D projection function and 3D viewer plugin in FIJI where the threshold is 40 and resampling factor is 1, respectively.

### 2.3.2 TIRF and HILO imaging

The excitation and emission path of TIRF and HILO is similar with socSPIM. The only difference is that TIRF and HILO do not need a cylindrical lens to generate the light sheet. Fibre-coupled 488 nm (15 mW iFLEX2000, Qioptic), 561 nm (50 mW DPL561, Cobolt) and excitation filters (FF01488/625 and LL02-561-25 Semrock) were used. The OD filter, Galilean beam expanders and adjustable mirrors were also used for the control of beam intensity, size and position. A 100× (150x with internal magnification) 1.49 numerical aperture (NA) oil immersion objective lens (MRD01991, Nikon) which was embedded in an inverted microscope was used to focus the laser beam and collect the emission fluorescence. The laser beam was incident at an angle larger than the critical angle of glass/water interface when focused at the back focal plan of objective lens to achieve total internal reflection. When using HILO mode the incident angle was smaller than TIRF and an iris was used for optimal section. TIRF and HILO were used when the functions of local delivery and intracellular injection were characterized. This is because it is much easier to image and analyse the AF555-labelled WGA molecules deposited on glass or cell surface as well as inside the cytoplasm using TIRF and HILO than light sheet.

### 2.3.3 Nanopipette fabrication

Nanopipettes were fabricated from quartz capillaries (Sutter Instrument outer diameter 1mm inner diameter 0.5 mm with filament, CA, USA) using a laser pipette puller (P-2000, Sutter Instruments, Novato, CA). Two sets of parameters were used to pull pipettes with different opening sizes. The size of nanopipettes pulled using these parameters were characterised using scanning electron microscopy (SEM) as previously reported[39,40,97]. Parameter 1 (Line1 Heat=400, Fil=3, Vel=30 Del=220 Pull=0; Line2 Heat=450, Fil=2, Vel=20 Del=180 Pull=255) was used to produce the nanopipette with ~100 nm inner diameter and ~200 nm outer diameter. These nanopipettes were used for small molecule delivery such as labelled Wheat Germ Agglutinin (WGA). In PBS buffer its electronic resistance was 150-200 MΩ. Parameter 2 (Line1 Heat=300, Fil=3, Vel=30 Del=220 Pull=0; Line2 Heat=350, Fil=2, Vel=20 Del=180 Pull=255) was used to produce the nanopipettes with 300-400 nm inner diameter and 600-800 nm outer diameter. This larger nanopipette was used for delivery of protein aggregates. Its electronic resistance was 40-80 MΩ.

### 2.3.4 Wheat germ agglutinin (WGA) delivery on glass and fixed cell surfaces

A nanopipette with ~100 nm aperture was backfilled with 8 µL positively charged Alexa-555 labelled WGA (Thermo Fisher) at a concentration of 9 µM for bulk delivery and 450 nM for single-molecule delivery in PBS buffer, with an Ag/AgCl electrode. The pipette was immersed into a bath of PBS buffer, which contained an untreated glass surface or cell sample, while another Ag/AgCl electrode served as the reference electrode. A -100mV potential bias from the patch clamp amplifier was applied between the electrodes inside the nanopipette and bath preventing WGA molecules escaping from the nanopipette. This generated a current of approximately 0.4 nA. A custom LabVIEW (National Instrument 2014) program implemented on a Field Programmable Gate Array (FPGA, National Instruments) was used to control the deliver process. The nanopipette was first moved down to a position ~15 µm above the sample surface using the white light microscope. Then the piezo moved the nanopipette down to the target area at a speed of 25 µm/s and the ion current was recorded in FPGA at the same time. Based on our previous work[26], when the nanopipette gets close to the sample surface the ionic current decreases exponentially. The ionic current vs tip-surface distance curve is shown in Figure. 1.6. When the ionic current drops by 2%, the nanopipette approaches a position 200 nm above the sample surface. Once the nanopipette had approached this position, the piezo stopped moving and maintained the nanopipette position above the sample surface. Positive voltage or air pressure pulses with different amplitudes and dwell times were applied to deliver specific amounts of Alexa-555 labelled WGA molecule onto the sample surface. It was found that the magnitude voltage can be tuned more precisely using the FPGA than using an air pressure pulse controlled by mechanical pump.

### 2.3.5 α-synuclein deposition

The procedure of protein aggregate deposition was similar to that used for Alexa-555 labelled WGA. However, different size nanopipettes and applied voltages were used. The nanopipette which was used to deliver protein aggregates has an aperture size of ~300-400 nm and was backfilled with 8 µL of negatively charged 1.4 µM α-synuclein in PBS. A +100mV voltage bias was applied between the electrodes inside the nanopipette and the bath, generating a +2nA ionic current. When the nanopipette approached the cell surface, a negative voltage pulse (-500mV, 10s for α-synuclein) was applied to drive protein aggregates out of the nanopipette.

### 2.3.6 Dye and α-synuclein oligomer injection into a live cell

The injection process used the same approach procedure as for local delivery. Once the nanopipette had approached the cell surface, the piezo moved the pipette down by an extra 5 μm in one step to penetrate the cell membrane. The penetration depth was 5 μm because the nanopipette needed enough force to penetrate the cell membrane and if the depth was less than 5 μm it was found that the nanopipette would not insert into the cytoplasm. The HEK cell has a height of ~10 μm (measured by moving the focal plane between the upper and bottom cell surface), so a penetration depth larger than 5 μm resulted in damage to the cell and potentially crushing of the nanopipette tip. Once the nanopipette had penetrated the cell membrane, a voltage pulse (-500mV, 10s) was applied to force the molecules out of the nanopipette and into the cytoplasm. After the injection process was finished, the nanopipette was retracted back by 5 μm in one step preventing the penetrated cell sticking on the nanopipette and moving up with it.

### 2.3.7 α-synuclein preparation

70 μM α-synuclein monomer, expressed and purified in E.coli[98–100] was shaken at 37 °C for 24 hours in order to produce a solution containing α-synuclein aggregates.

### 2.3.8 Cell culture

Human embryonic kidney cells (HEK) are cultivated on plasma cleaned glass slips in DMEM (Dulbecco's Modification of Eagle's Medium) with 4.5g/L glucose, L-glutamine and sodium pyruvate at 37 °C.

### 2.3.9 Fluorescence intensity measurement of deposited Alexa-555 labelled WGA molecules

After nanopipette deposition, the illuminated Alexa-555 labelled WGA molecules occupied an approximate circular area on the fixed cell surface (Figure 2.9). We fitted the fluorescence

intensity using a Gaussian distribution and used the full width at half maximum (FWHM) to estimate the average fluorescence of the deposited Alexa-555 labelled WGA molecules. In order to make the Gaussian fitting more accurately, the data fitted was selected from a thin section crossing the centre of the deposited area with 3 pixels in width and 100 pixels in length (Figure 2.9 (b)). Then the average intensity was plotted along the x axis and fitted to the following Gaussian equation (**Equation (2)**).

$$Y = a + (b - a)e^{\frac{-(x-c)^2}{2d^2}}$$ **Equation (2)**

In Equation (1), $a$ is the value of background intensity, b is the peak intensity, (b-$a$) is the real peak height and was used to represent the fluorescence intensity of delivered Alexa-555 labelled WGA molecules. c is the position and d is the width of the Gaussian distribution. This was used to calculate the FWHM (**Equation (3)**) and estimate the size of the delivering area.

$$\text{FWHM} = 2\sqrt{2\ln2}\, d \approx 2.355\, d$$ **Equation (3)**

**Equation (3)** describes the relationship between FWHM and standard deviation ($d$). The camera pixel size is 16 μm, resulting in an effective pixel size of 106.7 nm with 150x magnification and therefore the size of the FWHM is calculated by **Equation (4)**

$$\text{FWHM} = 2.355*d*16\mu m/150$$ **Equation (4)**
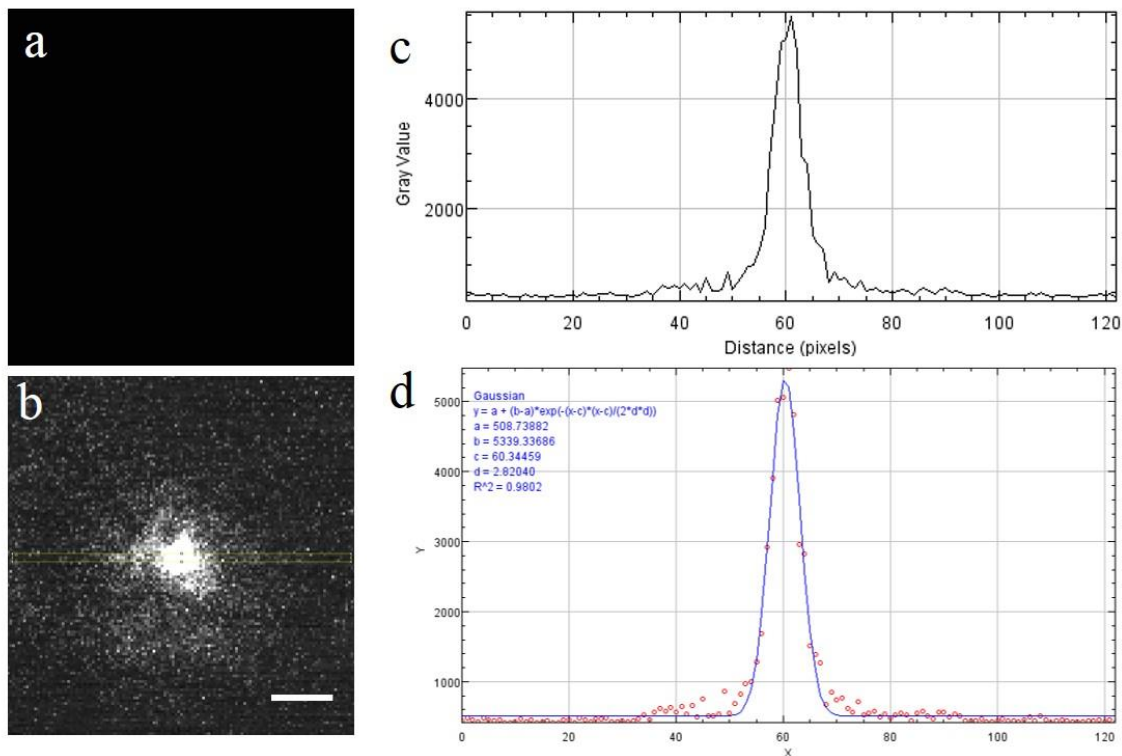
**Figure 2.9.** Deposition of Alexa-555 labelled WGA molecules on a fixed HEK cell surface and the intensity distribution. **(a)** The background before delivering **(b)** A thin section with 3 pixels in width and 100 pixels in length is selected cross the centre of fluorescence image of delivered WGA molecules. Scale bar is 2μm. **(b)** The average intensity of distribution along the X axis in the selected section. **(c)** The Gaussian fitting of the intensity curve, the parameters in the fitting equation are used to calculate peak height and FWHM.

### 2.3.10 Single molecule delivery and analysis

450 nM ALEXA-555 labelled WGA molecules were delivered to fixed HEK cell surface using a -300mV, 5s voltage pulse to demonstrate single-molecule delivery. After the delivery protocol was finished, one or more bright spots could be observed on the fixed cell surface. Image acquisition was continued with laser excitation until all fluorophores were photobleached. When one dye molecule photo bleached, the fluorescence intensity decreases instantly and there is a step function change in the intensity profile. The number of steps in the intensity profile corresponds to the number of dye molecules in one spot. UV-Vis spectra was used to define the average number of Alexa-555 dye molecules on each labelled WGA molecule. The Alexa-555 molecule has an absorption value of 1.309 Abs at 555 nm, and the WGA molecule has a 0.256 Abs absorption value at 280 nm. Based on the correction coefficient (0.08 for Alexa-555 molecule) and the absorption coefficients of Alexa-555 and WGA molecule (150000 $m^2$/mol for Alexa-555 and 28420 $m^2$/mol for WGA), the concentration of both molecules can be calculated using **Equation (5)**.

$$A = \varepsilon cl \qquad\qquad\qquad\qquad\qquad \textbf{Equation (5)}$$

A is the absorption value, $\varepsilon$ is the absorption coefficient and l is the path length (fixed as 0.1 cm). The concentrations of Alexa-555 and WGA were 87 μM and 53 μM. The concentration ratio is around 1:1.6, suggesting that one WGA molecule was labelled by 1.6 Alexa-555 molecules, on average. Approximately, if two Alexa-555 dye molecules are detected on fluorescence intensity profile then there should be one Alexa-555 labelled WGA molecule. We also designed an auto delivery and imaging algorithm using LabVIEW and JAVA script to repeat the single-molecule delivery protocol rapidly.

### 2.3.11 Automatic single molecule delivery algorithm

First, the micromanager software sends commands to the EMCCD to generate a digital trigger. Then this trigger is transferred by BNC cable to the FPGA digital input channel. Once the FPGA receives this digital trigger, it first turns on the laser at the power of 5800 W/cm$^2$ for 5 s to bleach all fluorophores on the cell surface. Then the FPGA turns off the laser and starts controlling the nanopipette to approach the cell surface and applies the single molecule

delivering protocol to deliver Alexa-555 labelled WGA molecules to the fixed cell surface. When the delivery protocol is finished, the FPGA turns on the laser again and generates a laser beam with 126 W/cm$^2$ power for single-molecule imaging. At the same time, the FPGA also generates a digital trigger and sends it back to the EMCCD. The EMCCD receives this trigger and takes 500 frames of image (three dye molecules need no more than 400 frames to be bleached, therefore 500 frames is sufficient to ensure that all delivered dye molecules can be bleached) until all dye molecules are bleached. This process can be repeated indefinitely to generate large amounts of single molecule delivery data.

## 2.4 Discussion

We have demonstrated that by combining nanopipette and light sheet 3D scan imaging, we developed a novel multifunctional microscopy, local delivery selective plane illumination microscopy (ldSPIM). Through four proof of concept experiments, we demonstrate that ldSPIM is capable of delivering single or precisely tuned amounts of biomolecules to specific locations on a single live cell. The experiments also show that ldSPIM can perform intracellular injection of dye molecules, as well as protein aggregates. The most notable advantage of ldSPIM is that it is the first instrument that is able to perform precise local delivery in combination with high-resolution light-sheet microscopy with single molecule sensitivity.

In the future the ldSPIM can be improved in two additional aspects. Firstly, the ldSPIM uses a single barrel nanopipette, which is only able to deliver one kind of molecules to a location at a time. If two reagents are required to be delivered to a same position, two different nanopipettes must be used to finish the deposition separately. This will make time sensitive experiments very difficult and introduce the pipette size as an extra variable. Secondly, the light sheet used in ldSPIM is reflected by an AFM cantilever which occupied the vertical space above the sample. It is challenging to add another detection method such as patch-clamp due to the limited space. A double or more barrel nanopipette[35] will be used to address the first issue. The double barrel nanopipette has two independent channels in one capillary so it is able to deliver two kinds of molecules e.g. AF594-labelled α-synuclein and Alexa-647 labelled amyloid-β to one or more locations e.g. cytoplasm and nucleus at the same time. Optimizing the optical pathway to achieve a new version of light sheet microscopy[101–103] without using a mirror to reflect the beam and removing the AFM cantilever will release more space, allowing more functionality in a single experiment and compatibility with well plates for high-throughput studies. Such an instrument is discussed in Chapter 5.

# Chapter 3
# The application of ldSPIM in Toll-Like-Receptor 4 (TLR4) activation

This chapter describes the application of ldSPIM in TLR4 activation and quantitative characterization of the formation of the downstream signaling complex, the Myddosome. Using ldSPIM, the lipopolysaccharide (LPS) and sonicated $A\beta$ aggregates were locally deposited onto the surface of MyD88 -/- immortalised bone marrow derived macrophages (iBMMS) transduced with MyD88-GFP . With the light sheet scan, the assembly of MyD88 oligomers after TLR4 activation was visualized in live cells in 3D for the first time.

The kinetics of MyD88 oligomer formation was analysed and compared between LPS and sonicated $A\beta$ fibrils triggering in the following five aspects: 1) the first time point when the Myddosome formed, 2) the Myddosome lifetime, 3) the total number of oligomers formed within 30mins upon triggering, 4) the Myddosome size and 5) the variation of MyD88 oligomer size with stimulation time.

**Contribution**

Bing Li imaged all cells and analysed the data. Dr. Jack Brelstaff and Dr. Lee Hopkins made the virus transduced MyD88-GFP macrophage**.** Prasanna Suresh helped with 2D tracking code to track each newly formed Myddosome

## 3.1 LPS triggered TLR4 Myddosome formation

According to our group's previous work, Latty *et al* demonstrated that when the canonical TLR4 agonist, LPS, was added into the cell growth media, TLR activation in MyD88-GFP transduced macrophages could be visualised through the assembly and disassembly of the Myddosome using total internal reflection fluorescence microscopy (TIRFM) within 10mins of stimulation[104].

I repeated this simulation using a nanopipette to deposit LPS to a single macrophage. In this experiment, 1 µg/ml LPS was loaded into the nanopipette and delivered onto the surface of a single macrophage with GFP-tagged MyD88. The formation of the Myddosome was imaged by TIRF. In unstimulated macrophages (PBS control), GFP-tagged MyD88 diffused freely in the cytoplasm or near the cell membrane (Figure 3.1) while macrophages that were activated by delivered LPS showed a gradual increase in the intensity of puncta, which was interpreted as Myddosome formation (Figure 3.2). The first Myddosomes formed 50 s post LPS triggering and continued for the next 300 s (Figure 3.2(a) – (g)). At 400 s post triggering, Myddosomes started to disassemble gradually (Figure 3.2(h) – (l)). The assembled Myddosomes either rapidly disappeared from the field of view after 50s, or were sustained for more than 10 min. These results were consistent with Latty's previous work[84]. This indicates that the nanopipette and the delivery protocol did not affect the properties of delivered molecules, suggesting that this system does not interfere with cell biology thus is applicable for depositing molecules onto single cells.

The number of MyD88 molecules in these formed Myddosomes was also analysed by comparing the fluorescence intensity of assembled Myddosome to the intensity of GFP monomer under the same illumination condition. The results showed that signal intensity of the Myddosome is approximately $5 \pm 1$ times that of the GFP monomer, which correlates with the 6 MyD88 molecules observed in the Myddosome crystal structure.
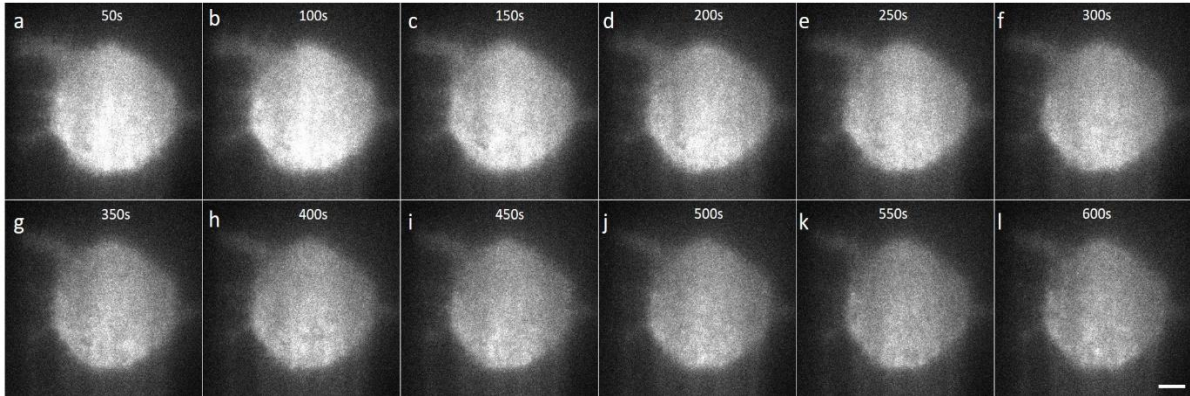
**Figure 3.1.** TIRF images of Macrophage with PBS control. (a)-(l) show the freely diffused GFP-tagged MyD88 without the formation of Myddosome. The scale bar is 2 μm.
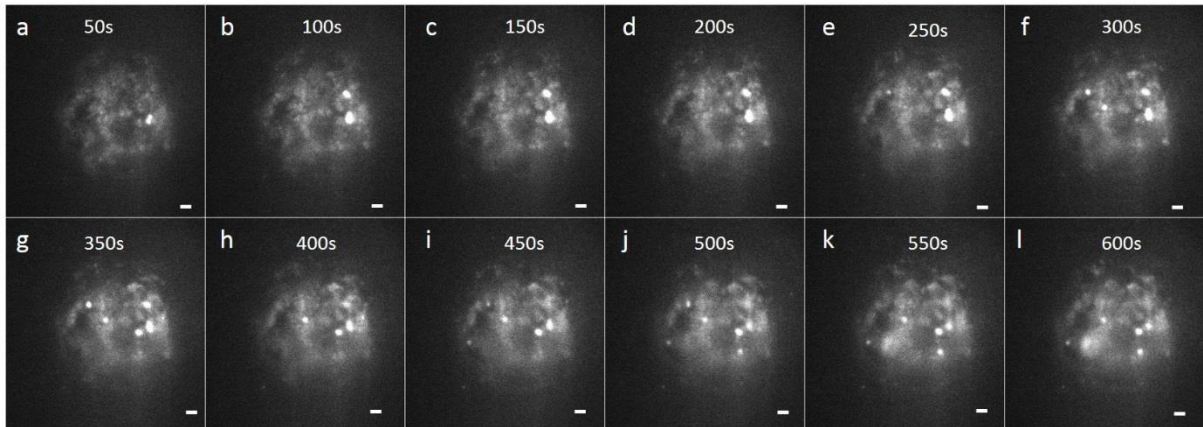


**Figure 3.2.** TIRF images of Myddosome formation triggered by delivered LPS. **(a) - (g)** show the process of Myddosome formation. **(h) – (l)** show the process of Myddosome disassembly. Scale bar is 2 μm.
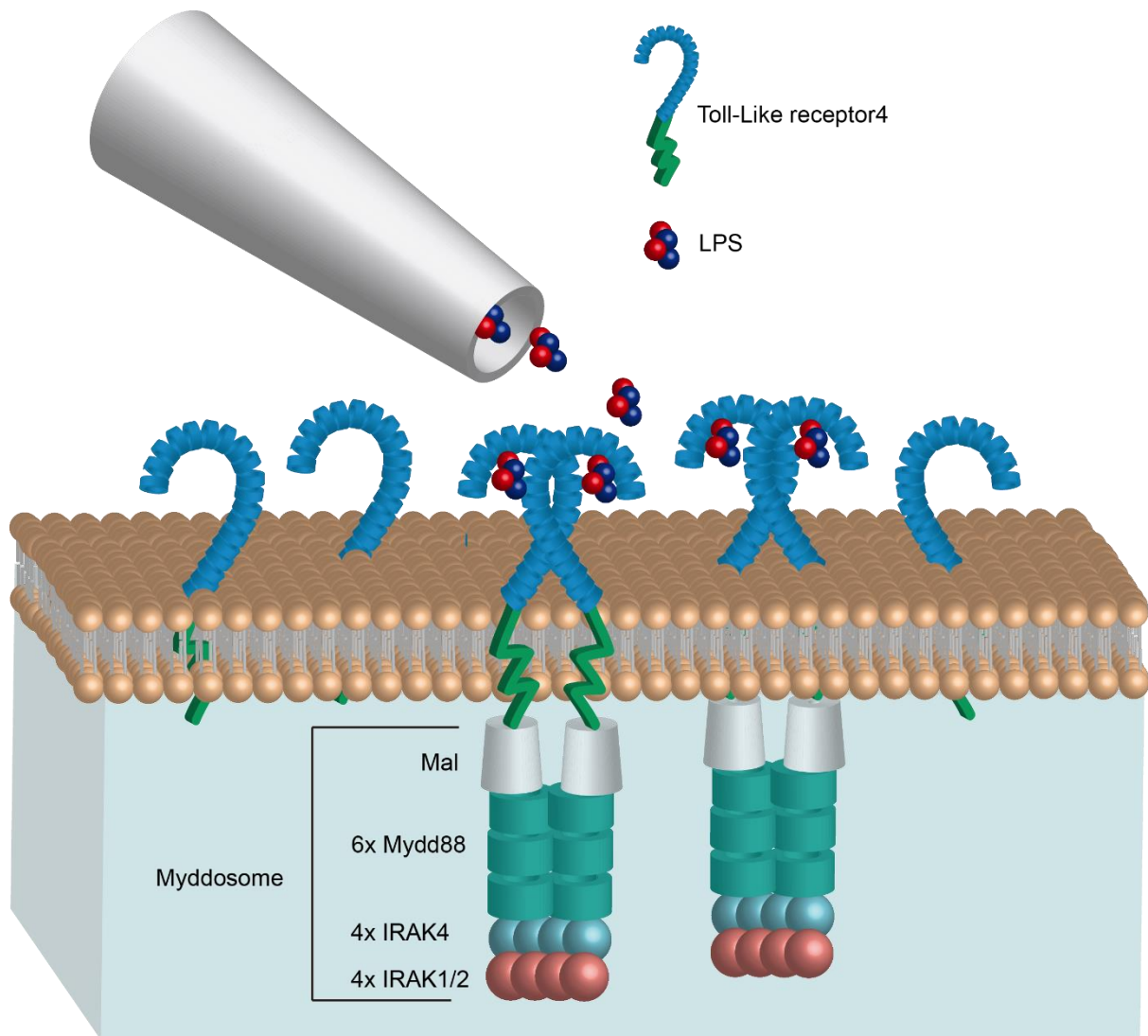
**Figure 3.3.** Schematic of Nanopipette delivered LPS triggered TLR4 Myddosome formation. The LPS is delivered by nanopipette to the macrophage surface. When LPS binds to TLR4, it will trigger the dimerization of TLR4, which activates the recruitment of Mal, Myd88 and IRAK4&2 to form the Myddosome. Unstimulated TLR4 remains monomeric on the cell surface.

## 3.2 Sonicated *amyloid-β* fibril triggered TLR4 Myddosome

As mentioned in the introduction, preclinical and clinical studies have shown that the activation of the innate immune system could be involved in the pathologies of neurodegenerative diseases. In Alzheimer's disease for instance, both small soluble protein aggregates assembled from Aβ (oligomers) and larger fibrillary aggregates are able to bind to TLR4 and other receptors on microglia[105], the resident macrophage within the brain, to activate the immune system and trigger downstream inflammation responses. Therefore, to study the contribution of the innate immune response to inflammation, and test the role of the Myddosome played in neurodegenerative diseases, sonicated Aβ fibrils were locally deposited onto the surface of macrophage with GFP-tagged MyD88 (Figure 3.4) using ldSPIM.

To begin with, the sonicated Aβ fibrils used in our experiments were characterized by single molecule pull down (SimPull), which is a pull down assay that is able to selectively isolate and visualize cellular proteins at the single molecule level. This technique can be combined with dSTORM microscopy in order to super-resolve proteins at the surface, and quantify three parameters: area, perimeter and circularity (Figure 3.5 and 3.6). The area histogram in Figure 3.6 shows that approximately 90% of oligomers had areas below 0.025 $\mu m^2$. This correlates well with the aggregate sizes obtained by previous work in the group using the same protocol[106], who measured an average aggregate area of approximately 0.02 $\mu m^2$. Compared with LPS, which is a small molecule, sonicated *A*β fibrils are macromolecules, so it is important to ensure that the nanopipette is capable of delivering the fibrils smoothly without blockage. To test the macromolecule delivery ability of the nanopipette, the sonicated Aβ fibrils (4 $\mu$M monomer concentration) were first tagged with a 1:1000 dilution of Amytracker 680 (Ebba Biotech), a small molecule dye which specifically binds to amyloid fibrils or proto-fibrils; this was then delivered to the macrophage surface. Figure **3.**3.7 and Figure 3.8 shows the deposition of Amytracker tagged fibrils at the cell membrane (non-uniform distribution on the cell surface, as the nanopipette delivers from the left-hand side of the FOV), from which we can be confident that the nanopipette, with its current pore diameter, is able to reliably deliver large aggregates to the cell membrane.

Similar to the response triggered by LPS, macrophages were also activated by sonicated *A*β fibrils to form Myddosomes (Figure 3.9). A typical result showed that 450s post sonicated *A*β

fibrils triggering, the first Myddosome was formed and continuously assembled for the next 1000s. Compared with Myddosomes triggered by LPS, Myddosomes triggered by sonicated $A\beta$ fibrils formed and disassembled at a slower speed, but exhibit a longer lifetime.
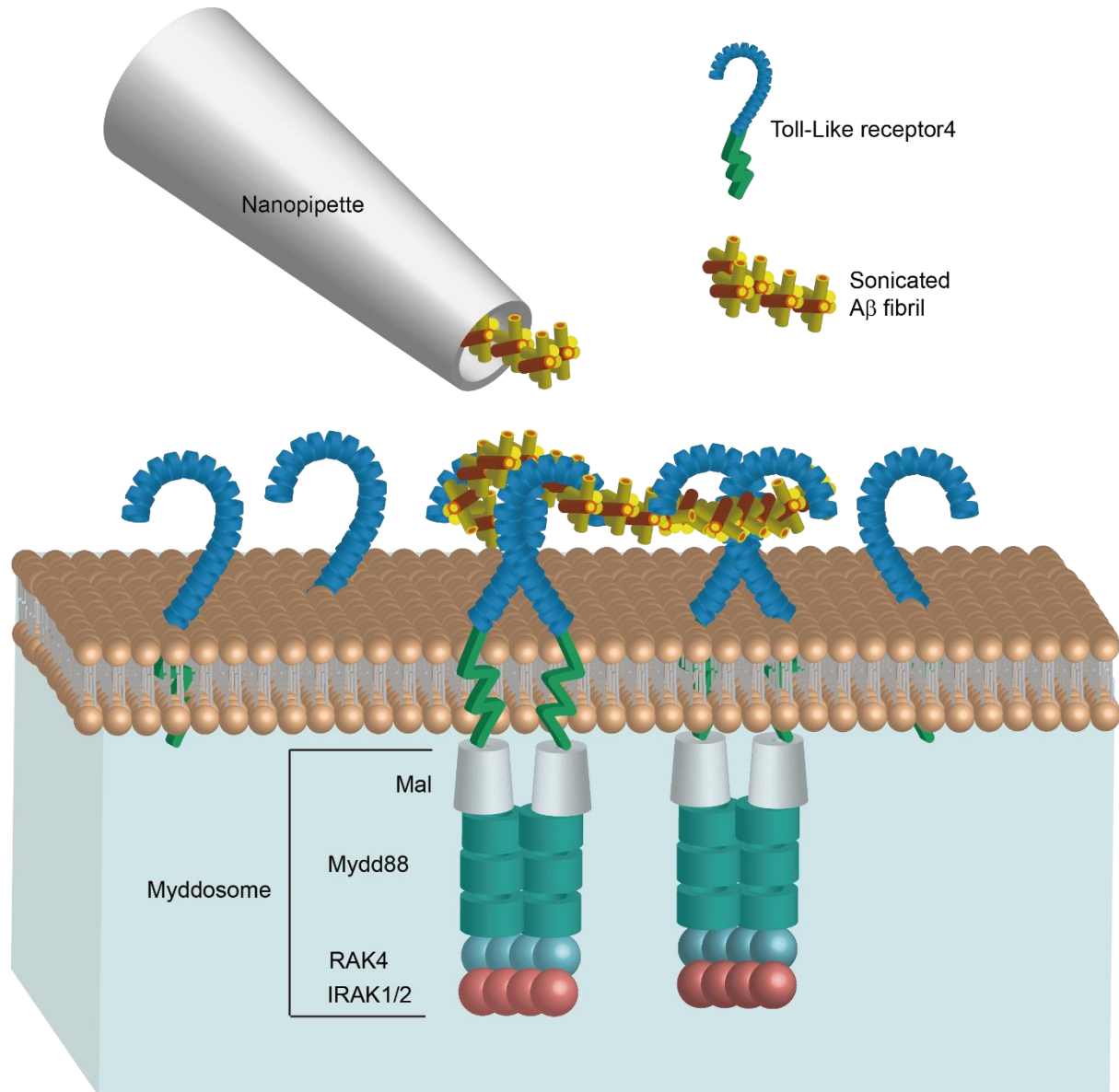


**Figure 3.4.** Schematic of Nanopipette delivered $A\beta$ fibrils triggered TLR4 Myddosome formation. The *amyloid-*$\beta$ fibrils is delivered by nanopipette to the macrophage surface. When $A\beta$ fibrils interact with TLR4, it will trigger the dimerization of TLR4, which will active the recruitment of Mal, Myd88 and IRAK4&2 to form the Myddosome. While those unstimulated TLR4 remains monomer on the cell surface.
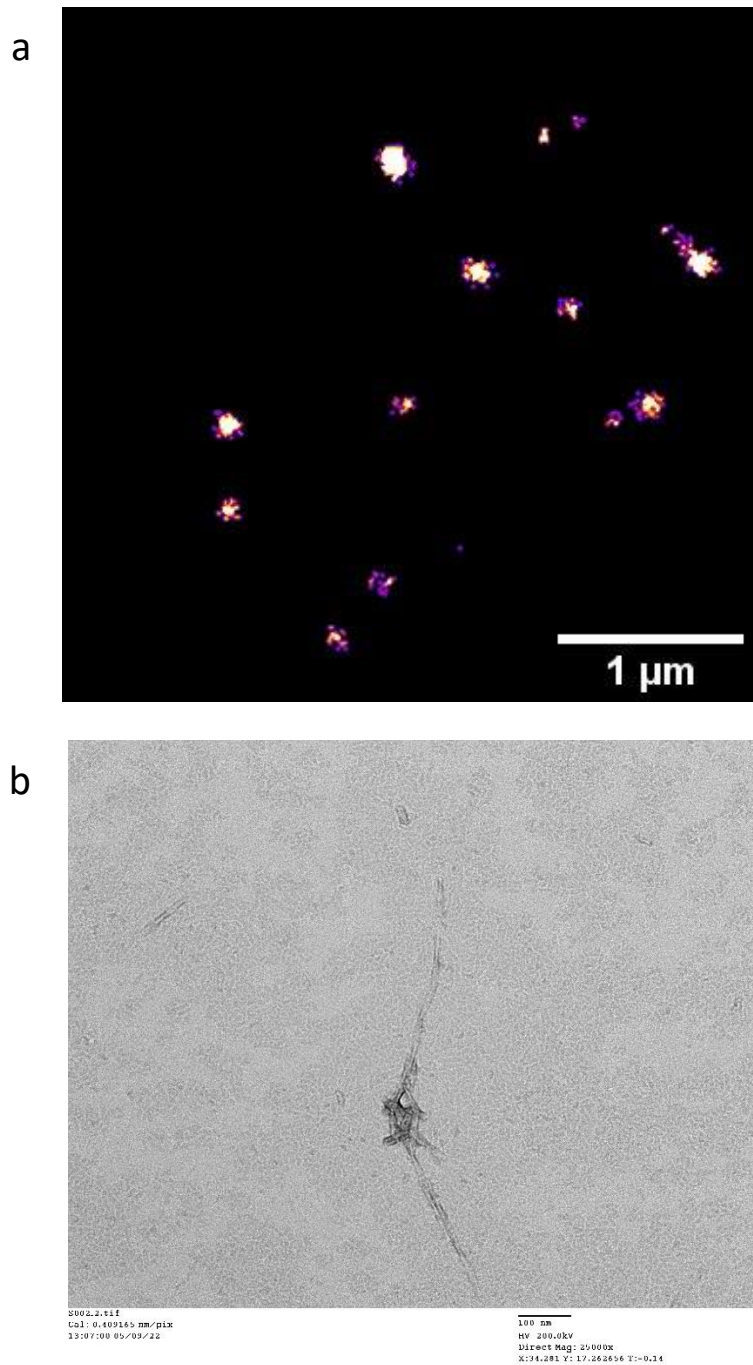
**Figure 3.5**. a) The super-resolved image of sonicated Aβ42 fibrils using SimPull. Scale bar is 1 μm and the resolution of dSTORM is around 15-30 nm. b) The EM image of sonicated Aβ42 fibrils. Scale bar is 100 nm.
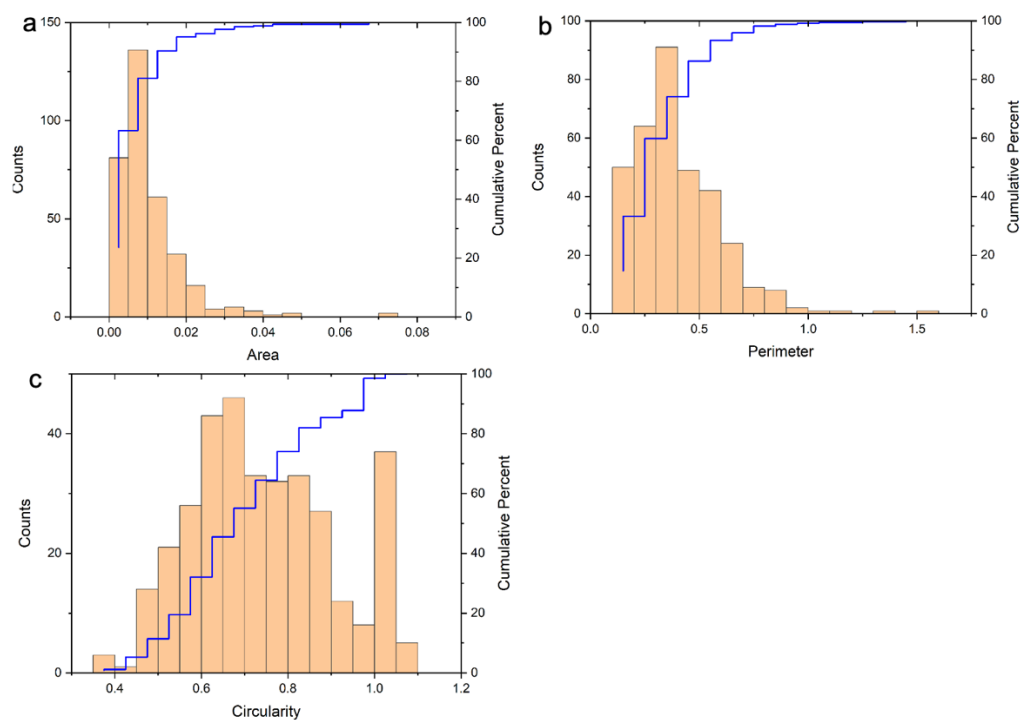
**Figure 3.6.** The characterization of sonicated Aβ42 fibrils. a) is the area, b) is the perimeter and c) is circularity.
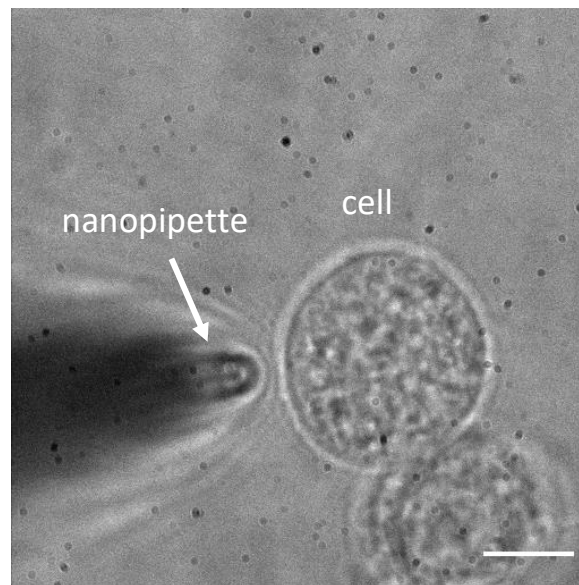
**Figure 1.7.** Nanopipette with large tip diameter approaches the cell with an angle to delivery sonicated Aβ fibrils. Scale bar is 8.5 μm.
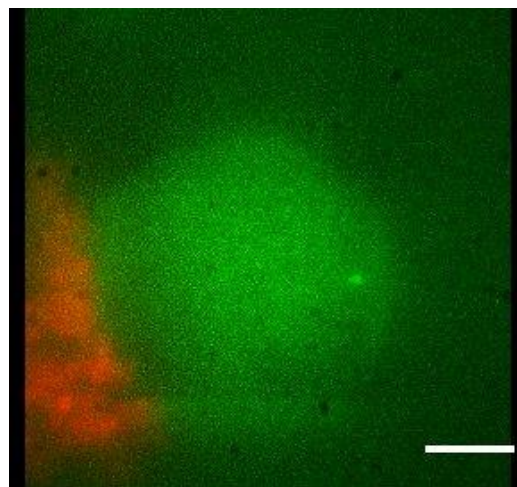


**Figure 3.8.** Projected view of tagged sonicated Aβ fibrils (red) after delivery to the cell membrane (green). Scale bar is 5 μm.
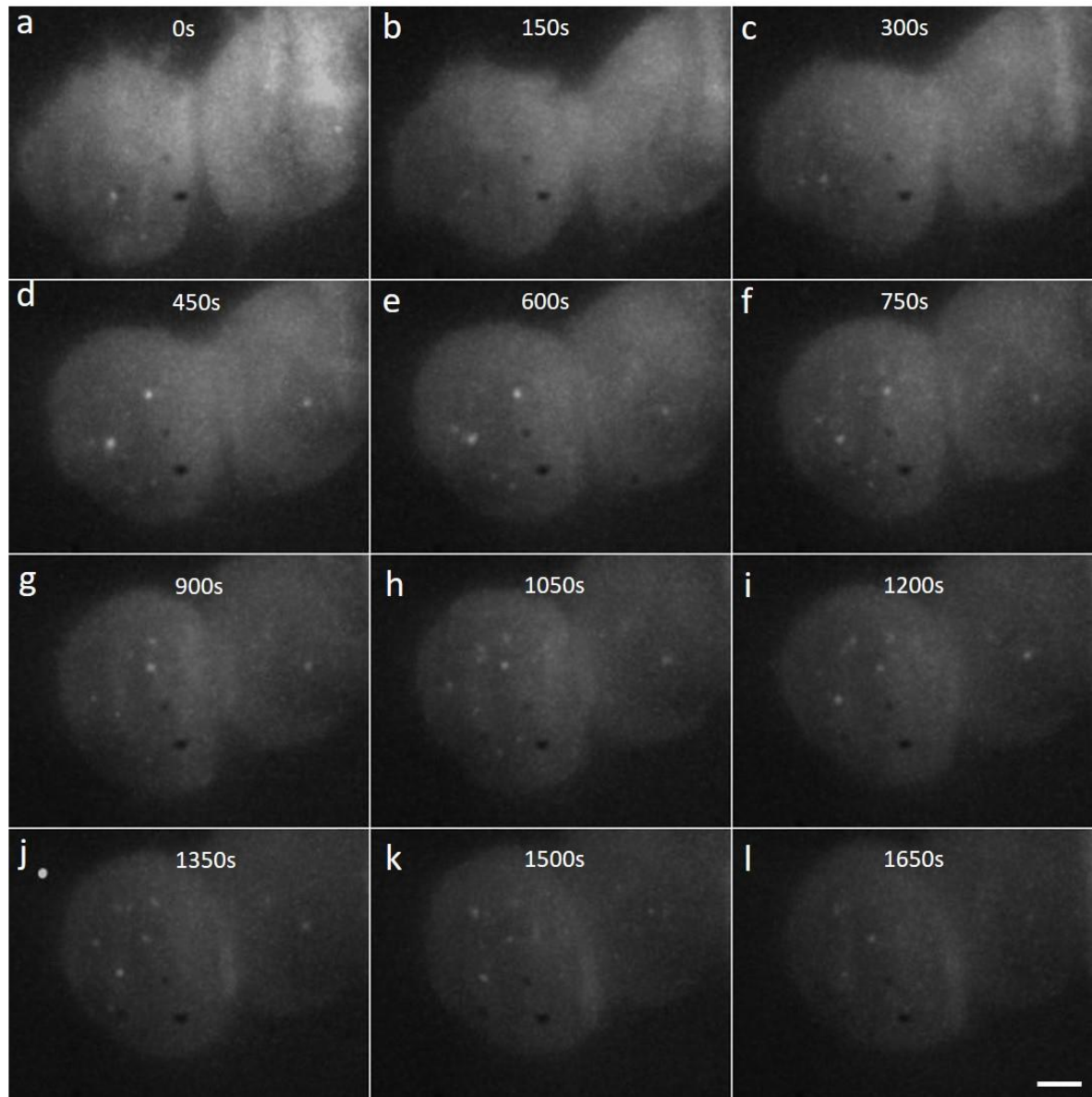
**Figure 3.9.** Light sheet 3D scan projection of Myddosome formation triggered by the delivery of sonicated *A*β fibrils. The Myddosome formation stared at 450s post triggering and last for the following 1000s. At 900s post triggering, the disassembly of Myddosome happened. The scale bar is 2 μm.

## 3.3 Light sheet live 3D imaging of Myddosome formation

Previous imaging studies on Myddosomes commonly involve the use of TIRF and confocal microscopy. However, both of these have limitations in visualising Myddosome formation.

TIRF is a 2D real time imaging method, which can only image the area 200nm above the coverslip. When imaged by TIRF, only the Myddosomes formed on the bottom surface of triggered macrophages can be visualized, with the Myddosome assembled above the bottom surface not able to be observed. This can introduce several errors in Myddosome kinetics analysis. First, it is unable to measure the total number of formed Myddosomes within a certain time period post triggering. Second, it is hard to calculate the lifetime of assembled Myddosomes, because when the fluorescence of a Myddosome disappears from the FOV, it is impossible to determine if the Myddosome is disassembling, or if it is moving from the bottom surface to an upper position. Confocal microscopy is able to image the cells in 3D; however, due to its low scanning speed for image acquisition confocal microscopy is not capable for live cell volumetric imaging over time.

Light sheet 3D scanning can address these issues significantly. Either by scanning the objective or sample stage, light sheet microscopy is able to scan the whole cell sample at a relatively high speed (single cell scanning only takes 2s). In the reconstructed 3D scan image, Myddosomes formed everywhere in the total cell volume can be observed (figure 3.10 b). The spatial distribution and movement of each individual Myddosome is tracked and shown in 3D volume rendered images (figure 3.10 e-g). Compared with TIRF, 3D light sheet imaging is able to follow all  Myddosomes formed, allowing for the calculation of the lifetime of each individual Myddosome, and the total number of Myddosome assembled within a certain time period post triggering precisely. The 3D light sheet scan also provides us with a solid foundation to analyse and compare the kinetics of Myddosomes formation after stimulation with different types of triggering molecules.
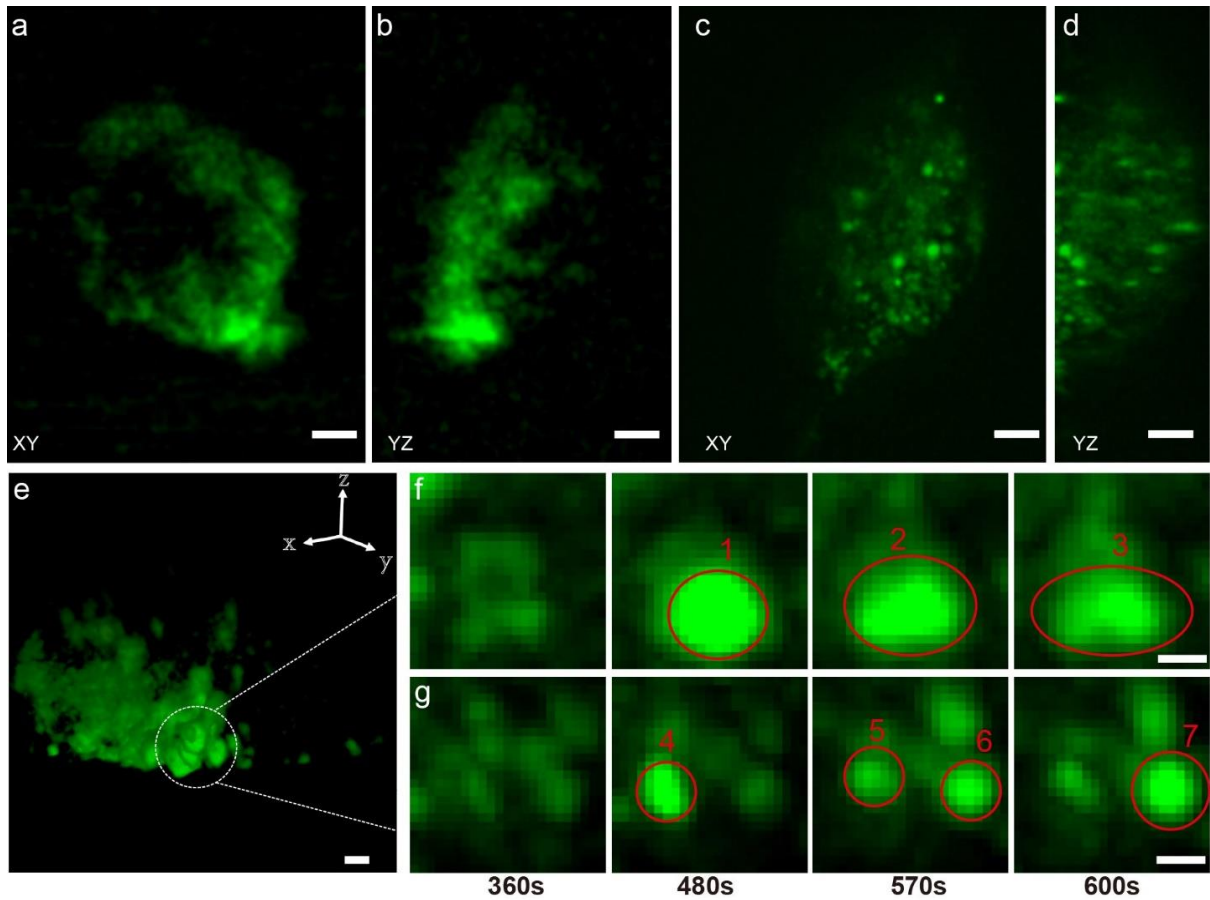
**Figure 3.10**. Representative images of whole-cell 3D imaging of Myddosome formation in live macrophages (n=10). **(a) and (b)** The intensity projection of $A\beta$ monomer control in XY and YZ at t=300 s. **(c) and (d)** The intensity projection of Myddosome formed in macrophage triggered by sonicated $A\beta$ fibrils in XY and YZ at t=300 s. The scale bar is 4μm. **(e)** The 3D volume rendering of the data in **(c)** showing the spatial distribution of Myddosomes. The scale bar is 4 μm. Time course of selected Myddosomes in **(e) (marked by the white dish circle)** response to sonicated $A\beta$ triggering are shown in **(f)** and **(g). (f)** The process of Myddosome formation and splitting is labelled in red circle 1 to 3. **(g)** The process of Myddosome assembly and disassembly is labelled in red circle 4 to 7. 480 s post $A\beta$ fibrils activation, Myddosome with different sizes formed. Then at 570s post triggering, the big Myddosome (in **(f)**) started splitting while the small one (in **(g)**) began to disassemble. At 600 s post triggering, the big Myddosome was still splitting and the small one had disassembled. The scale bar is 2 μm.

**3.4 Kinetics of Myddosome assembly**

Previous studies have demonstrated that when TLR4 is triggered by various kinds of stimulus, the response speed and intensity are different. In this section, in order to interpret the relation between the agonists and signalling efficiency, the kinetics of Myddosomes which are triggered by LPS and sonicated Aβ fibrils are analysed and compared by measuring 5 parameters: 1) the first time point when Myddosome formed, 2) the Myddosome lifetime, 3) the total number of oligomers formed within 30mins upon triggering, 4) the Myddosome size and 5) the variation of MyD88 oligomer size with stimulation time.

**3.4.1 The time point when first Myddosome formed**

Firstly, the time point when the first Myddosome formed was measured. This parameter represents the speed that macrophages respond to TLR4 dependent triggering. In our experiment, for the controls, PBS and Aβ monomers are delivered to macrophages (figure 3.11 a). Then LPS and sonicated Aβ fibrils were delivered to macrophages and imaged by 3D light sheet scan. From the 3D projection image of the Myddosome formation (Figure 3.11), the PBS and Aβ monomer control did not form Myddosomes. In contrast, the LPS-triggered Myddosomes started forming within 5mins after local delivery and the time point when the Aβ-triggered Myddosomes formed is around 10mins later, beginning at 15min after delivery. In total, we have imaged 7 replicates, comprising a total of 73 cells (sonicated Aβ fibrils triggered 34 cells and LPS triggered 39 cells). The dataset of each replicate are presented in a box chart (Figure 3.12). From the results, the Myddosomes formed after triggering by sonicated Aβ fibrils first appeared after a longer time, ranging from 200s to 1000s. In contrast, after LPS stimulation, macrophages only need less than 200s to assemble the first Myddosome. Looking at the total dataset summarized from each replicate, on average the LPS-triggered Myddosome first formed at 100s after delivery and the Aβ-triggered Myddosome first formed at 400s after delivery. This difference demonstrates that at the beginning of TLR4 triggering, the stimulation of LPS is more intensive than sonicated Aβ fibrils, resulting in a significantly faster Myddosome assembly speed (p< 0.0001).
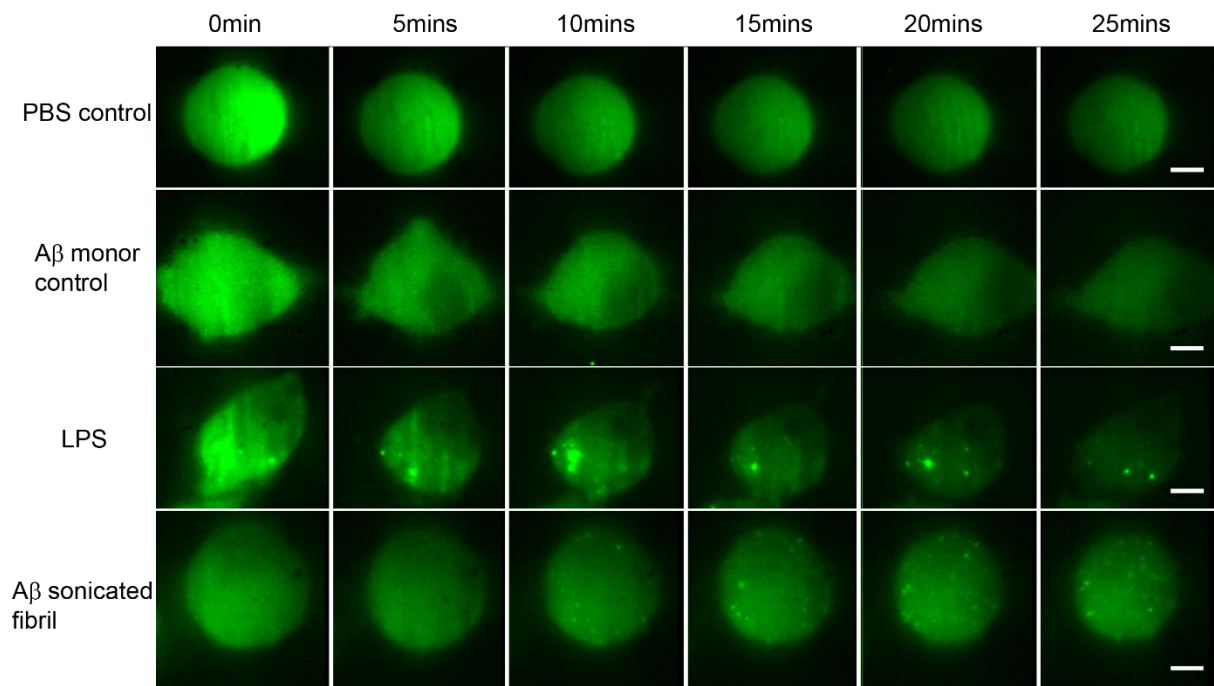
**Figure 3.11.** A montage showing the time series of Myddosome assembly. a) The PBS control showing no Myddosome formed when PBS buffer is delivered to TLR4. b) The Aβ monomer control also showing no Myddosome formed. c) The Myddosome formation triggered by LPS, showing that the first Myddosome assembled within 5mins after delivery. d) The Myddosome formation triggered by sonicated Aβ fibrils with the first one assembled at around 15mins after delivery. The scale bar is 5 μm.
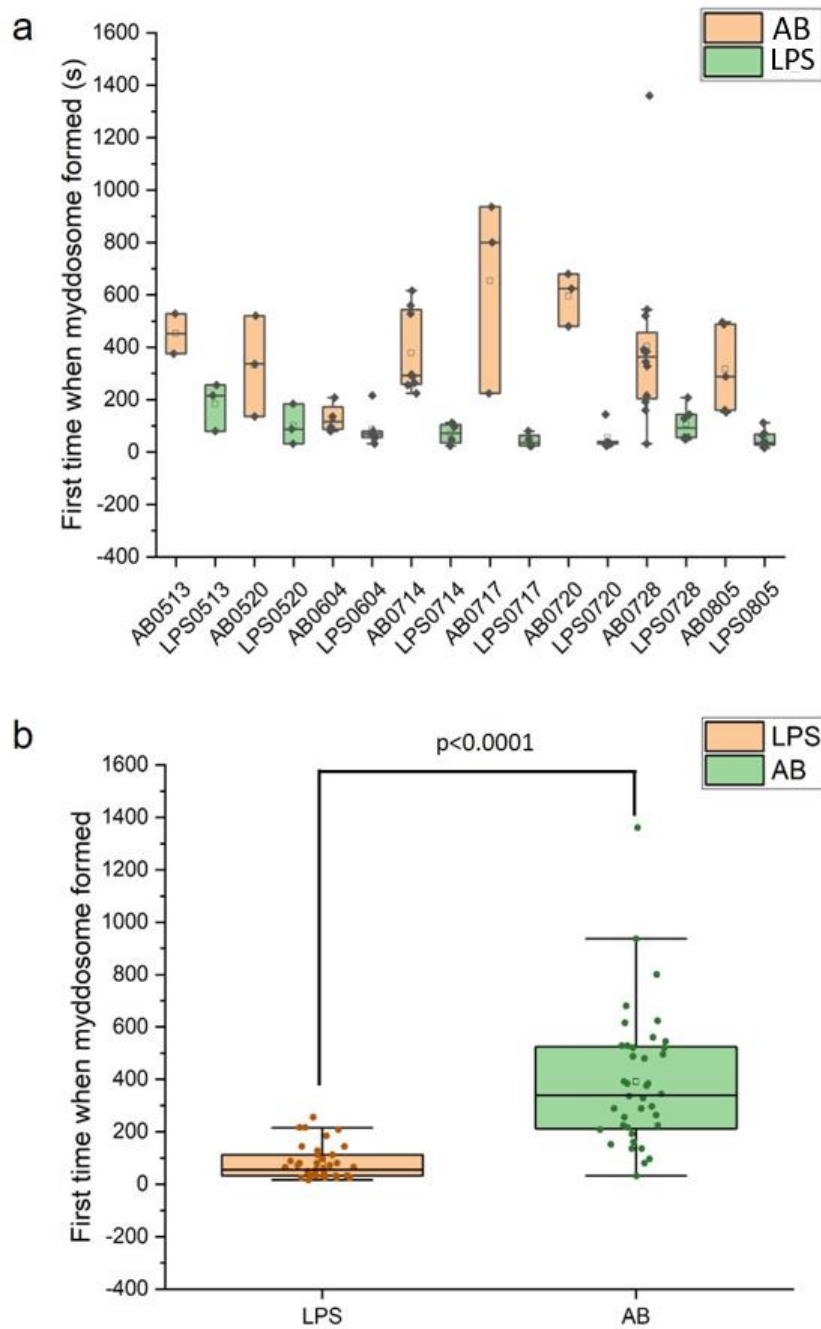
**Figure 3.12.** Time taken (seconds) for the newly formed Myddosome to be visible after local delivery. a) is the time points analysed in every replicate and b) is the total data set over the 8 replicates. Each point refers to one cell in each condition. Each FOV was normalised Box plots illustrate maximum/minimum, interquartile range, median and mean (square box) values. Unpaired t-test was made and the p value < 0.0001

## 3.4.2 Lifetime of Myddosome

The lifetime of Myddosome is proposed to be a factor to characterize its signalling kinetics. According to the previous study[107], the lifetime of Myddosome is related to the signalling intensity. In general, the Myddsomes with longer lifetimes are associated with a strong or continuous stimulation of TLR4, which leads to the generation of strong downstream cellular reactions. While Myddosomes with short lifetimes lead to less intensive TLR4 triggering.

To calculate the lifetime accurately, it is important to ensure that the GFP fluorescence signal of MyD88 puncta will not bleach during the 3D scanning. Macrophages with LPS-triggered Myddosomes were first fixed and imaged with the same laser power and same scanning time to ensure the Myddosomes will not be bleached during 3D imaging. It was tested that within 30mins of scanning the fluorescence of the Myddosomes decreased, but did not totally beach, indicating that the signal is due to disassembly rather than photobleaching.

An automatic particle tracking algorithm is used to obtain the trajectories of each individual Myddosome and analyse the lifetime. The lifetime of Myddosomes in individual replicates is present in a histogram (Figure 3.13). The lifetime of both LPS and sonicated Aβ fibrils triggered Myddosomes have a large population below 250s. One reason to explain the high population of Myddosomes with short lifetimes is that during Myddosome signalling, MyD88 will also assemble into dimers or tetramers, oligomers smaller than the 6-8 Myddosomes observed in the canonical crystal structure. The fluorescence signal of MyD88 dimers and tetramers will be detected and tracked by the algorithm and contribute to the short lifetime puncta population. In the long lifetime area (lifetime longer than 1000s), the Aβ-triggered Myddosomes have a larger population than LPS triggered ones, suggesting that Aβ-triggered Myddosomes have longer lifetime. In figure 3.14, the total dataset also showed a small, but significant increase in the average lifetime of Myddosomes formed after sonicated Aβ fibrils stimulation ($p < 0.001$, $n > 2000$, unpaired two-sided T-test).

From the lifetime results we can make a hypothesis that it is the structural property of LPS and sonicated Aβ fibrils that causes the significant lifetime difference. LPS is a small molecule; when delivered to the macrophage surface, it will bind to TLR4 rapidly and trigger TLR4 dimerization. The nanopipette delivered LPS is a pulse based process. After the delivery is finished, there will not be any further supply of LPS in the media. Therefore, the LPS

stimulation is a strong but instant. Sonicated Aβ fibrils, are macro-protein filaments. When sonicated Aβ fibrils are deposited on a macrophage surface, they can occupy more space and stay for a longer time, resulting in a continuous stimulation of TLR4.
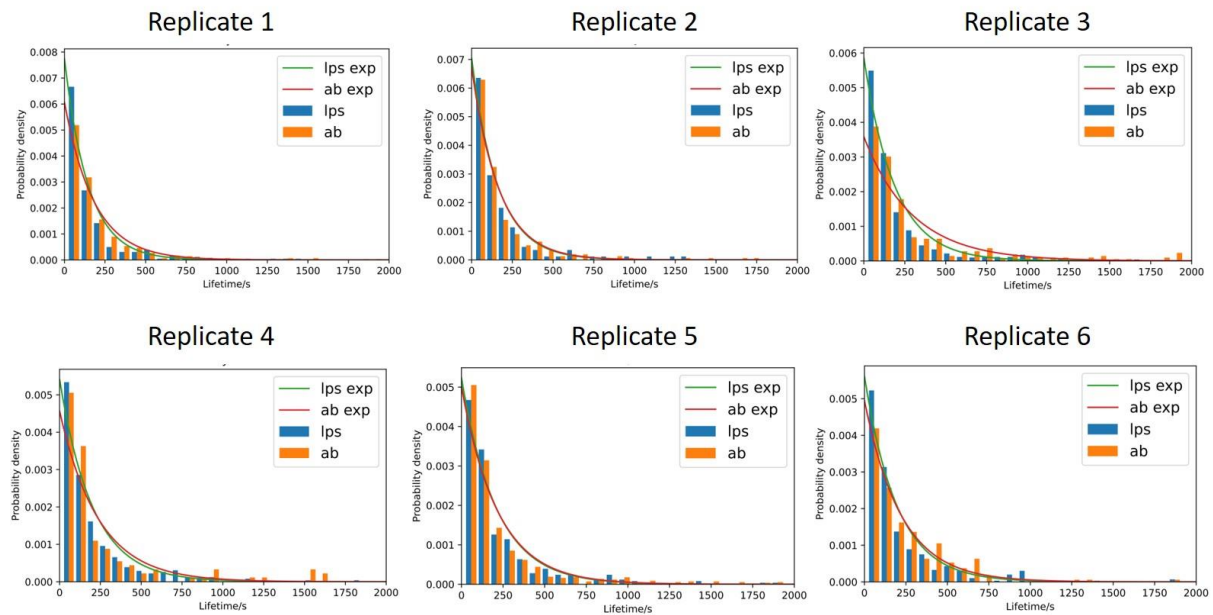


**Figure 3.13.** Histogram of Myddosome lifetime calculated in six replicates. Both LPS and sonicated Aβ fibrils triggered Myddosomes have a large population in the short lifetime area. In the long lifetime part, the population of sonicated Aβ fibrils triggered Myddosomes is larger than LPS triggered ones. The data is fitted to an exponential using the equation $y=Ae^{-\lambda x}$. The fitting parameters for each replicates are listed. Replicate 1, A values for LPS and Aβ are 0.00774 and 0.00606, lambda values are 0.0676 and 0.00544. Replicate2, A values for LPS and Aβ are 0.00704 and 0.00672, lambda values are 0.00622 and 0.00597. Replicate3, A values for LPS and Aβ are 0.00586 and 0.00358, lambda values are 0.00528 and 0.00335. Replicate4, A values for LPS and Aβ are 0.00541 and 0.00456, lambda values are 0.00491 and 0.00420. Replicate5, A values for LPS and Aβ are 0.00523 and 0.0050, lambda values are 0.00475 and 0.00457. Replicate6, A values for LPS and Aβ are 0.00562 and 0.00495, lambda values are 0.00507 and 0.00452.
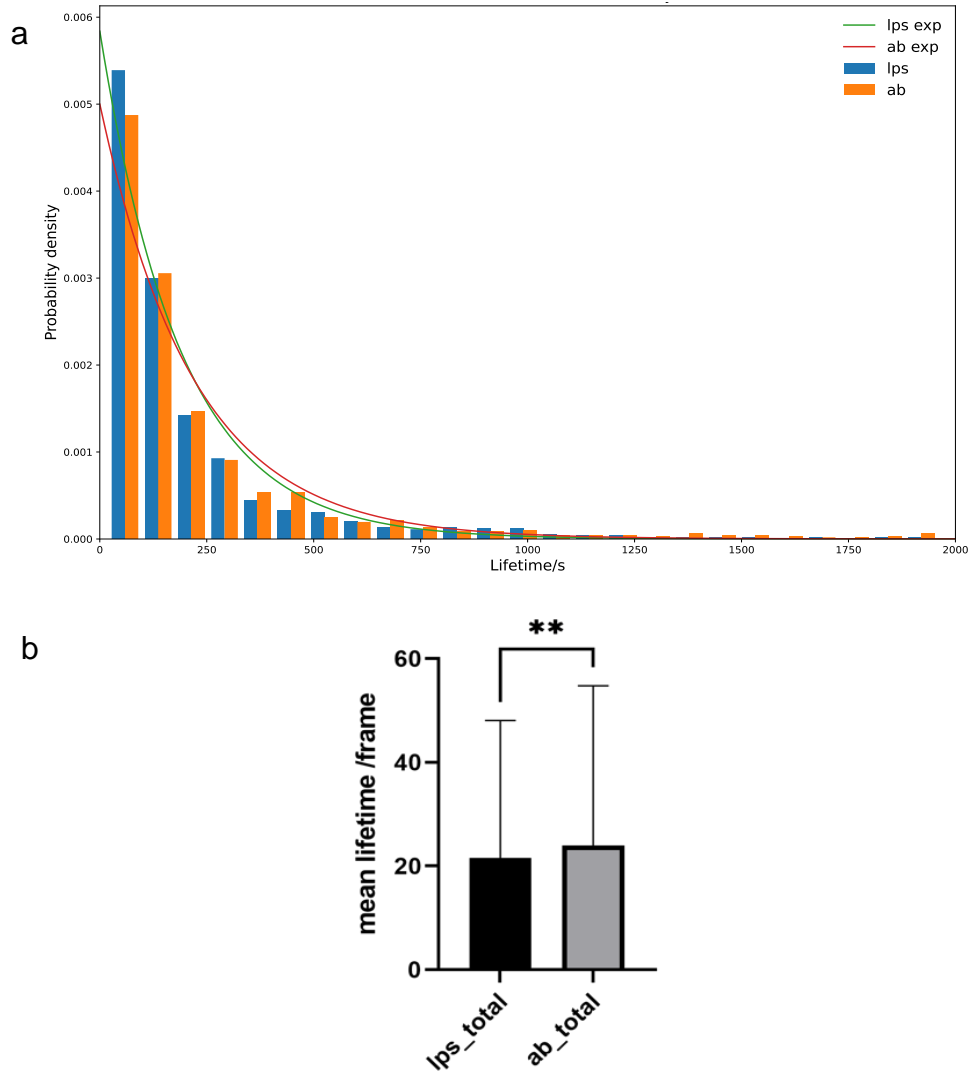
**Figure 3.14.** a) Distribution of lifetimes measured for all MyD88 puncta after LPS and sonicated Aβ fibrils stimulation. Lifetime distribution is fitted to an exponential function. b) Difference in the mean lifetime is significant (unpaired t test, p value < 0.05) due to large sample number (n = 2233 for lps, n = 2041 for sonicated Aβ fibrils, where n is the total number of Myddosomes tracked for all cells in each condition). 1 frame = 10 seconds. Error bar shows 1.5× interquartile range for each condition. The data is exponential fitted using the equation $y=Ae^{-\lambda x}$. The fitting values for LPS and Aβ are 0.00584 and 0.00500 in terms of A and 0.00526 and 0.00456 in terms of lamda.

### 3.4.3 Myddosome size.

Another important parameter to characterize the Myddosome signalling is Myddosome size. When using TIRF or light sheet microscopy, the acquired image of MyD88 puncta is diffraction limited. According to the structural study, the actual size of the Myddosome should be less than 1 μm, which is below the resolution of the diffraction limited imaging method. Therefore, it is impossible to measure the real size of the Myddosome using diffraction limited TIRF or light sheet microscopy. Methods such as measuring the fluorescence intensity of Myddosomes as an indicator to estimate the size have been put forward before. However, due to the photobleaching of GFP, the Myddosome fluorescence intensity in two separate time points is different, resulting in inaccurate measurement.

In order to address this issue, we use direct stochastic optical reconstruction microscopy (dSTORM),which is the most commonly used super-resolution imaging technology, to visualise and quantify the real size of LPS and sonicated amyloid-β aggregates triggered Myddosomes. The MyD88-GFP could not be super-resolved directly due to the rapid photobleaching. As a result, an Alexa Fluor$^{TM}$ 647 conjugated anti-GFP antibody was used to label MyD88-GFP in order to acquire more fluorescence signal for super resolution reconstruction. The reconstructed dSTORM images are presented in Figure 3.15. The green channel is the MyD88-GFP original signal, and the red channel is the reconstructed dSTORM image. The merged channel overlaps the green and red image showing the colocalization of MyD88-GFP and the super-resolved size of the Myddosome. From Figure 3.15, the control cells (MyD888-GFP without stimulation) showed no formation of Myddosome in the green channel and no signal overlap in the merged channel. The LPS and Aβ-triggered cells showed the Myddosomes formed in the green channel and had good overlap in the merged channel. The co-localisation information was helpful in identifying the real Myddosomes (spots showing yellow colour in merged channel) from unspecific signal in the super resolution reconstruction (The small spots in red channel without overlapping with GFP signal in merged channel).

The size of Myddosome formed with 30mins after LPS and sonicated Aβ fibrils stimulation are listed in Figure 3.16. In each replicate, the average size of Myddosome triggered by LPS is around 200nm while the average size of Myddosome triggered by sonicated Aβ fibrils is around 300nm (Figure 3.16 (a)). Looking at the total dataset, the trend is also the same, with

the Aβ-triggered Myddosomes having a significantly larger size compared to the LPS triggered Myddosomes (Figure 3.16(b)).



.
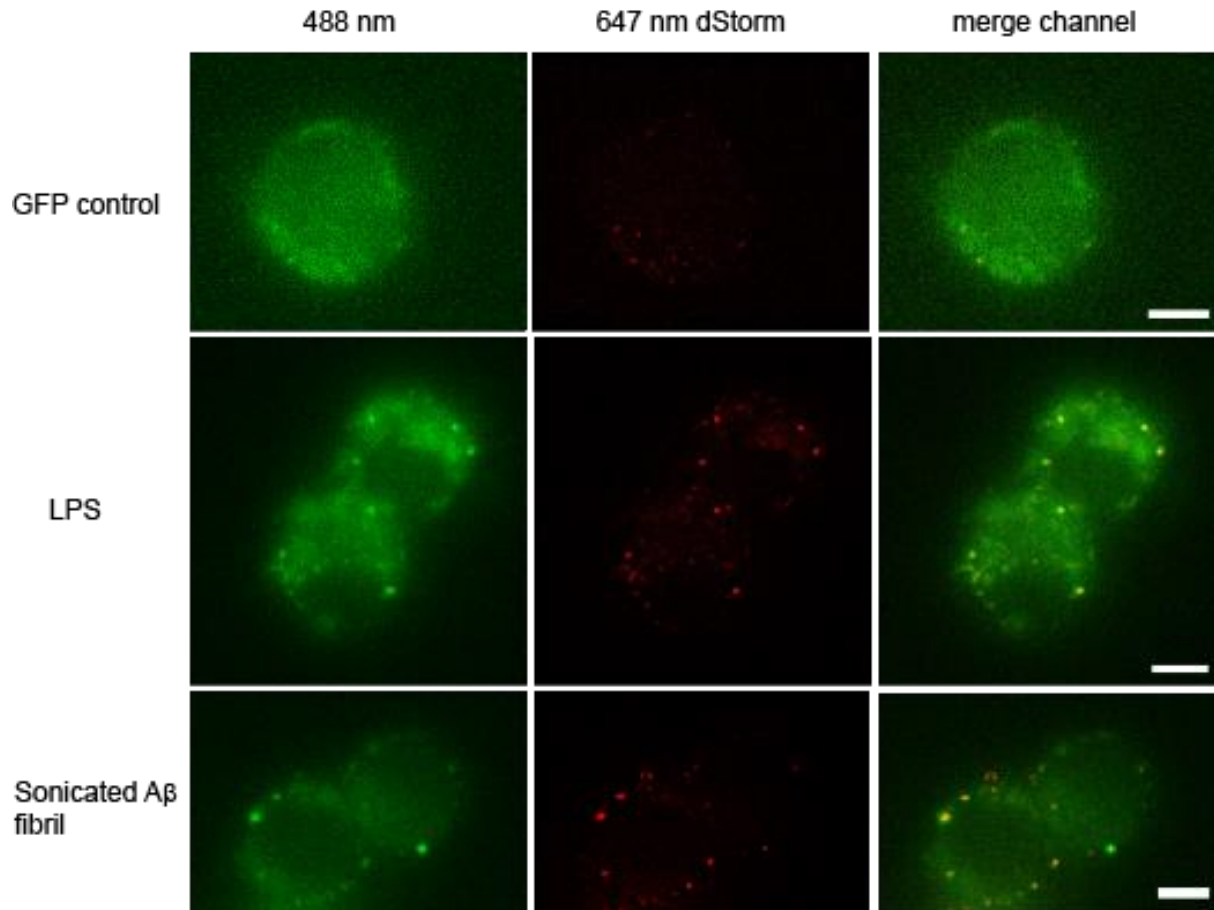
**Figure 3.15.** Fixed macrophages stimulated by PBS (control), LPS and s sonicated Aβ fibrils. 488nm channel shows the MyD88-GFP signal. 635nm channel shows the reconstructed super-resolved image of Alexa-647 conjugated anti-GFP antibody to represent the size of Myddosome. The merged channel shows signal overlap between the Myddosomes and Alexa-647 conjugated anti-GFP antibody. Only co-localized puncta (in yellow colour) are the real Myddosome signal, the others are unspecific binding of antibody. The scale bar is 5 μm.
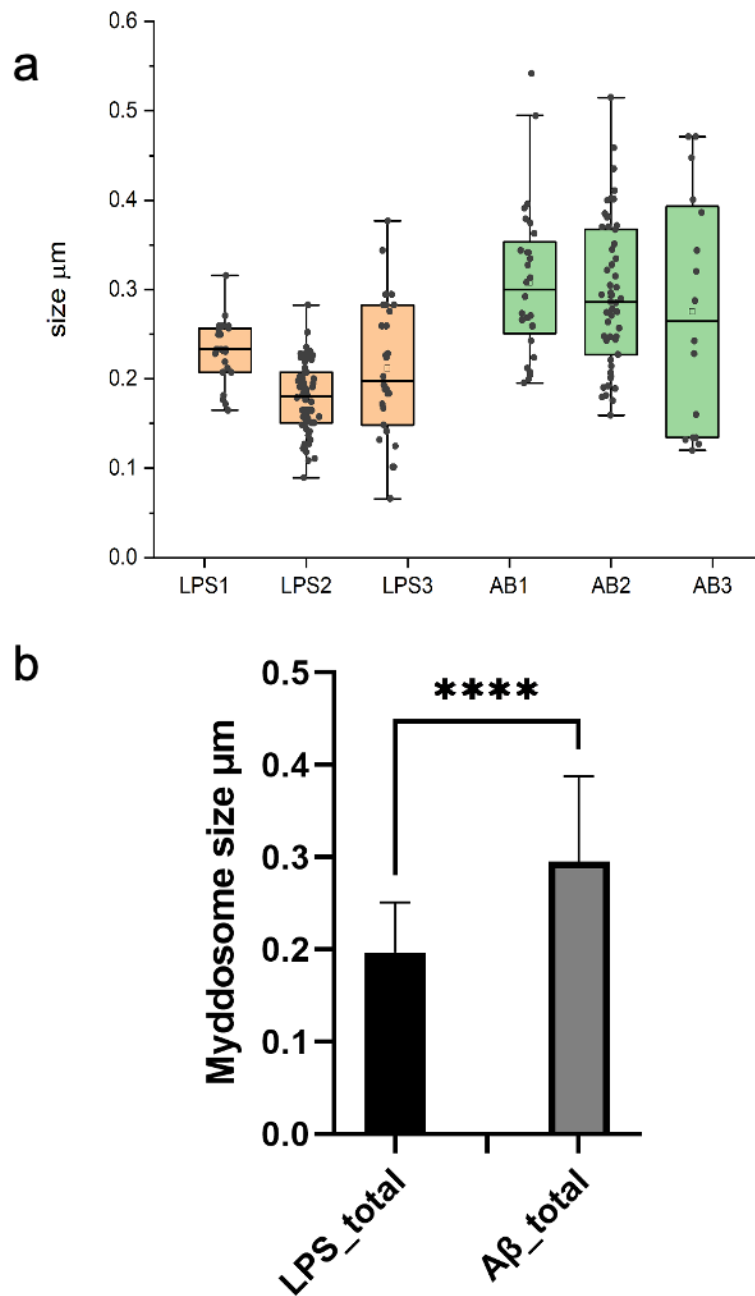
**Figure 3.16.** The size of Myddosomes triggered by LPS and sonicated Aβ fibrils. a) The size difference between LPS and sonicated amyloid-β aggregates in three replicates. In each replicates the Myddosome size, triggered by sonicated Aβ fibrils, is larger than LPS triggered ones. b) The total datasets of three replicates. Within 30mins post stimulation, the average size of LPS triggered Myddosome is around 200nm while the value of sonicated Aβ fibrils triggered Myddosmes is near 300nm (unpaired t test, p value < 0.0001).

### 3.4.4 Myddosome size change with different stimulation period

Beyond the Myddosome size within 30mins stimulation of LPS and Aβ, MyD88 -/- MyD88-GFP macrophages were stimulated and fixed at another 4 time points post triggering: 3 hours, 6 hours, 12 hours and 24 hours to characterize the size changes with stimulation period.

The size of Myddosomes assembled in different time points after triggering is listed in Figure 3.17. Each box chart represents one individual replicate. For most of the time points in all three replicates, sonicated Aβ fibrils stimulation led to larger Myddosome assembly than LPS.

From Figure 3.17 it can be observed that there is an increasing trend for the change in Myddosome size with time for both LPS and sonicated Aβ fibrils triggered Myddosomes (in some timepoints the error bar is large, this is because at longer timepoints the number of survived cells is limited, especially after 12 hours). The average size of Myddosomes summarized from all three replicates are plot with time in Figure 3.18. It is clear that the average size of Myddosomes increases as stimulation time progressed. Since the LPS and sonicated Aβ fibrils were added into the cell medium, they will keep stimulating the cells with time. The longer macrophages were stimulated, the more intensive triggering will be generated, resulting in the larger size Myddosome assembly.

The size distribution of Myddosomes assembled at each timepoint is shown in Figure 3.19. It can be observed that in each timepoint there is a large population of Myddosomes whose size is less than 400nm. When the stimulation time is longer than 3 hours, more Myddosomes with size larger than 400nm start appearing. It is easier to present this change in Kernel Density Estimate plots (figure 3.20). In both the sonicated Aβ fibrils and LPS conditions, the peak positions of fitted Myddosome size distribution at different time points were located between 100nm to 400nm and did not have a clear trend to move toward large sizes. However, there was a clear trend in the skewness of the fitted distribution curve to larger sizes as time progressed, suggesting that whilst the Myddosomes with a similar size between 100nm to 400nm at all time points remains the majority, there was a small but increasing population of larger Myddosome forming as time progressed. This size changes could be explained by either the assembly of Myddosomes with higher MyD88 stoichiometries or higher level of TLR4 assembly in response to the stimulus that initializes Myddosome signalling.
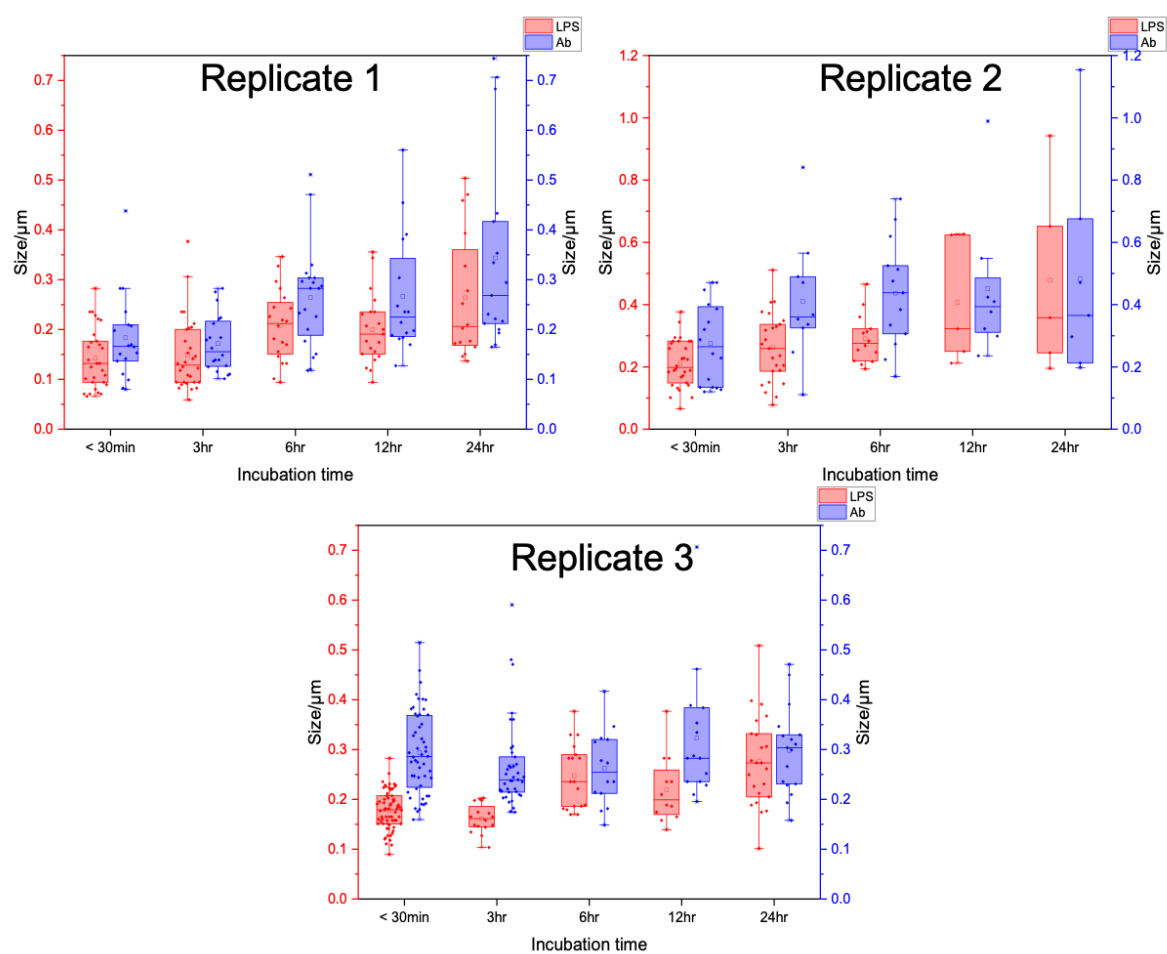
**Figure 3.17.** Myddosomes size changed with stimulation time for both LPS and sonicated Aβ fibrils. In most tie point the size of sonicated Aβ fibrils triggered Myddsome is larger than LPS triggered ones.
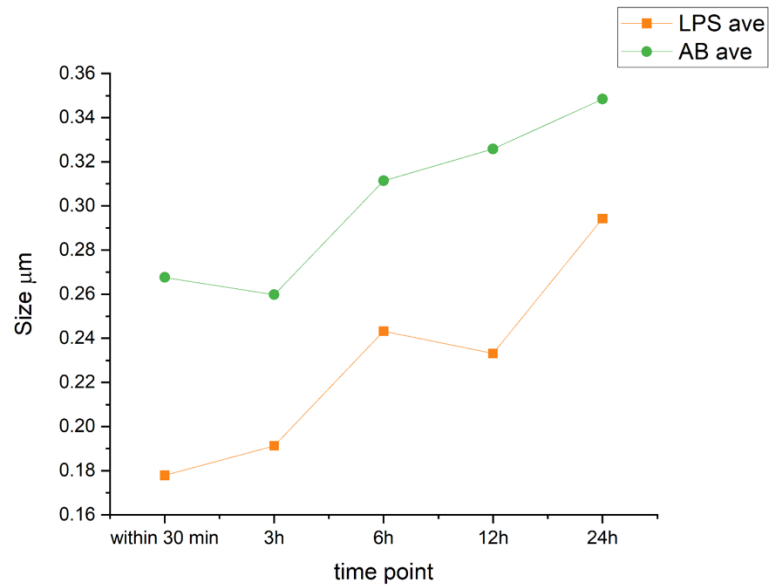
**Figure 3.18.** The average size of Myddosome assembled with different stimulation time for both LPS and sonicated Aβ fibrils summarized from three replicates. There is an increase in Myddosome size with stimulation time.
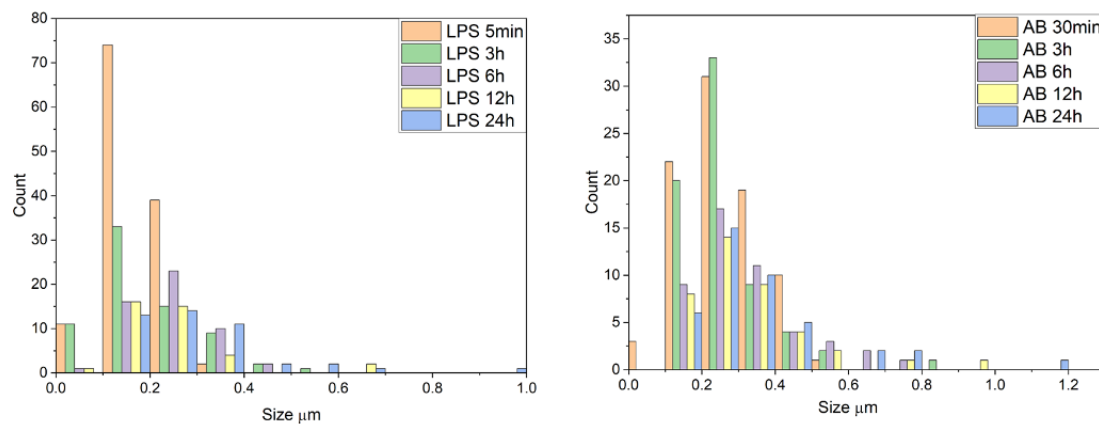


**Figure 3.19.** The size distribution of the Myddosomes formed at each timepoint shown as a histogram. For all timepoints the majority of Myddosomes are less than 400nm. With time, Myddosomes with larger than 400nm started appearing.
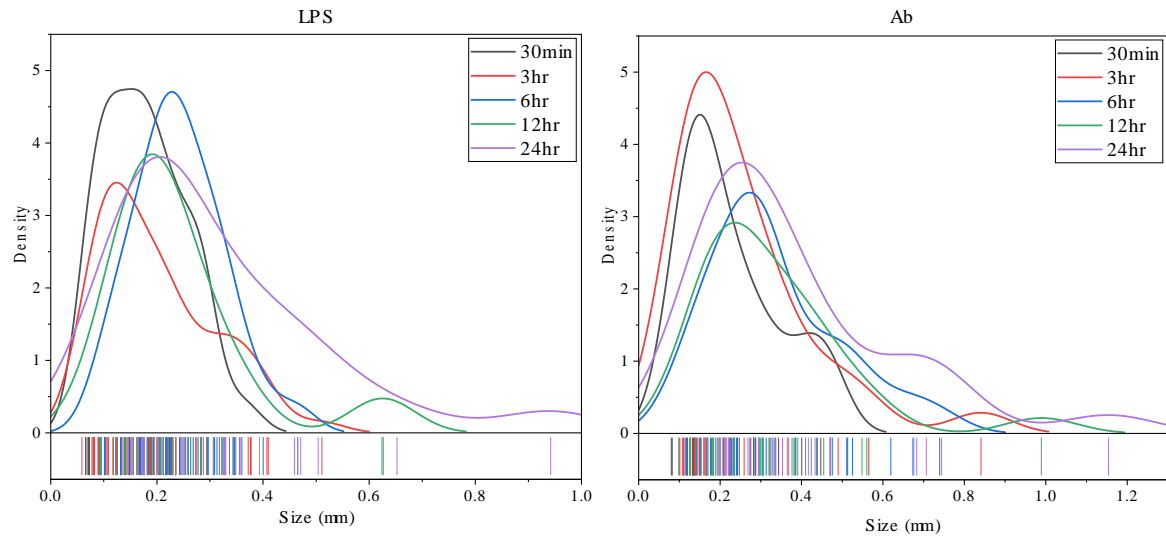
**Figure 3.20.** Kernel Density Estimate plots showing the size distribution of the Myddosomes at different time points. Skewing towards larger sizes appears with increasing stimulation time is observed.

### 3.4.5 Total number of Myddosome formed

The total number of Myddosomes is the final parameter to describe the kinetics of Myddosome formation. The automatic particle tracking algorithm was also used to find the number of tracked Myddosomes. The total number of Myddosomes assembled after stimulation summarized from 6 replicates is listed in Figure 3.21 (a). Although the total number of LPS-triggered Myddosomes is around 60 which is larger than sonicated Aβ fibrils, there is no significant difference between them (single tail unpaired T-test p >0.05). This may be caused by the low-level oligomers of Myd88 as described in section 3.4.2. Since these MyD88 oligomers existed in both conditions, the automatic particle tracking algorithm will take account of them in the total number of real Myddosomes, introducing errors in the comparison.

In order to filter out the contribution of these MyD88 oligomers, we set a lifetime threshold at 50 seconds according to the previous studies. Only the puncta with lifetime longer than 50 seconds will be counted in the total number of assembled Myddosomes. The filtered Myddosome number is listed in Figure 3.21(b). The number of LPS triggered longer lifetime Myydosome is significantly more than sonicated Aβ fibrils triggered ones. However, the ratio of the number of Myddosomes which last longer than 50s vs the total number did not show a difference between LPS and sonicated Aβ fibrils (figure 3.22).
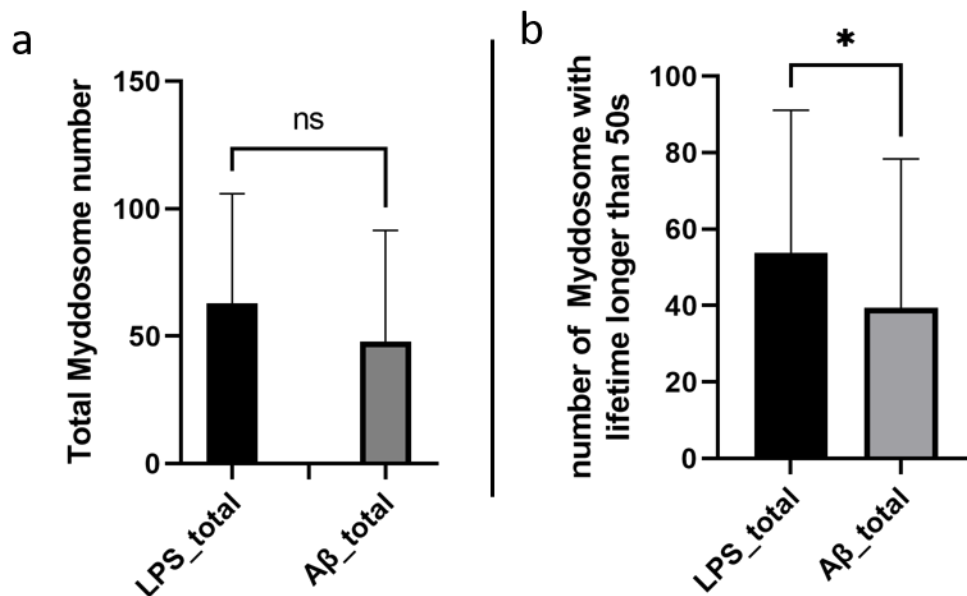
**Figure 3.21.** Total number of Myddosome formed under different conditions. a) The total number of all Myddosomes formed within 30mins after nanopipette delivery. The single tail unpaired T test shows no significant difference between LPS and sonicated Aβ fibrils stimulation. b) The filtered Myddosome number that only accounted for the Myddosomes with lifetime longer than 50 seconds. The same single tail unpaired T test shows there is a significant difference between two stimuluses (unpaired t test $p<0.05$).



**Figure 3.22.** The ratio of the number of Myddosomes which last longer than 50s vs the total number. Unpaired t test shows no significant difference.
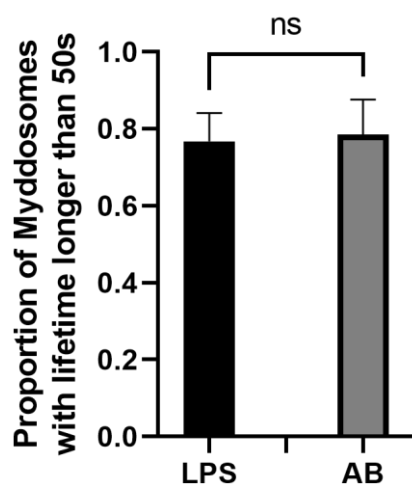
## 3.5 Materials & Methods

### 3.5.1 Lentiviral transfection and transduction for MyD88-GFP macrophage production

HEK cells (HEK293T) and immortalised macrophages were grown in complete medium: Sigma DMEM+ 10% FCS + 2mM L-glutamine + pen/strep NB. The medium was topped up with fresh L-glutamine every 4 weeks. The lentiviral transfection and transduction need an 8-days progress. Usually, we started at Monday and harvest the transduced cells at the next Tuesday.

Monday: the immortalised MyD88$^{-/-}$ macrophage cell line is seeded in a T75 flask.

Tuesday: HEK293T cells is seeded in a T175 Flask.

Thursday: HEK293T cells are ready to be harvested. For T175 flask, the original supernatant is removed and 6 ml of trypsin is put into the flask and incubated at $37^oC/5\%$ $CO_2$ for 5mins then centrifuged at 1000rpm for 5min at RT. The cell number is counted and diluted to 0.5 x $10^5$ cells/ ml and added at 1ml per well in a 12-well plate.

Friday: the immortalised MyD88$^{-/-}$ macrophage cells are plated at $0.25x10^5$/ml in a 12-well plate. Genejuice and DNA plasmids (pCMV-MD2.G, pCMV-dR8.91, and pHR-MYD88-GFP *Latty et al*) are put into HEK293T cells in a 12-well plate and incubated for 72 hours.

The next Monday: The supernatant containing lentivirus in HEK293T wells are clarified and added into wells containing the immortalised MyD88$^{-/-}$ macrophage cells and incubated for overnight.

The next Tuesday: The viral supernatant in the wells containing the immortalised MyD88$^{-/-}$ macrophage cells is replaced with fresh media. The MyD88$^{-/-}$ GFP macrophages are checked by fluorescence microscopy before use.

### 3.5.2 Nanopipette preparation

Nanopipettes were fabricated from quartz capillaries, with an outer and inner diameter of 1 mm and 0.5 mm respectively. A laser pipette puller (Model P-2000, Sutter Instrument, CA) was used for fabrication. Since the sonicated amyloid-β fibrils are macromolecules, the nanopipette should have larger tip size to enable fibrils to pass through. In contrast with the laser puller settings described in Chapter 2, the parameter (HEAT = 400, FIL = 4, VEL = 30, DEL = 200) was used to pull a pipette with an internal diameter of 1 μm (± 200 nm).

### 3.5.3 Amyloid-β fibril synthesis

The lyophilized Aβ42 peptide (Stratech, Cat. No. A-1170-2-RPE-1.0mg) was dissolved in PBS (pH = 7.4) at 200 μM on ice. The solution was quickly aliquoted and snap frozen. To prepare Aβ42 fibrils, an aliquot was thawed and diluted to 4 μM in 1xPBS supplemented with 0.01% $NaN_3$ (Merck, Cat. No. 71290) and incubated at 37 °C under quiescent conditions for one week. To obtain sonicated Aβ42 fibrils, the mixture was immersed and sonicated (Q125AUK-220 and 4422, Wolflabs) at 20 kHz with 40 % of power for 24×5 s bursts with 15-s rests between bursts. Thereafter, the sonicated material was centrifuged, aliquoted and snap frozen. The aliquots were stored at -80 °C until use.

### 3.5.4 Imaging Aβ oligomers using SiMPull based dSTORM imaging

This method is based on a previous report[108]. An APP-binding antibody (6E10, Mouse IgG1, Biolegend, Cat. SIG-39320) was immobilised on a PEGlyted coverslip via a biotin-Neutravidin bridge. 500 nM (monomeric concentration) sonicated Aβ fibrils were loaded onto the coverslip for 30 minutes, followed by two wash steps with 0.05% (v/v) PBST (PBS + Tween 20), and once with 1% (v/v) PBST. The coverslips were blocked using 0.1% (w/v) bovine serum albumin (Thermo Scientific, Cat. AM2616), 10% (v/v) salmon sperm (Thermo Scientific, Cat. 15632011) and 0.1% (v/v) PBST for 1 hr at room temperature. The coverslips were labelled with 6E10 (500 pM) and then incubated for 45 minutes, followed by 3 wash steps with 0.05% (v/v) PBST. dSTORM imaging was carried out in the same common glucose system described previously. Data analysis was carried out using a custom ImageJ macro. The drift was corrected using the NanoJ plugin[109], and localisations were identified using ThunderSTORM[110]. Topography analysis was carried out using the Topography library plug-in[111].

### 3.5.5 Nanopipette delivery of LPS and sonicated Aβ fibrils

1 μg/ml LPS and 4 μM monomer concentration sonicated Aβ fibrils were loaded into the nanopipette and the procedure described in Chapter 2 was used to deposit these molecules onto macrophage. In contrast to previous work which used a voltage pulse for delivery, a pressure pulse (3 kPa for 1 second) was used to deliver sonicated Aβ fibrils, due to their large size and molecular weight.

### 3.5.6 Light sheet live cell scanning and 3D reconstruction

The optical path of the light sheet microscope was fully described in Chapter 2. The scanning was achieved by moving the piezo sample stage. Controlled by FPGA, the movement of the sample stage was synchronized with acquiring the camera image. Starting from the coverslip surface, the stage was moved by the piezo with 100 steps, with a step size of 200nm. The total scan range is 20 μm, which is enough to cover the whole cell. The camera triggering mode was set with an edge trigger, where the camera will acquire a frame only when it receives a 5 volts TTL digital signal. When the sample stage was driven to a new section in the Z direction, the FPGA would generate a digital TTL signal and send it to camera in order to acquire a frame. This synchronization enabled each Z scanning section could be imaged accurately for the 3D reconstruction. The time interval between two scans was 10 second, after nanopipette delivery the cell was scanned by light sheet microscope for 200 rounds which took around 30mins. After image acquisition, the images were assembled into a hyperstack in the order of XY section, Z scan and time. Then the hyperstack was reconstructed into a 3D projection and volume rending using a plugin embedded in FIJI. All the live imaging was performed in a 37ºC incubator with 5% carbon dioxide atmosphere.

### 3.5.7 Myddosome live tracking

The analysis of images was carried out using Fiji (ImageJ) and auto tracking algorithm written in Matlab. The raw images were assembled into hyperstacks in the order of xy section, z scan and time. Then the hyperstacks were background subtracted using a rolling-ball algorithm (rolling ball radius = 80 pixels) and 3D Gaussian blurred (radius = 1 pixel). At last, the hyperstack was reconstructed into 3D projection and volume rending by the plugin embedded in FIJI.

Myddosomes in the 3D projections were identified using the Find Maxima plugin (prominence over background intensity = 20) and isolated into a new stack for tracking algorithm. The reason why we recruited find maxima as a filter to extract the assembled Myddosome position information is that the 2D tracking algorithm would treat the edge of cell membrane as a tracking spot which would result in huge background noise when the raw images were analysed. The extracted Myddosome stacks were analysed by MATLAB code (MathWorks) based on the Crocker-Grier algorithm, providing temporal information about the tracked trajectories

(figure 3.23). The following parameters were using in the tracking algorithm to minimise the false detection of noise and reduce the number of lost tracks: a) search range = 8 px; this is the maximum distance a spot can move between frames, and be counted as the same spot, b) memory = 6 frames (60 seconds); the maximum number of frames where a spot can vanish, reappear and be considered the same particle (this is important as the maxima fitting potentially misses spots occasionally), minimum track length = 2 frames (20 seconds).
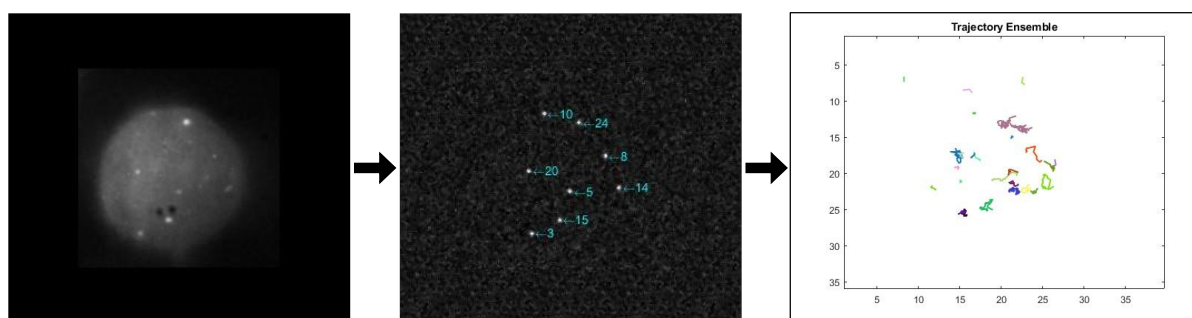


**Figure 3.23.** Overview of 2D tracking analysis. From left to right: z-stacks for each time frame were projected into one frame. The Find maxima plugin was used to convert the MyD88 puncta into spots, which were detected and tracked using the Crocker-Grier method (custom MATLAB code). Analysis could then be carried out on the tracked trajectories

### 3.5.8 Myddosome Kinetics analysis

The 2D tracking analysis provided us with the information about the total number of tracking and the starting and ending frame number of each tracked puncta. Before analysing the time point of the first Myddosome formation, lifetime and total number of Myddosome, the preformed Myddsomes present before nanopipette delivery must be removed. In the tracking analysis results, we deleted the Myddosomes that were tracked on the first frame of 3D projection to avoid the effect of preformed Myddosome.

The time point when the first Myddosome was detected was determined by finding out the earliest frame where spot tracking started. The lifetime of Myddosome was calculated by the difference between the starting and ending frame number of each tracked spot. The total number was determined by the total tracked spot number minus the number of tracked spot in the first frame.

### 3.5.9 dSTORM imaging of Myddosome

Macrophages were plated in DMEM + 10% FBS and allowed to sit down on a glass-bottom confocal dish (VWR International) overnight. The media was replaced with new media supplemented with either LPS (1 mg/mL) or aβ fibrils (monomer concentration 0.1 mM) and stimulated for 5 different time periods: 30mins, 3 hours, 6hours, 12 hours and 24 hours. Following triggering, the cells were washed 3 times with PBS and then fixed (0.8% PFA, 0.1% GA in PBS) for 15 minutes at 4°C. Following washing, the cells were stained with 6.7 μg/mL of an Alexa Fluor™ 647 conjugated anti-GFP rabbit polyclonal antibody (Invitrogen) for 20 minutes at 4°C. The cells were then washed a further 3 times with PBS prior to imaging. dSTORM imaging was carried out with 50 mM PBS-Tris, 0.5 mM glucose, 1.3 μM glucose oxidase, 2.2 μM catalase, and 50 mM mercaptoethylamine. The dSTROM images were acquired by TIRF microscopy. 190 mW 638 laser with exposure time 10 ms and 2000 frames were collected for each field of view. The data analysis was performed using a home-written ImageJ macro.

### 3.5.10 Myddosome size measurement

Myddosome sizes of MyD88-GFP tagged cells were characterised after fixing the cells and tagging with an anti-GFP antibody, followed by dSTORM imaging. Myddosomes were identified by looking for overlap of puncta in the 488 nm (GFP) and 635 nm (antibody) channels. Following identification, the size of the Myddosomes were measured by fitting a 1D Gaussian to the pixel intensities of the super-resolved puncta and recording the standard deviation of the Gaussian profile as described in Chapter 2.

## 3.6 Conclusion and Discussion

In this chapter, the ldSPIM was applied to study TLR4 signalling and Myddosome formation triggered by protein aggregates implicated in neurodegeneration, such as Aβ fibrils. Similar to the canonical TLR4 agonist LPS, the sonicated Aβ fibrils delivered from the nanopipette were observed to interact with TLR4 and trigger Myddosome formation, demonstrating that Aβ fibrils could induce a neuroinflammatory response through TLR4 activation.

The similarities and differences in Myddosome signalling kinetics between sonicated Aβ fibrils and LPS stimulation were characterized in the following five aspects: the first time point when a Myddosome first formed, the Myddsome lifetime the total number of oligomers formed within 30mins upon triggering, the Myddosome size and the change in the Myddosome size with stimulation time. From the results we showed that apart from the total number of Myddosomes formed, the other four factors mentioned above all showed a T test significant difference between LPS and sonicated Aβ fibrils stimulation. Firstly, we observed that LPS triggered Myddosomes formed faster than sonicated Aβ fibrils. The difference in lifetime and size of the Myddosomes shows the same trend between LPS and Aβ fibrils, in which the Aβ-triggered Myddosomes have a longer lifetime and larger size. By correlating the total number data and lifetime data by applying a lifetime threshold (> 50 seconds), the number of LPS-triggered Myddosomes were shown to be slightly more than the sonicated Aβ-triggered Myddosomes. However, if we look at the ratio of the number of Myddosomes which last longer than 50s vs the total number, there was no significant difference between sonicated Aβ fibrils and LPS.

From our analysis, we demonstrated that the assembly of Myddososmes triggered by sonicated Aβ fibrils had different signalling kinetics compared with LPS. Since Myddosome assembly regulates the activation of NF-κB and downstream cytokines secretion, we plan to work out which factors of the Myddosome assembly kinetics among the five aspects described above plays the major role in controlling the inflammatory signalling intensity. The first time point when the Myddosome formed represents the Myddosome assembly speed, which is more related to the binding affinity of stimulus and TLR4 rather than the extent of signalling. The LPS triggered Myddosome formed faster than Aβ-triggered ones, suggesting that the binding affinity between LPS and TLR4 is higher than Aβ fibrils. The total number of assembled

Myddosomes triggered by LPS and sonicated Aβ fibrils did not show a significant difference, suggesting that it is unlikely to be a factor influencing Myddosome signalling. Therefore, we propose that the lifetime and size are the major factors to affect Myddosome downstream signalling. This hypothesis is supported by a recent study, in which Taylor et al[107] showed that only longer lived and larger Myd88 puncta are able to recruit IRAK2/4 to form signalling Myddosomes while Myd88 puncta with shorter lifetimes and smaller size are rapidly degraded and disassembled.

According to our group's previous work, Latty et al[84] observed that LPS stimulation triggered rapid Myddosome assembly and disassembly (within 3mins). Our data shows consistent results with the literature, in which the LPS triggered Myddosomes have the similar average lifetimes. We presume that the sonicated Aβ fibrils which are larger than LPS may form Myddosomes of larger size which may last for longer and it is not clear how this will affect the down-stream signalling process and the amount of pro-inflammatory cytokines produced by the cell.

Another aspect that we want to discuss is the activation mechanism of TLR4 triggered by sonicated Aβ fibrils. Current structural analysis of TLR4 suggests that when band to LPS, the TLR4/MD2 co-receptor assembles into a hetero-tetramer and induces dimerization of the cytosolic Toll/interleukin-1 receptor (TIR) domains to recruit downstream signal transducers. Latty et al also found that when stimulated by LPS, there are more TLR4 dimers forming on the cell surface and higher order oligomerization of TLR4 was also observed. However, how the sonicated Aβ fibrils interact with TLR4 is unknown. In the future, TLR4 will be labelled ether by HALO tag or antibody to test whether the sonicated Aβ fibrils would stimulate higher order oligomerization of TLR4 or just the same as LPS to trigger TLR4 dimerization.

Finally, we will discuss the size change in different stimulation periods. According to previous work[112–114], the LPS triggered Myddosome signalling process has a negative feedback control system. During LPS stimulation, a short Myd88 isoform called Myd88 short (Myd88s) rather than the normal Myd88 is recruited. Myd88s lacks the intermediate domain (ID) for IRAK recruitment and thus it is signalling incompetent. We cannot distinguish between signalling competent and signalling incompetent Myddosomes from our experiments. However, the literature shows that TNFa production reaches a plateau after 16 hours before decreasing and the expression of TNF RNA reached a maximum after 6 hour before halving by 24 hours,

while TNFa production continues to increase with Aβ aggregates [105,115,116]. Therefore over the time-scale of our experiment predominantly signalling competent Myddosomes appear to be formed.

Our study of the MyD88 oligomer size with stimulation time is consistent with this and showed that larger size Myddosomes formed over time for both LPS and sonicated Aβ fibrils. This increase in size correlates with published increased production of TNF suggesting that the size of the Myddosomes formed controls the extent of signalling and TNF a production. To directly test whether the Aβ-triggered Myddosomes formed after different stimulation time periods is signalling or just a Myd88 oligomer, further experiments will be designed. We propose two strategies. The first one is to correlate the cytokine secretion level detected by ELISA with the size of the Myddosome formed in different stimulation time periods. If the cytokine level such as TNF-α increased with longer stimulation period, it will support that the Myddosomes with larger size are still signalling. Another strategy is labelling IRAK2/4 to visualise the IRAK recruitment into the Myddosome formed after different stimulation time periods to determine whether the Myddosomes can signal.

# Chapter 4
# The application of ldSPIM in studying Type I interferons receptor kinetics in cell surface

This chapter describe the work in collaboration with Dr. Stephanie Huang in Monash University. We demonstrated the application of nanopipette delivery in characterising the surface kinetics of the interaction between IFNβ and interferons receptor (IFNAR). IFNβ was delivered to mouse embryonic fibroblasts (MEFs) expressing HALO tagged IFNAR1 and SNAP tagged IFNAR2, which are the two subunits of IFNAR, and the diffusion of IFNAR was imaged by TIRF immediately after delivery. Analysed by an auto tracking algorithm, the kinetics of IFNAR1 and IFNAR2 before and after IFNβ stimulation were characterized for motility, abundance, and heterodimeric complex formation.

**Contribution**

Bing Li is responsible for the microscope and single molecule TIRF imaging and data analysis.

Dr. Stephanie Huang is responsible for cell culture and receptor labelling.

## 4.1 Introduction

Interferons (IFNs) are widely expressed cytokines that work as the first line of immune defence against viruses, bacteria, parasites and fungi, directly and/or indirectly through the induction of other mediators. Type I IFNs are one of the most common classes of IFN families, which bind the transmembrane receptors IFNAR1 and IFNAR2, triggering internalisation and activation of downstream cascades[117]. Despite the importance of IFN signaling in innate immunity, little is known about receptor surface kinetics and trafficking, how this couples to different pathways and whether the distribution of the receptor subunits influences signaling. With the development of single molecule imaging technologies such as fluorescence resonance energy transfer microscopy (FRET) and total internal reflection fluorescence microscopy (TIRF), the interferon receptor kinetics and dimerization have been characterized in the physiological context[118–120]. Through the formation of ternary complex of IFN, IFNAR1 and IFNAR2, Lamken et al[121] and Stark et al[122] suggested that the IFNβ first binds to IFNAR2 then this leads to the recruitment of IFNAR1. de Weerd et al[123] also demonstrated that IFNβ is able to bind to IFNAR1 alone and generate a signal independently of the IFNAR2. Stimulation with INFα and IFNβ has also been demonstrated to induce the internalisation of IFNAR1 and IFNAR2 with different speeds. INFα can induce the recycling of IFNAR to cell surface and the IFNβ is able to transfer IFNAR to lysosomal degradation[124,125].

In order to characterize the kinetics of the INF/ IFNAR1/IFNAR2 complex, Wilmes et al[118] revealed that no colocomotion of IFNAR1 and IFNAR2 was observed in the absence of INFs, and after the addition of saturating concentration of INFs then strong colocomotion was observed. Compared with unstimulated IFNAR, the INFs triggered receptors showed significantly reduced mobility, with INFα inducing around 70% INF/ IFNAR1/IFNAR2 complex formation and IFNβ yielding around 85% dimerization of IFNAR1 and IFNAR2.

In this chapter, we will focus on the interaction between IFNβ, which is one of the best-defined and most broadly expressed type I IFNs, and IFNAR1 and IFNAR2. The effect of IFNβ binding with IFNAR1 and IFNAR2 are characterized with regard to their diffusion co-efficient, total receptor number and co-localisation.

## 4.2 Single molecule tracking algorithm resolves and quantifies receptor population

Transduced mouse embryonic fibroblasts (MEFs) expressing Halo tagged IFNAR1 and SNAP tagged IFNAR2 were used to study receptor kinetics. The fluorescence signal from IFNAR1 and IFNAR2 on the bottom surface of MEFs were acquired using TIRF and quantified using the single-particle tracking algorithm developed by Laura Weimann $et$ $al$[126]. This algorithm detects molecules whose fluorescence intensity is above a certain magnitude of signal to noise ratio (SNR) and generates the trajectory of each tracked spot to calculate the diffusion coefficient (figure 4.1 a and b). The distribution of membrane receptor diffusion coefficient is split into two populations, a mobile fraction, $f_1$, and an immobile fraction, $f_2$. Their respective diffusion coefficients are also calculated and denoted $D_1$ for the mobile population 1 and $D_2$ for the immobile population (figure 4.1 c).
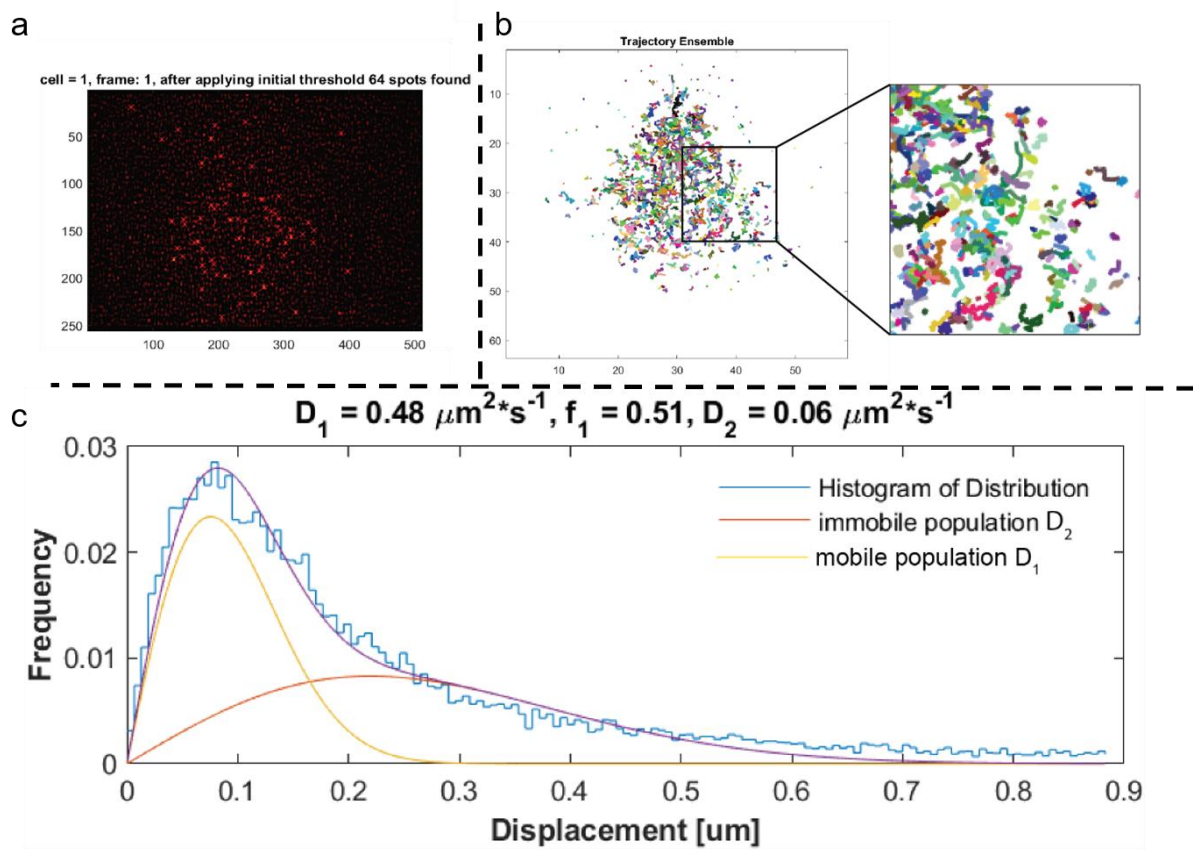


**Figure 4.1.** a) Tagged receptors are observed as individual spots on the cell surface. Only those spots with fluorescence intensity above the SNR threshold are selected and displayed by single-molecule tracking algorithm. b) The trajectory of each tracked spot. c) A histogram of distribution is created of the diffusion co-efficients, and assuming a heterogeneous population of diffusing species, these are dissected into two diffusing populations, $D_1$ (mobile population) and $D_2$ (immobile population)

## 4.3 Diffraction limited image of IFNAR1 and IFNAR2

In our experiment, since the HALO tagged IFNAR1 and SNP tagged IFNAR2were imaged together using a two channel-splitter, with a combination of HALO photoactivable (PA) 646 dye and SNAP TMR to label them respectively. The reason why using PA646 dye is that the MEFs exhibited high levels of auto fluorescence in the red channel and the PA646 dye can be activated by a 405nm laser to emit brighter fluorescence, making it possible to distinguish the true receptor population from the background signal (figure 4.2). The real signal of PA646 dye labelled HALO tagged IFNAR1 can be filtered by minus the fluorescence of signal acquired from frames after 405nm laser activation with the averaged fluorescence intensity of background. The signal to noise ratio (SNR) of the auto fluorescence and the real labelled IFNAR were calculated and listed in figure 4.3 A). Both IFNAR1-Halo PA646 and IFNAR2-SNAP TMR exhibit a higher SNR compared to control cells, indicating that the true signal of IFNAR can be distinguished by the auto tracking algorithm. The track length or the life time of each spot, which is the number of frames that one spot can last, is also calculated. In Figure 4.3 B), the IFNAR1-Halo PA646 exhibits longer lifetime on the cell surface compared with control while the IFNAR2-SNAP TMR shows similar dwell times to control. This difference is caused by the photostability of PA646 dye and TMR.

405 activation

control

IFNAR1 HaloPA

frame 0    frame 250    frame 500    frame 750    frame 1000
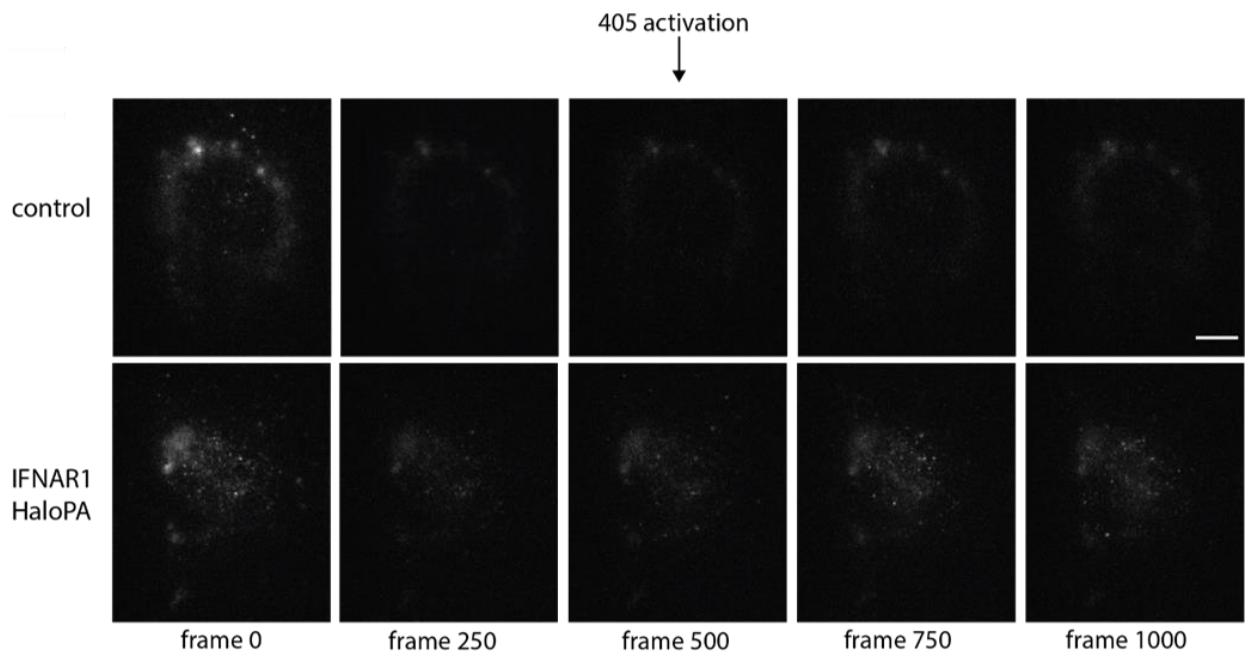
**Figure 4.2.** The diffraction limited TIRFM images at frames 0, 250, 500, 750 and 1000 of an untransduced cell and one expressing a Halo-tagged IFNAR1, both incubated with a photoactivatable (PA) Halo-tag ligand, which is activated by a 405nm laser at 500 frames to identify the true receptor population from the background fluorescence. Scale bar is 10 μm.



A

B
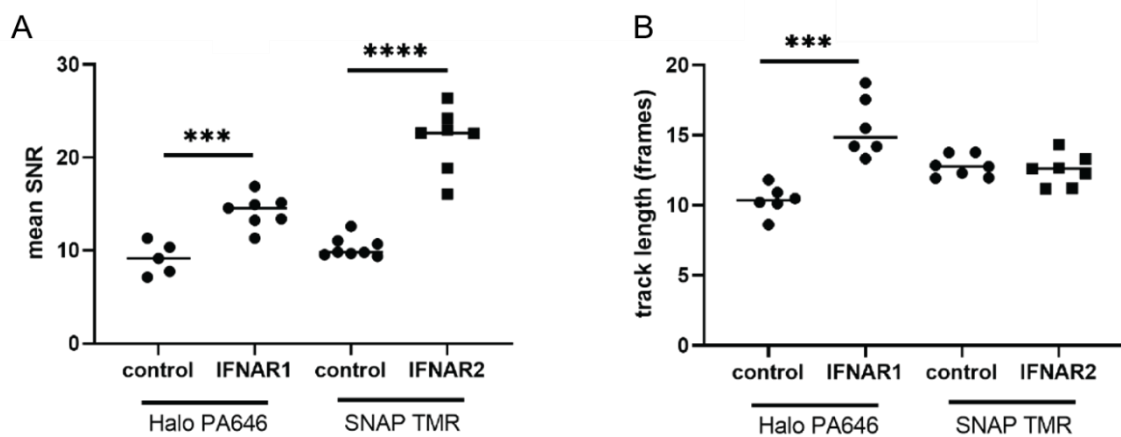
**Figure 4.3.** A) Signal to noise ratio (SNR) and B) track length were calculated for untransduced cells, IFNAR1-Halo and IFNAR2-SNAP incubated with Halo PA 646nm ligand and SNAP TMR ligand, using the single-molecule tracking algorithm. These were subsequently used as parameters with the same algorithm to eliminate background and detect the true receptor population. n = 5 – 8. ***$p < 0.001$, ****$p < 0.0001$. Unpaired t-test.

**4.4 The IFNβ reduces diffusion coefficient of co-expressed IFNAR1 and IFNAR2**

In this section, three kinds of MEFs were generated: Ifnar1$^{+/-}$ MEFs only expresses IFNAR1, Ifnar1$^{-/+}$ MEFs only express IFNAR2 and Ifnar1$^{+/+}$ MEFs expressing both receptor subunits. Before adding IFNβ, the IFNAR1 and IFNAR2 expressed alone exhibited a similar diffusion coefficient in both mobile and less-mobile population (0.1 μm$^2$/s for the mobile population and 0.02 μm$^2$/s for the less-mmobile population). The co-expressed IFNAR1 and IFNAR2 had a higher baseline for the diffusion coefficient in the mobile population at around 0.2 μm$^2$/s while the less-mobile population shared a similar value of diffusion coefficient with IFNAR1 and IFNAR2 expressed alone. After IFNβ delivery to the MEFs surface by the nanopipette, the diffusion coefficients of IFNAR1 and IFNAR2 expressed alone did not change in both populations. In contrast, the diffusion coefficient of co-expressed IFNAR1 and IFNAR2 displayed a significantly decrease in mobile population while the diffusion coefficient of less-mobile population remains unchanged.

These results indicated that a single receptor binding to the IFNβ does not lead to a change in diffusion. The reduced diffusion coefficient is mainly caused by IFNβ induced dimerization of IFNAR1 and IFNAR2 ligand (figure 4.4).
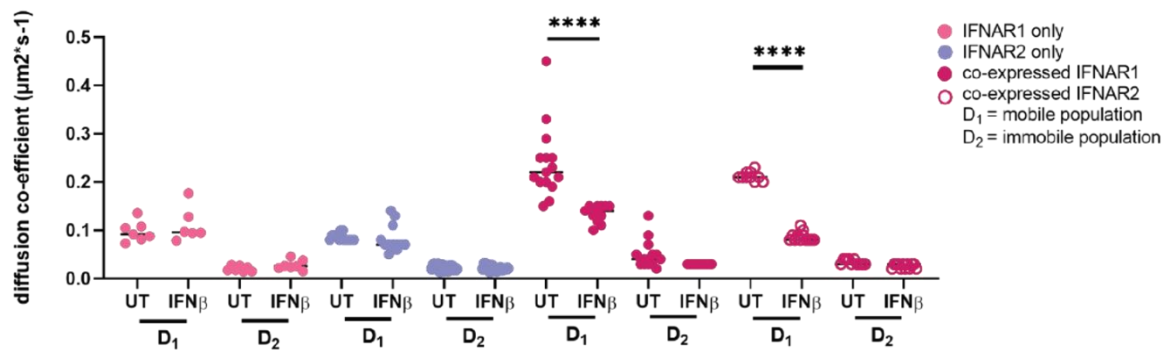


**Figure 4.4.** The diffusing spots are split into the mobile population, D$_1$, and the less-mobile population, D$_2$. IFNAR1 and IFNAR2 expressed alone show no change in diffusion co-efficient upon addition of IFNβ, whereas co-expressed subunits decrease significantly in surface mobility following IFNβ treatment. D$_1$ of the total diffusing population shows no change for IFNAR1 and IFNAR2 expressed alone after addition of IFNβ. n = 7 – 14 for each condition. Each dot represents a single cell. **$p < 0.01$, ****$p < 0.0001$. One-way ANOVA with significance derived from Tukey's multiple comparisons test.

## 4.5 The IFNβ induced co-localization of IFNAR1 and IFNAR2

To further test whether the addition of IFNβ will lead to the dimerization of IFNAR1 and IFNAR2, the co-localization of two receptors, percentage of coincidence, was calculated. In figure 4.5, when the distance for coincidence is set as less than 500nm, there is no obvious coincidence for all cell types but a small, not significant decrease (T test) for cells co-expressing IFNAR1 and IFNAR2 after IFNβ addition. This possibly hints that there might be some pre-dimerization of IFNAR1 and IFNAR2. This might also explain why there is two diffusing populations. The unassociated IFNAR1 and IFNAR2 could move freely and is treated as the mobile population, while the pre-dimerized IFNAR1 and IFNAR2 contribute to the less-mobile population (figure 4.6).
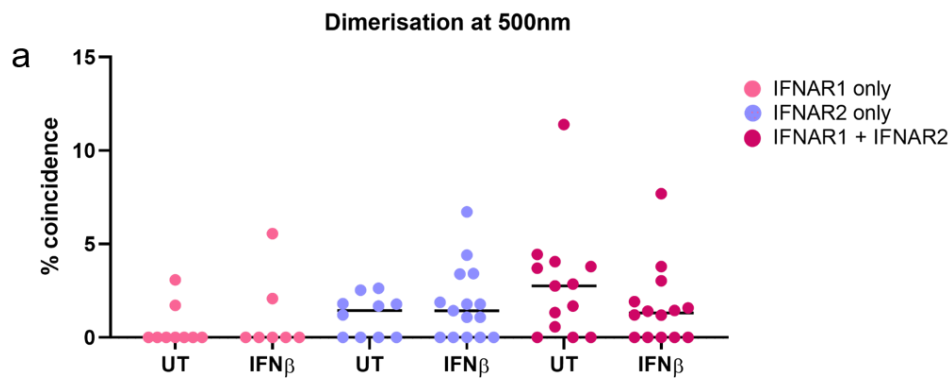


**Figure 4.5.** a) The coincidence of IFNAR1 and IFNAR2 at co-localization at distance of 500 nm. No significant difference was find before and after IFNβ addition. A small but not statistically significant decrease in co-localization coincidence was observed after IFNβ addition.
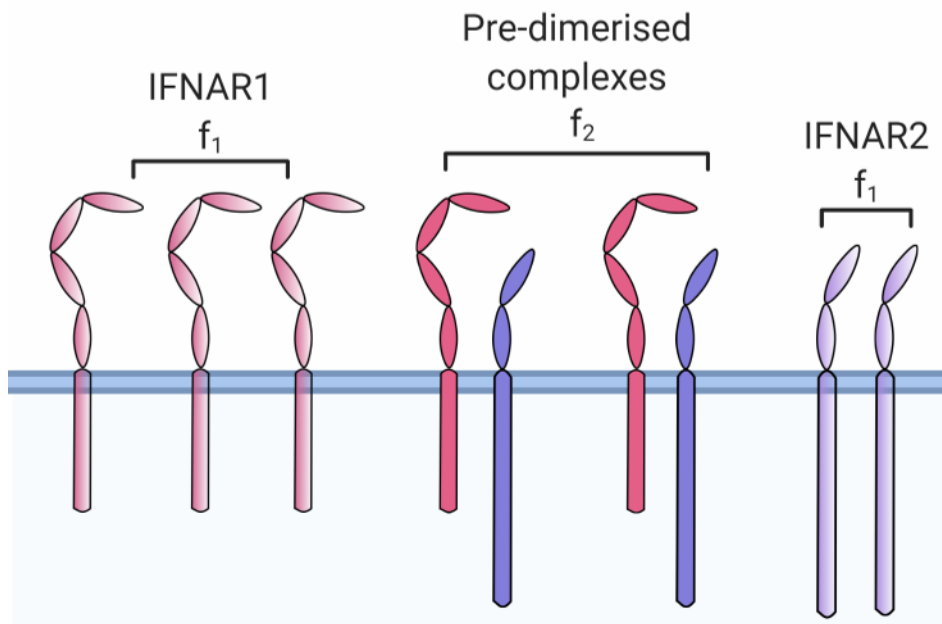
**Figure 4.6.** Schematic of co-expressed IFNAR1 and IFNAR2 on cell surface. The unpaired IFNAR1 and IFNAR2 have higher diffusion coefficients which belongs to the mobile population. The pre-dimerised IFNAR1 and IFNAR2 complexes contribute to the less-mobile population.

## 4.6 IFNβ induces depletion of IFNAR1 mobile fraction

In addition to the decrease of the diffusion coefficient of co-expressed IFNAR1 and IFNAR2 in the mobile population, the IFNβ stimulation might also reduce the number of tracks for IFNAR1 co-expressed with IFNAR2. As the tags are intracellular, the disappearance of signal can perhaps be explained by the ubiquitination of IFNAR1 and subsequent degradation to completely remove the conjugated tag and fluorescent ligand. According to a previous study, IFNAR1 can be rapidly endocytosed from the cell surface and heavily ubiquitinated within 5min of IFNβ addition. Compared with IFNAR1, the co-expressed IFNAR2 did not show a significant change of track number after IFNβ stimulation, which may be explained by less ubiquitination of this subunit or rapid recycling of the subunit to the cell surface (figure 4.5)[125].



**Figure 4.7.** The track number of mobile IFNAR1 co-expressed with IFNAR2 decreased significantly upon IFNβ deposition. n = 7 – 14 for each condition. Each dot represents a single cell. **$p < 0.01$, ****$p < 0.0001$. One-way ANOVA with significance derived from Tukey's multiple comparisons test.

## 4.7 Materials and methods

### 4.7.1 Tag the IFNAR1 and IFNAR2 with HALO or SNAP ligands.

Human IFNAR1 and IFNAR2 were cloned into pHR (Courtesy of Bryant lab) backbones under the control of the spleen focus-forming virus (SSFV) promoter and pL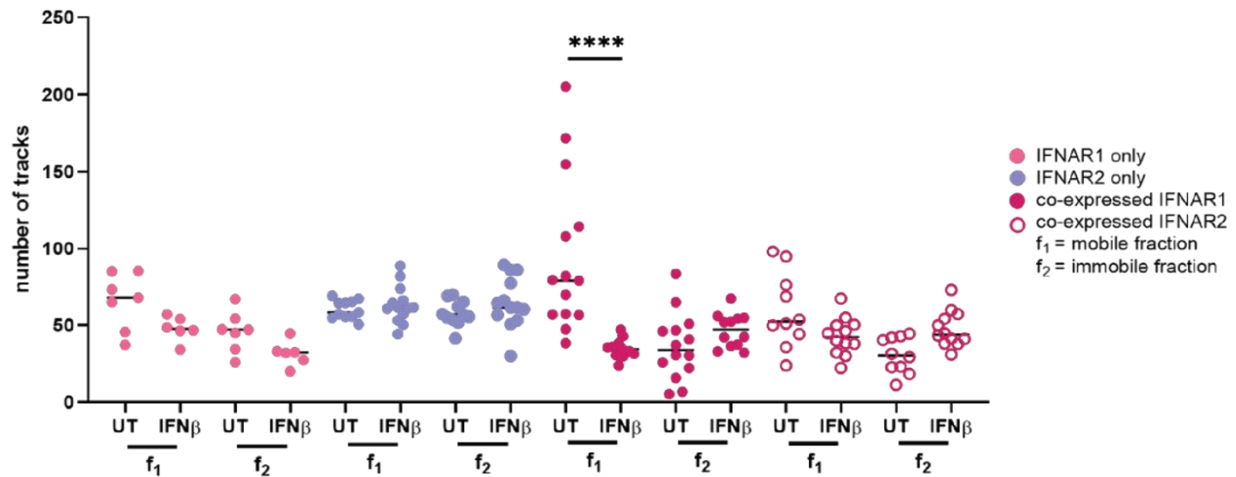VX (Clontech) backbone under the control of the cytomegalovirus (CMV) promoter. IFNAR1 was fused to a C-terminal GFP or SNAP tag (pHR IFNAR1-GFP and pHR IFNAR1-SNAP) via the insertion of full length IFNAR1 using the MluI (primer sequence: GATTAGACGCGTATGATGGTCGTCCTCCTG) and BamHI (primer sequence: GCGCGGATCCTACAAAGTCCTGCTGTAGTTCTTCACTTGTTTTACTTTCG) restrictions sites. IFNAR2 was also fused to the same C-terminal tags (pHR IFNAR2-GFP, and pHR IFNAR2-SNAP) via MluI (primer sequence: GCGACGCGTATGCTTTTGAGCCAG AATGCCTTCATCGTCAGATCACTTAATTTGGTT) and BglII (primer sequence: GCGCAGATCTTCTCATTATATAACCATCCCCAAG) restriction sites (错误!未找到引用源。 **& 2**). IFNAR1 and IFNAR2 fused to a C-terminal Halo-tag (pLVX IFNAR1-HaloTag and pLVX IFNAR2-HaloTag) were generated using Clone EZ® (Genscript).

The C-terminal reporter tags used are:

1. EGFP, a variant of GFP, an innately fluorescent protein isolated from jellyfish Aequorea victoria, that contains chromophore mutations to increase brightness by 35-fold and codon optimised for higher expression in mammalian cells;

2. HaloTag, a 33kDa haloalkine dehalogenase that acts as a hydrolase to catalyse a reaction, forming a covalent bond with a synthetic ligand consisting of a chloroalkine linker and a functional group[127]. In this case, the functional group used will be a fluorescent tag to enable visualisation using total internal reflection;

3. SnapTag, a 19.4kDa mutant DNA repair protein O6-alkylguanine-DNA alkyltransferase, that catalyses a reaction with benzylguanine derivatives for covalent labelling with synthetic ligands.

### 4.7.2 Transfection and viral transduction

Cells were cultured in Dulbecco's Modified Eagle Media (DMEM, Gibco) supplemented with 10% fetal bovine serum (Bovogen) without the addition of antibiotics and incubated at 37°C

and 5% $CO_2$. Lenti-X cells were plated in 6 well plates (Greiner Bio-One) at 70% confluence and transfected with 1μg psPAX2 (envelope protein), 0.1μg VSVG (packing vector), 1μg tagged IFNAR1 and 1μg tagged IFNAR2 at a 2:1 ratio with jetPEI DNA Transfection Reagent (Polyplus). *Ifnar1$^{-/-}$* mouse embryonic fibroblasts (MEFs) were plated in 6 well plates (Greiner Bio-One) at 70% confluence 20hrs prior to transduction. Supernatant was collected at 72hrs post transfection and filtered through a 20μm syringe filter (Whatman). *Ifnar1$^{-/-}$* MEFs were transduced with viral supernatant and 1μg of polybrene was added to reduce membrane repulsion of viral particles. Viral supernatant was removed 18hrs post transduction and replaced with fresh complete medium. Stable transduction of MEFs was confirmed using fluorescence microscopy.

### 4.7.3 Live cell labelling and single molecule imaging

To minimise the background from non-adsorbed dye molecules, transduced MEFs were plated on plasma cleaned (Harrick Plasma) glass coverslips coated with 5μg/mL fibronectin (Sigma-Aldrich) and incubated in phenol free DMEM (Gibco) supplemented with 10% fetal bovine serum without antibiotics for 24 hours prior to imaging. Cells were incubated with 100nM Halo JF646 photoactivatable dye (Lavis Lab, Janelia Campus) and 120nM SNAP-cell TMR Star (NEB) at 37˚c for 15 minutes, followed by three 30minute complete medium replacements to remove unbound dye. Cells were then washed three times with PBS and the coverslip was secured in an Attofluor cell chamber (ThermoFisher) with 1mL of PBS overlaid for single molecule imaging.

Total internal reflection (TIRF) experiments were carried out on an inverted microscope (Eclipse TE 200; Nikon) coupled with an electron multiplying charge coupled device (EMCCD) (Photometrics, Evolve Delta 512). A 60x magnification objective lens with a numerical aperture of 1.49 was used for TIRF microscopy. SNAP TMR ligand was excited using a 561 nm laser diode and filtered by a 580/14nm bandpass filter (Edmund Optics) Photoactivatable Halo JF646 was excited by a 405nm laser diode (Cobolt) at 150 mW and filtered by a 708/75nm bandpass filter (Edmund Optics).

### 4.7.4 Dual-view installation and colocalisation optimisation

For dual colour imaging, the two dyes were excited using the same lasers described above and fluorescence was detected using a spectral image splitter (Teledyne Photometrics) with a 605nm cut-off wavelength dichroic beam splitter (Teledyne Photometrics) in combination with a 708/75nm bandpass filter for detection of SNAP TMR and 580/14nm bandpass filter for the detection of Halo JF646, projecting each channel into 512 x 256 pixels. Stacks of 2000 frames were acquired with a time resolution of 33ms/frame. Imaging was performed at room temperature in PBS. For receptor dimerisation studies, cells were incubated with 1000IU/mL of IFN for 5min to ensure diffusion of ligand before acquisition of images.

To set up dual-colour imaging on the TIRF microscope, we installed a spectral image splitter with a dichroic beam splitter to detect both 646nm and 554nm wavelengths emitted from the two labelled receptors on the same sample.

Untransduced cells were used to control for background fluorescence and noise; cells expressing IFNAR1 only were used as control for zero binding events (as there was no binding partner), and any coincidence detected would be a false positive; cells co-expressing IFNAR1 and IFNAR2 were used to probe for true coincidence. All cells were stimulated with 1000IU/mL IFNβ, with images acquired 5mins post stimulus and a 405nm pulse delivered at 30 seconds to activate the JF646 photoactivatable dye on IFNAR1. All % coincidence was calculated for IFNAR1-Halo JF646, as this was the rate limiting subunit, and all binding events were normalised to untransduced control.

### 4.7.5 Image analysis for single-molecule tracking and co-localisation

TrackMate was used for single molecule tracking to resolve dwell time of receptor subunits on the cell surface and measure velocity (mean, minimum and maximum) of IFNAR1 and IFNAR2 expressed alone or together at baseline and following stimulation with IFNβ. A difference of Gaussian filters was used to detect the single molecules, using an estimated spot diameter of 1μm and a threshold value of 43.

A single molecule tracking algorithm[126] executed in MATLAB (release 2019b, The MathWorks Inc.) was used to identify and split tracks into two populations of different diffusion coefficients under the assumption that molecules being analysed are membrane bound receptors.

For co-localisation analysis, the image acquired presents the 554nm channel on the top half of the display and the 646nm channel on the bottom half of the display, shown on the left of 错误!未找到引用源。. A FIJI script was written to first subtract background fluorescence, then split the channels into IFNAR1 JF646 and IFNAR2 TMR, shown in the middle of schematic in 错误!未找到引用源。figure 4.8. Each channel was then analysed using the single-molecule tracking algorithm described above to create individual trajectories of each spot[126], and paired trajectories (ie. tracks detected in 646nm and 554nm channels) for each cell was analysed by Dynamic Single-Molecule Co-localization, or DySCo[127], for co-locomotion. Molecules were considered co-localised if found within 500nm of eachother for >300ms. Co-localisation, or coincidence is calculated as:

$$\% \, Coincidence = 100 \, \times \frac{number \, of \, colocalised \, tracks \, in \, 646nm \, channel}{total \, number \, of \, tracker \, in \, 646nm \, channel} \, ,$$

Therefore, the maximum % coincidence possible is 50%, as this equation calculates the percentage of molecules from the rate limiting population and its co-localisation events with the higher efficiency population.

A subsequent algorithm (DySCo) was used to identify the coincidence of tracks formed by IFNAR1 and IFNAR2 in each frame to an average precision of around 20nm. Receptors were considered co-localised if molecules were within 500nm for ≥5 frames (≥165ms). Coincidence values were calculated in relation to IFNAR2 as this exhibited lower expression levels, therefore also the rate limiting partner.
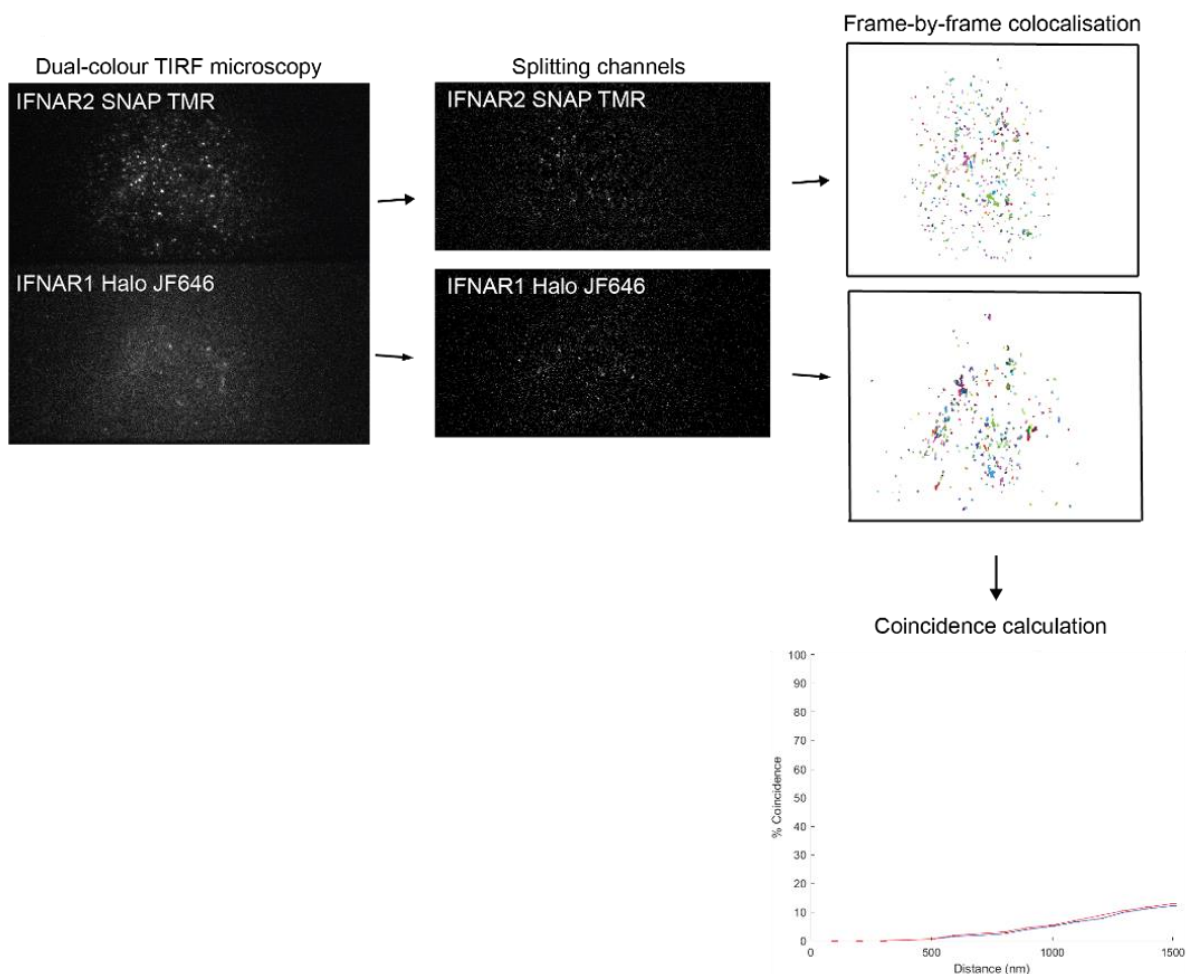
**Figure 4.8.** The dual view image splitter and co-localization analysis.

## 4.8 Conclusion and Discussion

In this chapter, we have characterised IFNAR1 and IFNAR2 dynamics at the cell membrane in real-time using single-molecule TIRFM and nanopipette based local delivery technology. Our data showed that the addition of IFNβ delivered by nanopipette reduces the diffusion coefficient of the mobile fraction of both co-expressed IFNAR1 and IFNAR2, indicating ligand induced heterodimerisation, supporting the long standing literature of IFN signaling[118,121]. However, when IFNAR1 or IFNAR2 was expressed on its own, the addition of IFNβ did not reduce the diffusion coefficient or induce a loss of total receptors. In addition, although the number of tracked IFNAR1 co-expressed with IFNAR2 also showed a significant decrease upon IFNβ stimulation, the track number of co-expressed IFNAR2 did not change significantly after the addition of IFNβ. These observations differ from published literature, where the addition of IFNβ was shown to induce IFNAR2 independent signaling and ubiquitination of both receptors[124,125]. In these studies, human cell lines (HEK-293T and Hela cells) overexpressing homologous receptors were used while in our experiment we used the mouse embryonic fibroblasts with heterologous receptor type to ensure no interference from endogenous receptors and titrated IFNAR1 and IFNAR2 for 1:1 expression. Therefore, the difference between the previous literature and our results might be due to the cell type used, which may influence the kinetics of the exogenously expressed receptors. Furthermore, the fluorescence activated cell sorting (FACS) analysis techniques in these publications quantified surface IFNAR2 at one hour intervals post-stimulation to show modest downregulation in comparison to IFNAR1[124,125]. Our study observed receptor kinetics immediately after the delivery of IFNβ by nanopipette, nuclear translocation of the transcription factor, STAT1, occurs within 10 minutes of IFN stimulation[118], therefore, the absence of IFNAR2 membrane dynamics may also be due to the limited time frame of the observation. To confirm that the kinetics of our model reflects that of literature, future work should be carried out on human cell line and observing the presence of IFNAR2 at extended time points.

The co-localization analysis shows that there is pre-dimerization before IFNβ stimulation and the addition of IFNβ would reduce the coincidence of receptor co-localization. This controversial result did not support the dimerization of IFNAR1 and IFNAR2 upon IFNβ stimulation. But it contributes to the two population of receptors on the cell membrane where the pre-dimerized IFNAR1 and IFNAR2 had very low level diffusion coefficient. This can be explained by the over-expression of exogenous IFNAR with a receptor density of $\sim 2/\mu m^2$ for

cells expressing both subunits. This receptor density is above typical physiological receptor concentration range $(0.1-1/\mu m^2)$[118], indicating the possibility of surface overcrowding.

One of the novelties in our experiment is that the nanopipette was used to deposit IFNβ to MEFs to activate IFNAR1 and IFNAR2. In the previous studies of IFNAR signalling, the IFNβ was added into cell medium and all the cell in the sample dish were triggered at the same time. Since TIRF could only image one cell at a time, the cells imaged in different sequence would have different response times to IFNβ, which will introduce errors in the kinetics analysis. When using nanopipette, each cell will be freshly triggered and imaged without any dead time, making the IFNAR activation identical within each individual cell.

# Chapter 5

# Development of two-colour epi-illumination SPIM

This chapter describes the development of a novel single-objective light-sheet microscopy, which is called epi-illumination selective-plane illumination microscopy (eSPIM). Equipped with a Galvo scanning mirror, eSPIM allows rapid single-molecule imaging with light-sheet illumination. This microscope is compatible with imaging using common biological sample holders, e.g. multi-well plates. Core components and their functions in eSPIM are illustrated with a schematic diagram. This diagram also demonstrates the principle of eSPIM. The performance of eSPIM was assessed by three proof-of-concept experiments. These experiments were fixed cell membrane imaging, live-cell DNA imaging and tracking tau protein aggregates in live cells.

**Contribution**

Bing Li and Ziwei Zhang worked together to build and maintain the eSPIM. The cell samples were gifts from the Laue group in the Department of Biochemistry at the University of Cambridge.

## 5.1 Introduction of eSPIM

As mentioned in the introduction (chapter 1), conventional light-sheet fluorescence microscopy (LSFM) usually uses a two-objective-lens geometry to introduce the illuminating light section into the bio-sample. This either uses a perpendicular geometry or a vertical geometry with an AFM reflective tip and the two-objective LSFM requires special sample chambers and is not compatible with the use of multi-well plates. In order to address this issue, an alternative single-objective LSFM has been developed. Oblique-plane microscopy (OPM) is the most common type of single-objective LSFM. It generates a highly angled light sheet and a remote focus system composed of a second and tertiary objective lens which the latter is used to tilt and focus the imaging plane onto a camera (figure 5.1 (a)). Usually, the resolution and single-collection efficiency is low because the tertiary objective lens is not able to capture all emission signals focused by the second objective, which results in a low NA of the tertiary objective lens (figure 5.1 (a)). To solve this problem, Yang *et al.*[101] found that when light rays travel from a low to a high refractive index medium (from air to water for example), the light rays could be compressed and refracted by the tertiary objective lens. Therefore, Yang *et al.* designed the eSPIM. In eSPIM, a coverslip-walled immersion chamber is placed in front of the tertiary objective lens in order to capture more emission signal (figure 5.1 (b)). Since it is challenging to maintain the water immersion in the chamber, Millett-Sikking and York[103] optimised the chamber by making a glass-tipped tertiary objective (snouty lens), which further improves instrument performance (figure 5.1 (c)). We therefore built a two-colour eSPIM in our lab using a snouty lens as the tertiary objective.
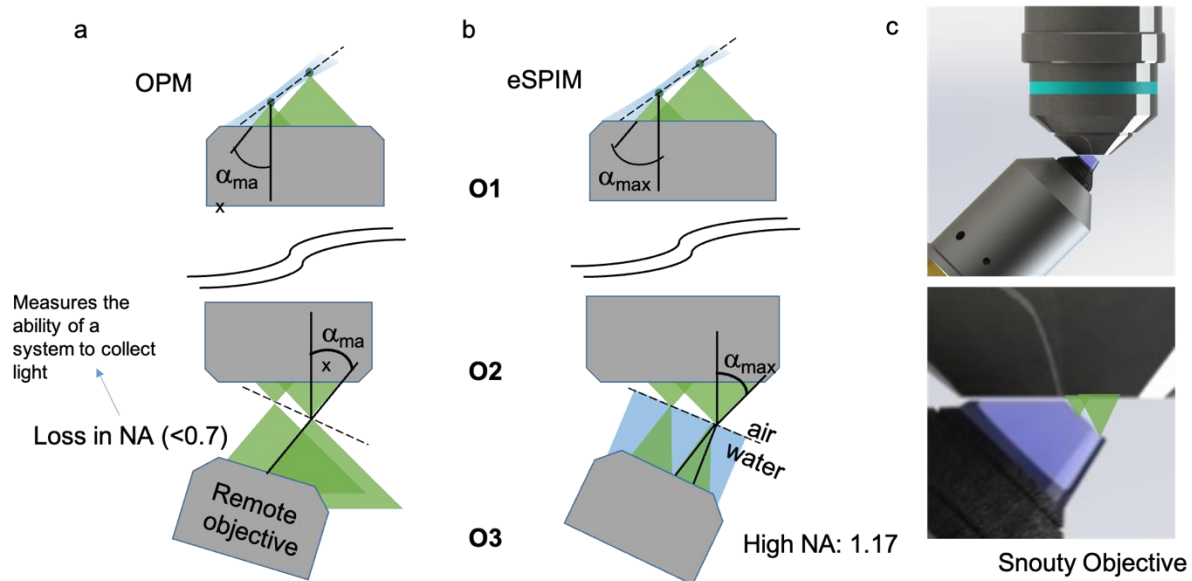
**Figure 5.1.** The principle of the remote image module. a) The typical remote tertiary objective lens of OPM. It misses parts of the tilted image and thus resulting in a low collection efficiency. b) The tertiary objective lens with a coverslip-walled immersion chamber to compress and refract the light was used in eSPIM. c) The geometry of the snouty lens.

**5.2 Building eSPIM**

Main components of the eSPIM are described in this section. The schematic optical pathway of the eSPIM is shown in schematic diagram (figure 5.2). Followed by the sequence of the components listed in the figure, the excitation and emission path are demonstrated. The supporting instruments are then described.

**5.2.1 The excitation path of eSPIM**

**The common illumination beam path**

As described in chapter 2, eSPIM and typical light-sheet microscope have similar components in the common-laser-beam path. These include the illumination light source, laser power controller, shutters, beam-expanders, positioning mirrors, multi-beam combiner and cylindrical lens.

**Dichroic beam splitter**

The dichroic mirror in eSPIM is installed after cylindrical lens. It not only splits the excitation beam and emission signals, but also tilts the light-sheet angle when it gets out of the primary lens to scan the bio-sample. The common tilt angle is 30°, but it can be tuned from 0° to 45°.

**Tube lens and scan lens**

Two pairs of tube lenses and scan lenses form two 4f systems to focus and re-collimate both the excitation laser beam and emission fluorescence. In the first combination, tube lens 1 and scan lens 2 are installed behind the primary objective lens. The distance between tube lens 1 and scan lens 1 is the sum of their focal length, which is 270 mm (200mm + 70mm). The second 4f system is implemented behind the Galvo mirror. The distance between tube lens 2 and scan lens 2 is 296 mm (226mm + 70mm).

**Galvo mirror**

The Galvo mirror which can rotate along one axis is used to achieve a rapid light-sheet scan at a speed of 100 frames per second. The mirror is mounted on a 1D rotation motor. When the mirror rotates, the position where the light sheet enters the primary objectives can be changed in one direction and this initiates the light sheet to scan across the sample.

**The primary objective (O1)**

In our design, a high NA 60x water-immersion objective lens is mounted on an inverted microscope body and works as primary objective (O1) to illuminate the fluorophores and collect the emission signals.

## 5.2.2 The emission path and the remote image module

When the emission fluorescence is collected by O1, it passes through the 4f systems and the Galvo mirror to reach the dichroic splitter. After that, a two-colour remote image module (RIM) is used to refocus the emission signal to camera. The RIM consists a 40x air objective lens (O2), a snouty lens (O3), a tube lens and a two-colour splitter. O2 generates a replica of the fluorescence collected from the primary objective at the focus of the tertiary objective lens, which is the snouty lens (O3). O3 is placed 30° relative O2 and is responsible for re-collimating and correcting the image using the same angle of light-sheet tilting. The tube lens and the image splitter are used to refocus the signal onto camera in two-colour channels.
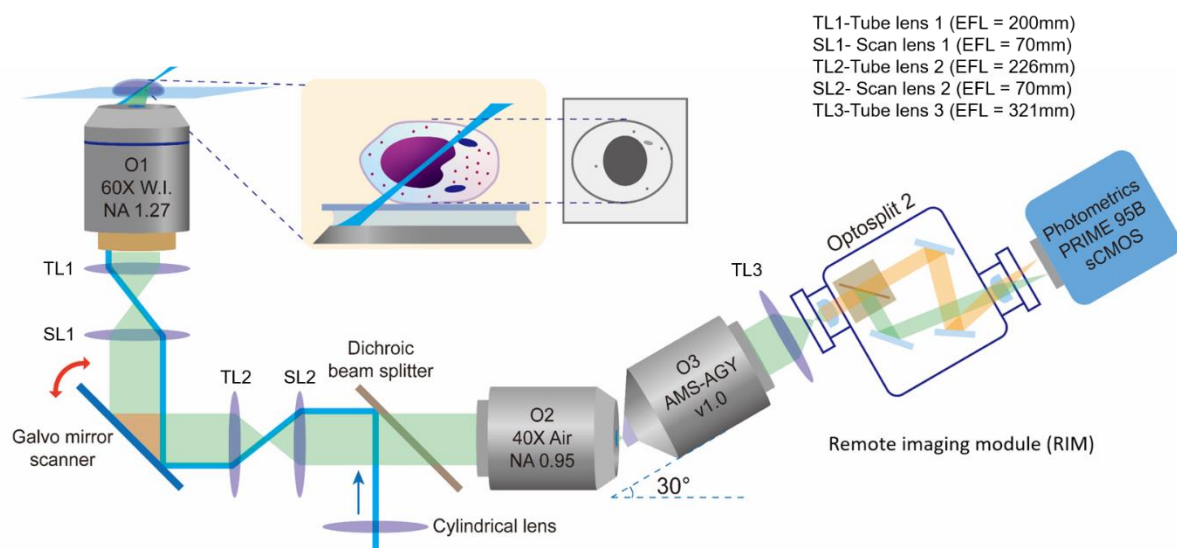


**Figure 5.2.** The illustration of eSPIM. The common-illumination-laser path is not shown in the figure. (Left) The excitation partconsists of two 4f systems, a Galvo mirror and the primary objective lens (O1). (Right) The remote imaging module (RIM) contains the secondary objective lens (O2), a snouty lens (O3), a two-colour splitter and a camera.

### 5.2.3 Supporting instruments

**Sample stage**

Biosamples are mounted on a XY stage which is designed to fit the 35-mm glass-bottom petri dish. The XY stage can be controlled by steppers. It can move across a distance of 20 cm with a smallest step as 1 μm.

**Optical table**

The entire set-up including all the laser lines, mirrors and microscope body is built on a vibration-insulation damping optical table. Typically, the damping optical table can isolate the the microscope from normal environment vibration including doors opening and closing and footsteps around the room.

**Live-cell incubating unit**

Live-cell incubating unit has two subunits, one is heaters plus a plastic incubator that covers the sample stage to maintain a constant 37 °C sample temperature and the other one is a carbon dioxide sensor plus carbon dioxide cylinder to keep introducing carbon dioxide into the incubator and maintain a 5% $CO_2$ atmosphere.

## 5.3 Bio-sample imaging using eSPIM

To demonstrate the performance of single or multi-colour eSPIM imaging, a variety of cells and their subcellular structures were imaged. These include fixed cell imaging, live-cell DNA imaging and *in vivo* tau aggregates imaging.

### 5.3.1 Fixed cell imaging

Firstly, fixed macrophages were labelled with membrane dye (Abberior STAR 488). In figure 5.3, the outline of macrophage was clearly illuminated by eSPIM using a 488-nm laser. Then, the TNF-$\alpha$ generated on the surface of macrophage upon LPS stimulation was imaged. In figure 5.4 (a), the macrophage membrane was labelled by Abberior STAR 488 and to mark the outline of the cells. The TNF-$\alpha$ stimulated by LPS labelled with Alexa-647 conjugated antibody is shown in figure 5.4 (b). The merged channel (Figure 5.4 (c)) shows that the TNF-$\alpha$ signal overlaps with the membrane, suggesting that the TNF-$\alpha$ is mainly generated on the cell surface.
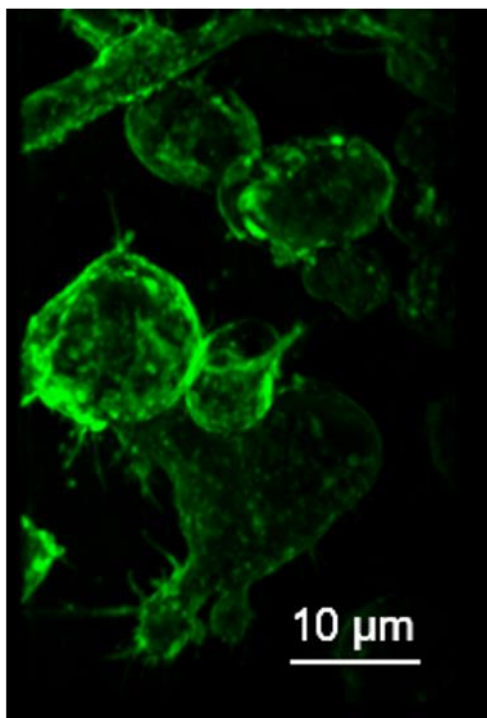


**Figure 5.3.** Fixed cells imaged by eSPIM. Macrophages surface was labelled with Abberior STAR 488 were excited by 488-nm laser. The scale bar is 10 μm.
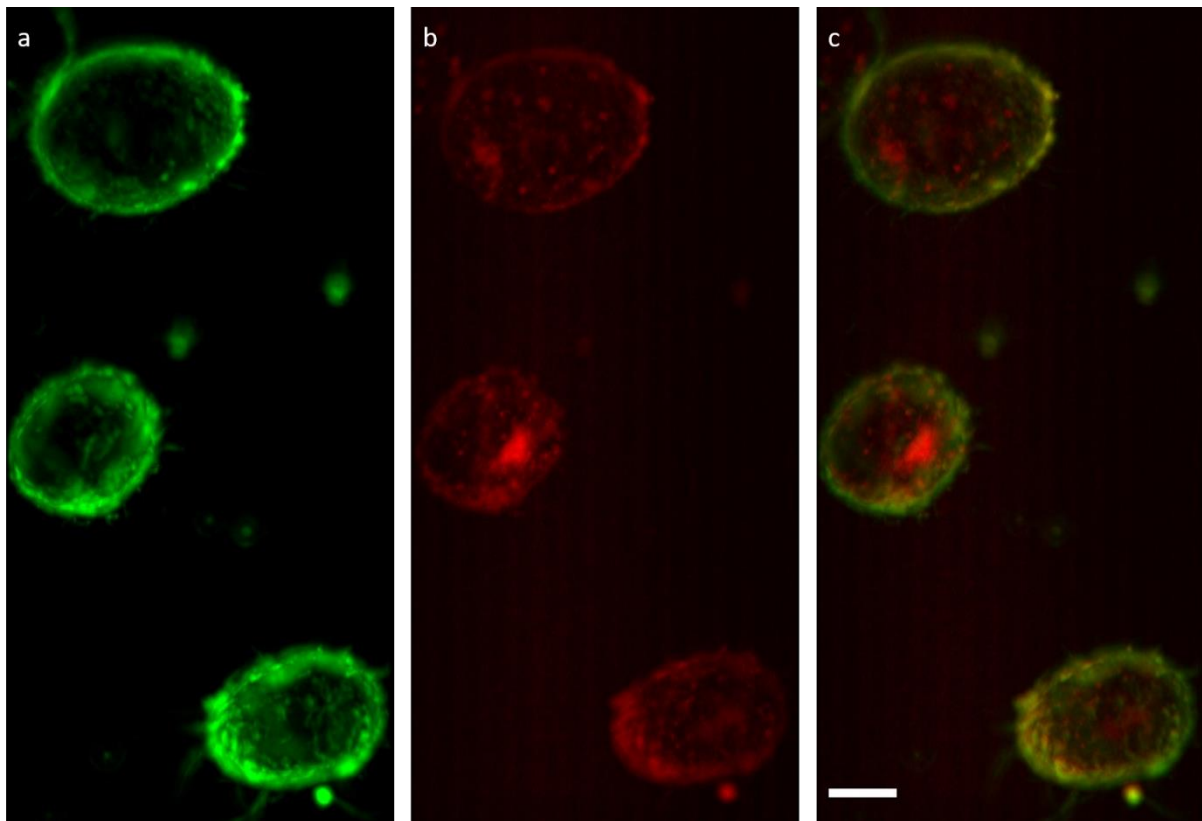
**Figure 5.4.** The TNF-α generation on macrophage surface after LPS stimulation. a) The macrophage was labelled with the membrane dye Abberior STAR 488 and excited by 488-nm laser. (Green) b) The TNF-α labelled with Alexa-647 conjugated antibody was excited by 635-nm laser. (Red) c) The overlay image of the green and red channel. It shows that the TNF-α signal is mainly distributed on the cell surface. The scale bar is 10 μm.

### 5.3.2 live-cell imaging

The nuclei of the live cells were labelled with Sir-DNA and was imaged by eSPIM for 3 hours (30ms exposure time and 90s interval) at a laser power density of 150 $W/cm^2$. From the montage as shown in figure 5.5, no noticeable photo-bleaching is observed. In contrast, the dyes in these live cells can be photo-bleached within two hours using conventional confocal microscope.
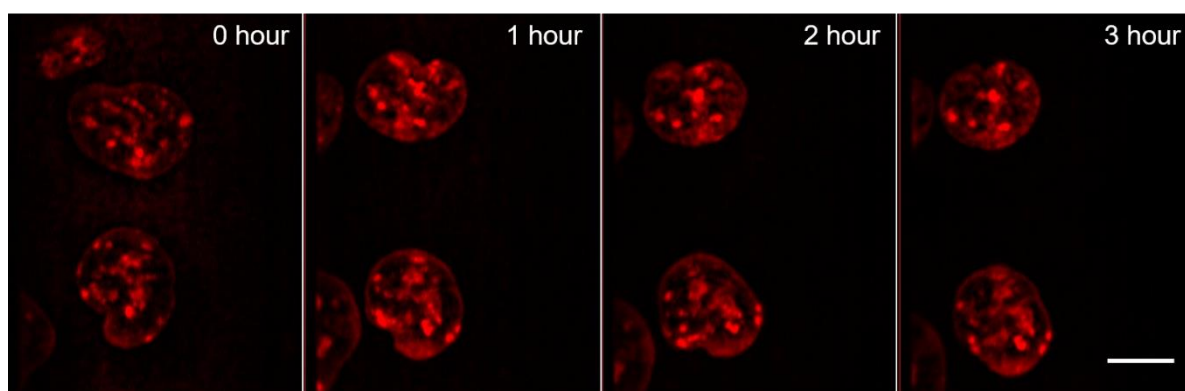


**Figure 5.5.** DNA image in live cells for 3 hours without noticeable photobleaching. The scale bar is 10 μm. All micrographs are of the same brightness and contrast.

### 5.3.3 Tau aggregates imaging in live cells

Tau-Venus expressed in HEK 293 cells were imaged using eSPIM. In figure 5.6, the tau puncta were continuously imaged for 10 mins with 30-ms exposure time. It is possible to track each tau aggregate for a long time with reduced photo-bleaching using eSPIM.
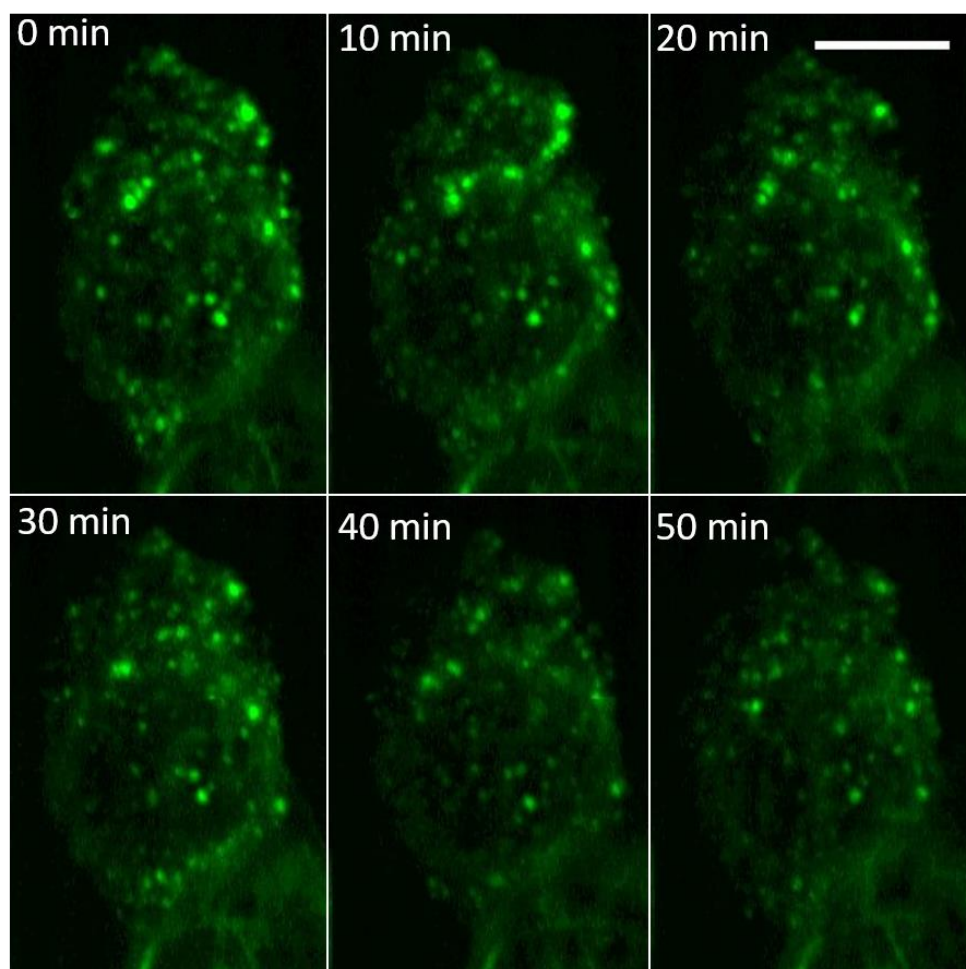
**Figure 5.6.** Tau aggregates imaged within live HEK 293 cells. The scale bar is 10 μm.

## 5.4 eSPIM alignment

To align the eSPIM, a collimated laser beam needs to be introduced into O1 from the top. In the remote image module, the O3 should be first adjusted to 0° relative to O2, forming a straight optical path (figure 5.7). Then one installs the other components listed in section 5.2 and precisely adjusts their position to get a perfect symmetric beam shape on the camera (figure 5.8).
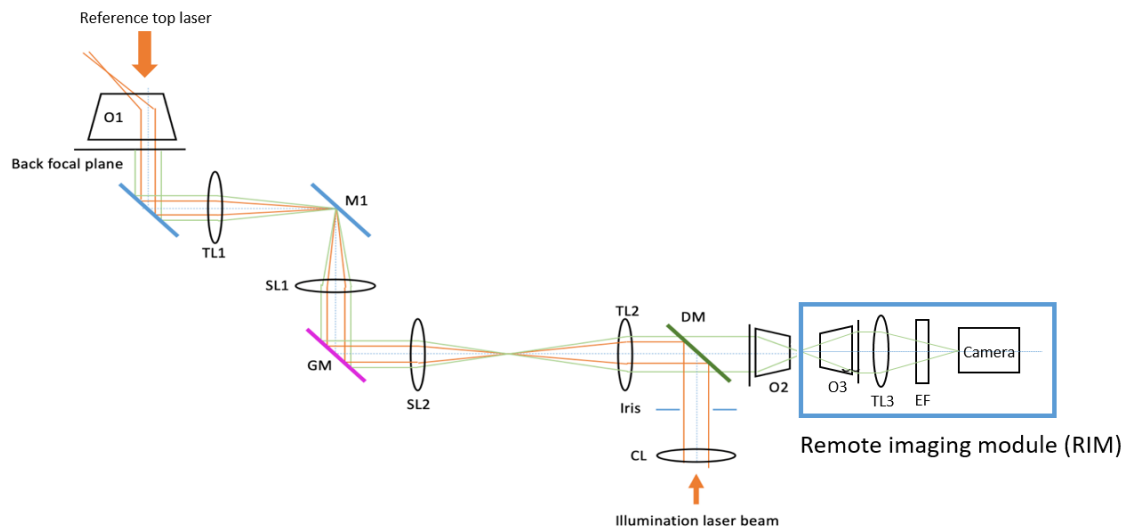


**Figure 5.7.** The straight beam path in remote image module (RIM). The O3 is 0° relative to O2. A reference collimated laser beam is introduce from the top of O1.
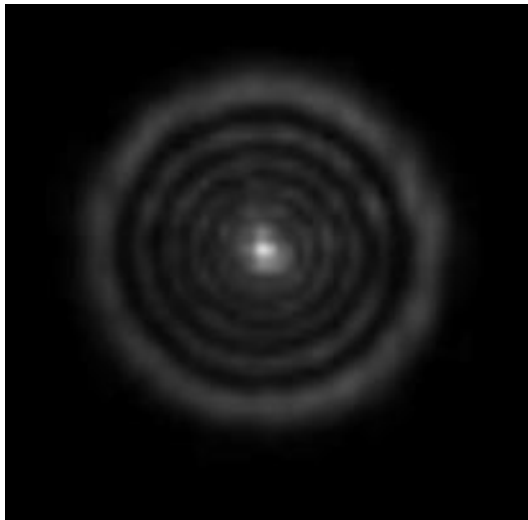


**Figure 5.8.** The symmetric beam generated by the straight MID on camera.

Once the symmetric beam is observed, the RIM is then tilted 30° relative to O2 (figure 5.9) and its position should be adjusted until the pattern of the beam shape on the camera is similar to the one in figure 5.10.
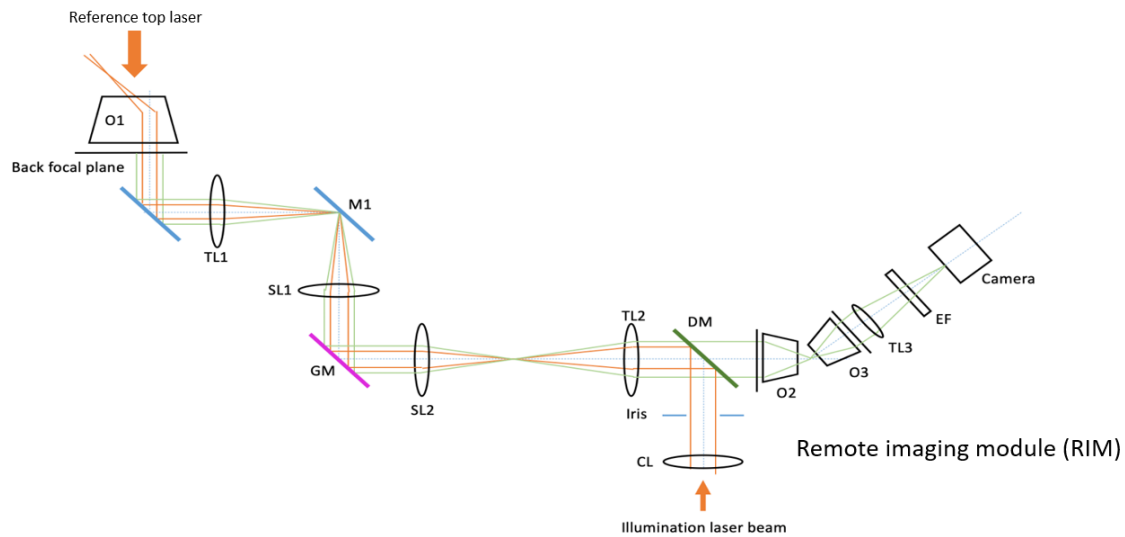


**Figure 5.9.** The RIM is tilted 30° relative to O2.



**Figure 5.10.** The tilted laser-beam shape.

Then the reference laser beam can be removed to introduce the light sheet into O1. The dichroic mirror should be adjusted to make the light sheet at an angle of 30° relative the coverslip. TetraSpeck beads in agarose gel can be used to monitor the alignment. If the light-sheet angle matches the RIM tilted angle, the beads should be visualised across the whole field of view when imaged by the eSPIM (figure 5.11).
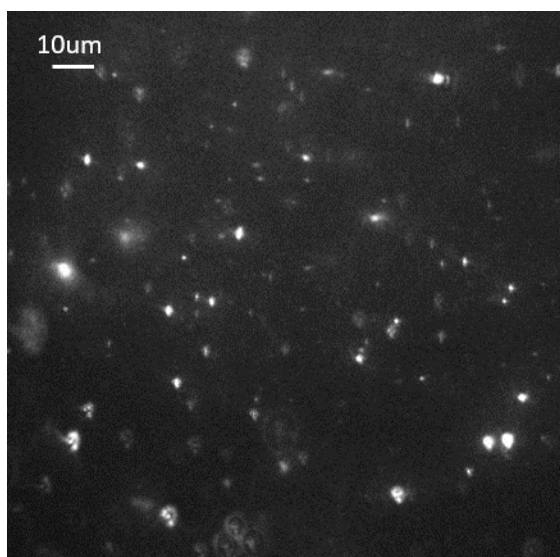
**Figure 5.11.** Beads imaged by 30° tilted light sheet.

## 5.5 Light-sheet thickness measurement

To measure the thickness of the light sheet generated by eSPIM, the sheet angle was first adjusted to 90° relative to the coverslip. Then a dye, Oxazine 725, was added on the coverslip surface and excited by 635-nm laser. The fluorescence image of the excited Oxazine 725 represents the shape of light sheet. By measuring the FWHM of the sheet weight (figure 5.12), the thickness was calculated as 1.029 μm.



**Figure 5.12.** The image of Oxazine 725 excited by the light sheet

## 5.6 Conclusion

In this chapter, a new design of single-objective light-sheet microscopy, which is called two-colour eSPIM, was described. The results show that the eSPIM is able to scan a range of bio-samples including both fixed and live samples rapidly with reduced photo-bleaching. Using a two-colour dichroic splitter, eSPIM is also capable of imaging two different dye-labelled species at the same time. In the future, the nanopipette based local delivery module can be installed on eSPIM. This can make the eSPIM more versatile for imaging cell inflammatory signalling and visualising cell-cell interactions.

# Conclusion

In this pilot study, we have designed and assembled two novel single molecule imaging methods. 1. the ldSPIM. By combining the single-objective light sheet microscopy and the nanopipette based delivery module, the ldSPIM is able to locally deliver precise amounts of target molecule down to the single molecule level to a specific position on the surface or inside the cell samples and image. Using an AFM cantilever to reflect the light sheet on top of the objective, ldSPIM is compatible with all kinds of sample dishes including normal petri dishes and multi-well plate. 2. the eSPIM. eSPIM is the next generation single objective light sheet microscopy. Using a galvo mirror scanned tilted light sheet and a remote imaging module, eSPIM is able to achieve rapid 3D scans. In addition, since eSPIM does not need further items such as AFM cantilever to reflect the light sheet, it is more effective to image cell samples in all kinds of sample dishes.

By applying the ldSPIM to study TLR4 signalling and Myddosome formation, we first proved that nanopipette delivered LPS and sonicated Aβ fibrils could both trigger TLR4 to form the downstream signalling complexes, Myddosomes. We then identified and compared the kinetics of LPS and sonicated Aβ fibrils triggered Myddosome assembly in the following five aspects: 1) the first time point when Myddosome formed, 2) the Myddosome lifetime, 3) the total number of oligomers formed within 30mins upon triggering, 4) the Myddosome size and 5) the variation of MyD88 oligomer size with stimulation time. The results showed that while the LPS-triggered Myddosomes formed faster, the Aβ-triggered Myddosomes had long lifetime and larger size. In terms of the total number of oligomers formed within 30mins upon triggering, there is no significant difference between two stimuli. These results suggests that sonicated Aβ fibrils triggers a different response of the Myddosome signalling compared with LPS, and this might be caused by the difference in size between LPS and sonicated Aβ fibrils.

Finally, collaborating with Dr. Stephanie Huang in Monash University, we demonstrated the application of nanopipette delivery in characterising the surface kinetics of the interaction between IFNβ and IFNAR. We observed the addition of IFNβ delivered by nanopipette reduces the diffusion coefficient of the mobile fraction of both co-expressed IFNAR1 and IFNAR2, indicating ligand induced heterodimerisation. We also observed the reduction of IFNAR1 number upon IFNβ indicating the internalization and degradation of the receptor. Several

factors such as cell type and receptor density on the cell surface may contribute to this result differing from previously published work

# Future work

In the next steps, there are several aspects that need further development. The first one is developing a Myd88-GFP cell line. Currently the macrophages express MyD8-GFP were produced by lentiviral transfection and transduction. From figure 3.10 to figure 3.18, we observed that the data distribution between each individual replicate varies significantly. This is because the virus transduction efficiency varies in each individual replicate, resulting in different amounts of Myd88-GFP expressed in each replicate and therefore different Myddosome intensities. The cells obtained using a Myd88-GFP cell line will have the same level of Myd88-GFP expression and generate stable response in each replicate, making the kinetics analysis much more accurate.

The second step is to develop a 3D Myddosome tracking algorithm. Currently the Myddosome kinetics is analysed by a 2D tracking algorithm. One drawback of this approach is that by projecting all Myddosomes in the cell volume into one frame, it is not possible to accurately determine the position and movement of puncta within the cell. By using 3D tracking, it can be further tested that whether the localisation of the Myddosome (membrane bound or cytoplasmic) affect their lifetime and stoichiometry, which could provide more information about MyD88 recruitment and disassembly.

The third step is to explore the link between Myddosome signalling intensity and downstream response, such as cytokines generation like TNF-$\alpha$ secretion. Currently we only characterized the difference of Myddosome assembly between LPS and sonicated A$\beta$ fibrils. However, the way how these kinetics difference will affect the downstream inflammatory response remains unknown. Since the cytokines release is a typical result of TLR4 mediated inflammatory response, we want to further test if different Myddosome size, lifetime and total number correlate with different levels of cytokines secretion.

# Reference

(1)    Jr, K. K.; Yasuda, R.; Noji, H.; Adachi, K. A Rotary Molecular Motor That Can Work at near 100 % Effeciency. *Phil.Trans. R. Soc. Lond. B* **2000**, *355*, 473–489.

(2)    Funatsu, T.; Harada, Y.; Tokunaga, M.; Saito, K.; Yanagida, T. Imaging of Single Fluorescent Molecules and Individual ATP Turnovers by Single Myosin Molecules in Aqueous Solution. *Nature* **1995**, *374* (6522), 555–559. https://doi.org/10.1038/374555a0.

(3)    Yang, W.; Gelles, J.; Musser, S. M. Imaging of Single-Molecule Translocation through Nuclear Pore Complexes. *Proc. Natl. Acad. Sci.* **2004**, *101* (35), 12887–12892. https://doi.org/10.1073/pnas.0403675101.

(4)    Weiss, S. Measuring Conformational Dynamics of Biomolecules by Single Molecule Fluorescence Spectroscopy. *Nat. Struct. Biol.* **2000**, *7* (9), 724–729. https://doi.org/10.1038/78941.

(5)    Kubitscheck, U.; Grünwald, D.; Hoekstra, A.; Rohleder, D.; Kues, T.; Siebrasse, J. P.; Peters, R. Nuclear Transport of Single Molecules: Dwell Times at the Nuclear Pore Complex. *J. Cell Biol.* **2005**, *168* (2), 233–243. https://doi.org/10.1083/jcb.200411005.

(6)    Sase, I.; Miyata, H.; Corrie, J. E.; Craik, J. S.; Kinosita, K. Real Time Imaging of Single Fluorophores on Moving Actin with an Epifluorescence Microscope. *Biophys. J.* **1995**, *69* (2), 323–328. https://doi.org/10.1016/S0006-3495(95)79937-4.

(7)    Tokunaga, M.; Kitamura, K.; Saito, K.; Iwane, A. H.; Yanagida, T. Single-Molecule Imaging of Fluorophores and Enzymatic Reactions Achieved by Total Internal-Reflection Fluorescence Miscroscopy. *Biochem. Biophys. Res. Commun.* **1997**, *235* (235), 47–53.

(8)    Yanagida, T. Mechanics and Models of the Myosin Motor. *Phil. Trans. R. Soc. Lond. B* **2000**, *355* (1396), 433–440. https://doi.org/10.1098/rstb.2000.0584.

(9)    Kues, T.; Peters, R.; Kubitscheck, U. Visualization and Tracking of Single Protein Molecules in the Cell Nucleus. *Biophys. J.* **2001**, *80* (6), 2954–2967. https://doi.org/10.1016/S0006-3495(01)76261-3.

(10)   Stelzer, E. H. K. Light Sheet Fluorescence Microscopy for Quantitative Biology. *Nat. Methods* **2015**, *12* (1), 23–26. https://doi.org/10.1038/nmeth.3219.

(11)   Baumgart, E.; Kubitscheck, U. Scanned Light Sheet Microscopy with Confocal Slit Detection. *Opt. Express* **2012**, *20* (19), 21805. https://doi.org/10.1364/OE.20.021805.

(12)     Axelrod, D. Cell-Substrate Contacts Illuminated by Total Internal Reflection Fluorescence. *J. Cell Biol.* **1981**, *89* (9), 141–145.

(13)     Dodt, H. U.; Leischner, U.; Schierloh, A.; Jährling, N.; Mauch, C. P.; Deininger, K.; Deussing, J. M.; Eder, M.; Zieglgänsberger, W.; Becker, K. Ultramicroscopy: Three-Dimensional Visualization of Neuronal Networks in the Whole Mouse Brain. *Nat. Methods* **2007**, *4* (4), 331–336. https://doi.org/10.1038/nmeth1036.

(14)     Huisken, J.; Stainier, D. Y. R. Even Fluorescence Excitation by Multidirectional Selective Plane Illumination Microscopy (MSPIM). *Opt. Lett.* **2007**, *32* (17), 2608. https://doi.org/10.1364/OL.32.002608.

(15)     Voie, A. H.; Burns, D. H.; Spelman, F. A. Orthogonal-Plane Fluorescence Optical Sectioning: Three Dimensional Imaging of Macroscopic Biological Specimens. *Journal of Microscopy*. 1993, pp 229–236. https://doi.org/10.1111/j.1365-2818.1993.tb03346.x.

(16)     Keller, P. J.; Stelzer, E. H. Quantitative in Vivo Imaging of Entire Embryos with Digital Scanned Laser Light Sheet Fluorescence Microscopy. *Current Opinion in Neurobiology*. 2008, pp 624–632. https://doi.org/10.1016/j.conb.2009.03.008.

(17)     Keller, P. J.; Schmidt, A. D.; Wittbrodt, J.; Stelzer, E. H. K. Supporting Online Material for Reconstruction of Zebrafish Early Light Sheet Microscopy. *Science* **2008**, *322* (November), 1065–1069. https://doi.org/10.1126/science.1162493.

(18)     Makio Tokunaga, Naoko Imamoto, & Kumiko Sakata-Sogawa. Highly Inclined Thin Illumination Enables Clear Single-Molecule Imaging in Cells. *Nat. Methods* **2010**, *5*, 159–161. https://doi.org/10.1038/NMETH.1171.

(19)     Huisken, J.; Swoger, J.; Del Bene, F.; Wittbrodt, J.; Stelzer, E. H. K. Optical Sectioning Deep inside Live Embryos by Selective Plane Illumination Microscopy. *Science (80-84. )*. **2004**, *305* (5686), 1007–1009. https://doi.org/10.1126/science.1100035.

(20)     Santi, P. A. Light Sheet Fluorescence Microscopy: A Review. *Journal of Histochemistry and Cytochemistry*. 2011, pp 129–138. https://doi.org/10.1369/0022155410394857.

(21)     Ponjavic, A.; McColl, J.; Carr, A. R.; Santos, A. M.; Kulenkampff, K.; Lippert, A.; Davis, S. J.; Klenerman, D.; Lee, S. F. Single-Molecule Light-Sheet Imaging of Suspended T Cells. *Biophys. J.* **2018**, *114* (9), 2200–2211. https://doi.org/10.1016/j.bpj.2018.02.044.

(22)     Greiss, F.; Deligiannaki, M.; Jung, C.; Gaul, U.; Braun, D. Single-Molecule Imaging in Living Drosophila Embryos with Reflected Light-Sheet Microscopy. *Biophys. J.* **2016**, *110* (4), 939–946. https://doi.org/10.1016/j.bpj.2015.12.035.

(23)     Manuscript, A. In Live Mammalian Cells. *Single Mol. Imaging Transcr. Factor Bind. to DNA Live Mamm. Cells* **2013**, *10* (5), 421–426. https://doi.org/10.1038/nmeth.2411.Single.

(24)     Kumar, S.; Wilding, D.; Sikkel, M. B.; Lyon, A. R.; MacLeod, K. T.; Dunsby, C. High-Speed 2D and 3D Fluorescence Microscopy of Cardiac Myocytes. *Opt. Express* **2011**, *19* (15), 13839. https://doi.org/10.1364/oe.19.013839.

(25)     Maioli, V.; Chennell, G.; Sparks, H.; Lana, T.; Kumar, S.; Carling, D.; Sardini, A.; Dunsby, C. Time-Lapse 3-D Measurements of a Glucose Biosensor in Multicellular Spheroids by Light Sheet Fluorescence Microscopy in Commercial 96-Well Plates. *Sci. Rep.* **2016**, *6* (November), 1–13. https://doi.org/10.1038/srep37777.

(26)     Zhukov, A.; Richards, O.; Ostanin, V.; Korchev, Y.; Klenerman, D. Ultramicroscopy A Hybrid Scanning Mode for Fast Scanning Ion Conductance Microscopy ( SICM ) Imaging. *Ultramicroscopy* **2012**, *121*, 1–7. https://doi.org/10.1016/j.ultramic.2012.06.015.

(27)     Bruckbauer, A.; Ying, L.; Rothery, A. M.; Zhou, D.; Shevchuk, A. I.; Abell, C.; Korchev, Y. E.; Klenerman, D. Writing with DNA and Protein Using a Nanopipet for Controlled Delivery. *J. Am. Chem. Soc.* **2002**, *124* (30), 8810–8811. https://doi.org/10.1021/ja026816c.

(28)     Ying, L.; Bruckbauer, A.; Rothery, A. M.; Korchev, Y. E.; Klenerman, D. Programmable Delivery of DNA through a Nanopipet. *Anal. Chem.* **2002**, *74* (6), 1380–1385. https://doi.org/10.1021/ac015674m.

(29)     Bruckbauer, A.; Zhou, D.; Ying, L.; Korchev, Y. E.; Abell, C.; Klenerman, D. Multicomponent Submicron Features of Biomolecules Created by Voltage Controlled Deposition from a Nanopipet. *J. Am. Chem. Soc.* **2003**, *125* (32), 9834–9839. https://doi.org/10.1021/ja035755v.

(30)     Klenerman, D.; Shevchuk, A.; Novak, P.; Korchev, Y. E.; Davis, S. J. Imaging the Cell Surface and Its Organization down to the Level of Single Molecules. *Philosophical Transactions of the Royal Society B: Biological Sciences*. 2013. https://doi.org/10.1098/rstb.2012.0027.

(31)     Bruckbauer, A.; James, P.; Zhou, D.; Ji, W. Y.; Excell, D.; Korchev, Y.; Jones, R.;

Klenerman, D. Nanopipette Delivery of Individual Molecules to Cellular Compartments for Single-Molecule Fluorescence Tracking. *Biophys. J.* **2007**, *93* (9), 3120–3131. https://doi.org/10.1529/biophysj.107.104737.

(32)  Lalley. Microiontophoresis and Pressure Ejection. *Mod. Tech. Neurosci. Res.* **1999**, 193–212. https://doi.org/10.1016/0197-0186(86)90175-0.

(33)  Bagher, P.; Davis, M. J.; Segal, S. S. Visualizing Calcium Responses to Acetylcholine Convection along Endothelium of Arteriolar Networks in Cx40BAC-GCaMP2 Transgenic Mice. *Am. J. Physiol. Heart Circ. Physiol.* **2011**, *301* (3), H794-802. https://doi.org/10.1152/ajpheart.00425.2011.

(34)  Kovács, P.; Dénes, V.; Kellényi, L.; Hernádi, I. Microiontophoresis Electrode Location by Neurohistological Marking: Comparison of Four Native Dyes Applied from Current Balancing Electrode Channels. *J. Pharmacol. Toxicol. Methods* **2005**, *51* (2), 147–151. https://doi.org/10.1016/j.vascn.2004.08.002.

(35)  Rodolfa, K. T.; Bruckbauer, A.; Zhou, D.; Korchev, Y. E.; Klenerman, D. Two-Component Graded Deposition of Biomolecules with a Double-Barreled Nanopipette. *Angew. Chemie - Int. Ed.* **2005**, *44* (42), 6854–6859. https://doi.org/10.1002/anie.200502338.

(36)  Piper, J. D.; Li, C.; Lo, C.; Berry, R.; Korchev, Y.; Ying, L.; Klenerman, D. Characterization and Application of Controllable Local Nanopipet. *J. AM. CHEM. SOC* **2008**, *130* (9), 10386–10393.

(37)  Bruckbauer, A.; Zhou, D.; Kang, D. J.; Korchev, Y. E.; Abell, C.; Klenerman, D. An Addressable Antibody Nanoarray Produced on a Nanostructured Surface. *J. Am. Chem. Soc.* **2004**, *126* (21), 6508–6509. https://doi.org/10.1021/ja0317426.

(38)  Adam Seger, R.; Actis, P.; Penfold, C.; Maalouf, M.; Vilozny, B.; Pourmand, N. Voltage Controlled Nano-Injection System for Single-Cell Surgery. *Nanoscale* **2012**, *4* (19), 5843–5846. https://doi.org/10.1039/c2nr31700a.

(39)  Babakinejad, B.; Jönsson, P.; López Córdoba, A.; Actis, P.; Novak, P.; Takahashi, Y.; Shevchuk, A.; Anand, U.; Anand, P.; Drews, A.; Ferrer-Montiel, A.; Klenerman, D.; Korchev, Y. E. Local Delivery of Molecules from a Nanopipette for Quantitative Receptor Mapping on Live Cells. *Anal. Chem.* **2013**, *85* (19), 9333–9342. https://doi.org/10.1021/ac4021769.

(40)  Ivanov, A. P.; Actis, P.; Jönsson, P.; Klenerman, D.; Korchev, Y.; Edel, J. B. On-Demand Delivery of Single DNA Molecules Using Nanopipets. *ACS Nano* **2015**, *9* (4),

3587–3594. https://doi.org/10.1021/acsnano.5b00911.

(41)     Laforge, F. O.; Carpino, J.; Rotenberg, S. A.; Mirkin, M. V. Electrochemical
        Attosyringe. *Proc. Natl. Acad. Sci.* **2007**, *104* (29), 11895–11900.
        https://doi.org/10.1073/pnas.0705102104.

(42)     Matsuoka, H.; Komazaki, T.; Mukai, Y.; Shibusawa, M.; Akane, H.; Chaki, A.;
        Uetake, N.; Saito, M. High Throughput Easy Microinjection with a Single-Cell
        Manipulation Supporting Robot. *J. Biotechnol.* **2005**, *116* (2), 185–194.
        https://doi.org/10.1016/j.jbiotec.2004.10.010.

(43)     Barber, K.; Mala, R. R.; Lambert, M. P.; Qiu, R.; MacDonald, R. C.; Klein, W. L.
        Delivery of Membrane-Impermeant Fluorescent Probes into Living Neural Cell
        Populations by Lipotransfer. *Neurosci. Lett.* **1996**, *207* (1), 17–20.
        https://doi.org/10.1016/0304-3940(96)12497-6.

(44)     Zelphati, O.; Wang, Y.; Kitada, S.; Reed, J. C.; Felgner, P. L.; Corbeil, J. Intracellular
        Delivery of Proteins with a New Lipid-Mediated Delivery System. *J. Biol. Chem.*
        **2001**, *276* (37), 35103–35110. https://doi.org/10.1074/jbc.M104920200.

(45)     Provoda, C. J.; Stier, E. M.; Lee, K. D. Tumor Cell Killing Enabled by Listeriolysin O-
        Liposome-Mediated Delivery of the Protein Toxin Gelonin. *J. Biol. Chem.* **2003**, *278*
        (37), 35102–35108. https://doi.org/10.1074/jbc.M305411200.

(46)     Yacoub, M. D. The κ-μ Distribution and the η-μ Distribution. *IEEE Antennas Propag.
        Mag.* **2007**, *49* (1), 68–81. https://doi.org/10.1109/MAP.2007.370983.

(47)     Zhou, H.; Wu, S.; Joo, J. Y.; Zhu, S.; Han, D. W.; Lin, T.; Trauger, S.; Bien, G.; Yao,
        S.; Zhu, Y.; Siuzdak, G.; Schöler, H. R.; Duan, L.; Ding, S. Generation of Induced
        Pluripotent Stem Cells Using Recombinant Proteins
        (DOI:10.1016/j.Stem.2009.04.005). *Cell Stem Cell* **2009**, *4* (6), 581.
        https://doi.org/10.1016/j.stem.2009.05.014.

(48)     Shah, D. A.; Kwon, S. J.; Bale, S. S.; Banerjee, A.; Dordick, J. S.; Kane, R. S.
        Regulation of Stem Cell Signaling by Nanoparticle-Mediated Intracellular Protein
        Delivery. *Biomaterials* **2011**, *32* (12), 3210–3219.
        https://doi.org/10.1016/j.biomaterials.2010.11.077.

(49)     Zhang, Y.; Yu, L. C. Microinjection as a Tool of Mechanical Delivery. *Curr. Opin.
        Biotechnol.* **2008**, *19* (5), 506–510. https://doi.org/10.1016/j.copbio.2008.07.005.

(50)     Viigipuu, K.; Kallio, P. Microinjection of Living Adherent Cells by Using a Semi-
        Automatic Microinjection System. In *ATLA Alternatives to Laboratory Animals*; 2004;

Vol. 32, pp 417–423.

(51) Prasanna, G. L.; Panda, T. Electroporation: Basic Principles, Practical Considerations and Applications in Molecular Biology. *Bioprocess Eng.* **1997**, *16* (5), 261–264. https://doi.org/10.1007/s004490050319.

(52) Ionescu-Zanetti, C.; Blatz, A.; Khine, M. Electrophoresis-Assisted Single-Cell Electroporation for Efficient Intracellular Delivery. *Biomed. Microdevices* **2008**, *10* (1), 113–116. https://doi.org/10.1007/s10544-007-9115-x.

(53) Rols, M.; Golzio, M.; Teissie, J. Direct Visualization at the Single-Cell Level of Electrically Mediated Gene Delivery. *Proc. Natl. Acad. Sci.* **2002**, *99* (3), 1292–1297.

(54) Yan, M.; Du, J.; Gu, Z.; Liang, M.; Hu, Y.; Zhang, W.; Priceman, S.; Wu, L.; Zhou, Z. H.; Liu, Z.; Segura, T.; Tang, Y.; Lu, Y. A Novel Intracellular Protein Delivery Platform Based on Single-Protein Nanocapsules. *Nat. Nanotechnol.* **2010**, *5* (1), 48–53. https://doi.org/10.1038/nnano.2009.341.

(55) Kam, N. W. S.; Jessop, T. C.; Wender, P. A.; Dai, H. Nanotube Molecular Transporters: Internalization of Carbon Nanotube-Protein Conjugates into Mammalian Cells. *J. Am. Chem. Soc.* **2004**, *126* (22), 6850–6851. https://doi.org/10.1021/ja0486059.

(56) Prechtel, A. T.; Turza, N. M.; Theodoridis, A. A.; Kummer, M.; Steinkasserer, A. Small Interfering RNA (SiRNA) Delivery into Monocyte-Derived Dendritic Cells by Electroporation. *J. Immunol. Methods* **2006**, *311* (1–2), 139–152. https://doi.org/10.1016/j.jim.2006.01.021.

(57) Prentice, H. L.; Prentice, H. L. High Efficiency Transformation of Schizosaccharomyces Pombe by Electroporation. *Nucleic Acids Res.* **2008**, *20* (3), 621. https://doi.org/10.1093/nar/20.3.621.

(58) Yun, C. K.; Hwang, J. W.; Kwak, T. J.; Chang, W. J.; Ha, S.; Han, K.; Lee, S.; Choi, Y. S. Nanoinjection System for Precise Direct Delivery of Biomolecules into Single Cells. *Lab Chip* **2019**, *19* (4), 580–588. https://doi.org/10.1039/c8lc00709h.

(59) Delehanty, J. B.; Bradburne, C. E.; Boeneman, K.; Susumu, K.; Farrell, D.; Mei, B. C.; Blanco-Canosa, J. B.; Dawson, G.; Dawson, P. E.; Mattoussi, H.; Medintz, I. L. Delivering Quantum Dot-Peptide Bioconjugates to the Cellular Cytosol: Escaping from the Endolysosomal System. *Integr. Biol.* **2010**, *2* (5–6), 265–277. https://doi.org/10.1039/c0ib00002g.

(60) Hennig, S.; Van De Linde, S.; Lummer, M.; Simonis, M.; Huser, T.; Sauer, M. Instant

Live-Cell Super-Resolution Imaging of Cellular Structures by Nanoinjection of Fluorescent Probes. *Nano Lett.* **2015**, *15* (2), 1374–1381. https://doi.org/10.1021/nl504660t.

(61)     Blennow, K.; de Leon, M. J.; Zetterberg, H. Alzheimer's Disease. *Lancet* **2006**, *368* (9533), 387–403. https://doi.org/10.1016/S0140-6736(06)69113-7.

(62)     Prince, M.; Jackson, J. World Alzheimer Report 2009. *Alzheimer's Dis. Int.* **2009**, 1–96.

(63)     Cutler, R. G.; Kelly, J.; Storie, K.; Pedersen, W. A.; Tammara, A.; Hatanpaa, K.; Troncoso, J. C.; Mattson, M. P. Involvement of Oxidative Stress-Induced Abnormalities in Ceramide and Cholesterol Metabolism in Brain Aging and Alzheimer's Disease. *Proc. Natl. Acad. Sci. U. S. A.* **2004**, *101* (7), 2070–2075. https://doi.org/10.1073/pnas.0305799101.

(64)     Praticò, D.; Trojanowski, J. Q. Inflammatory Hypotheses: Novel Mechanisms of Alzheimer's Neurodegeneration and New Therapeutic Targets? *Neurobiol. Aging* **2000**, *21* (3), 441–445. https://doi.org/10.1016/S0197-4580(00)00141-X.

(65)     Neuner, S. M.; Tcw, J.; Goate, A. M. Neurobiology of Disease Genetic Architecture of Alzheimer ' s Disease. *Neurobiol. Dis.* **2020**, *143* (May), 104976.

(66)     Jucker, Mathias; Walker, L. C. Amyloid-β Pathology Induced in Humans Cause Freezing in Clouds. *Nature* **2015**, 3–4.

(67)     McGowan, E.; Pickford, F.; Kim, J.; Onstead, L.; Eriksen, J.; Yu, C.; Skipper, L.; Murphy, M. P.; Beard, J.; Das, P.; Jansen, K.; Delucia, M.; Lin, W.; Dolios, G.; Wang, R.; Eckman, C. B.; Dickson, D. W.; Hutton, M.; Hardy, J.; Golde, T. McGowan et Al., 2005 NIH Aβ42 Is Essential for Parenchymal and Vascular Amyloid Deposition in Mice.Pdf. *Neuron* **2006**, *47* (2), 191–199.

(68)     Bertram, L.; Tanzi, R. E. Thirty Years of Alzheimer's Disease Genetics: The Implications of Systematic Meta-Analyses. *Nat. Rev. Neurosci.* **2008**, *9* (10), 768–778. https://doi.org/10.1038/nrn2494.

(69)     Wu, L. G.; Saggau, P. Presynaptic Inhibition of Elicited Neurotransmitter Release. *Trends Neurosci.* **1997**, *20* (5), 204–212. https://doi.org/10.1016/S0166-2236(96)01015-6.

(70)     Sennvik, K.; Fastbom, J.; Blomberg, M.; Wahlund, L. O.; Winblad, B.; Benedikz, E. Levels of α- and β-Secretase Cleaved Amyloid Precursor Protein in the Cerebrospinal Fluid of Alzheimer's Disease Patients. *Neurosci. Lett.* **2000**, *278* (3), 169–172.

https://doi.org/10.1016/S0304-3940(99)00929-5.

(71) Puzzo, D.; Privitera, L.; Leznik, E.; Fà, M.; Staniszewski, A.; Palmeri, A.; Arancio, O. Picomolar Amyloid-β Positively Modulates Synaptic Plasticity and Memory in Hippocampus. *J. Neurosci.* **2008**, *28* (53), 14537–14545. https://doi.org/10.1523/JNEUROSCI.2692-08.2008.

(72) Velliquette, R. A.; O'Connor, T.; Vassar, R. Energy Inhibition Elevates β-Secretase Levels and Activity and Is Potentially Amyloidogenic in APP Transgenic Mice: Possible Early Events in Alzheimer's Disease Pathogenesis. *J. Neurosci.* **2005**, *25* (47), 10874–10883. https://doi.org/10.1523/JNEUROSCI.2350-05.2005.

(73) Akira, S.; Takeda, K. Toll-like Receptor Signalling. *Nature Reviews Immunology*. 2004, pp 499–511. https://doi.org/10.1038/nri1391.

(74) Janeway, C. A.; Medzhitov, R. Innate Mmune Ecognition. **2002**, No. 2, 197–216. https://doi.org/10.1146/annurev.immunol.20.083001.084359.

(75) Gay, N. J. Role of Self-Organising Myddosome Oligomers in Inflammatory Signalling by Toll-like Receptors. *BMC Biol.* **2019**, *17* (1), 15–18. https://doi.org/10.1186/s12915-019-0637-5.

(76) Ve, T.; Vajjhala, P. R.; Hedger, A.; Croll, T.; Dimaio, F.; Horsefield, S.; Yu, X.; Lavrencic, P.; Hassan, Z.; Morgan, G. P.; Mansell, A.; Mobli, M.; O'Carroll, A.; Chauvin, B.; Gambin, Y.; Sierecki, E.; Landsberg, M. J.; Stacey, K. J.; Egelman, E. H.; Kobe, B. Structural Basis of TIR-Domain-Assembly Formation in MAL- and MyD88-Dependent TLR4 Signaling. *Nat. Struct. Mol. Biol.* **2017**, *24* (9), 743–751. https://doi.org/10.1038/nsmb.3444.

(77) Akira, S.; Uematsu, S.; Takeuchi, O. Pathogen Recognition and Innate Immunity. *Cell*. 2006, pp 783–801. https://doi.org/10.1016/j.cell.2006.02.015.

(78) Gay, N. J.; Motshwene, P. G.; Sandercock, A. M.; Robinson, C. V; Grossmann, J. G.; Kao, C.; Latz, E.; Ayaluru, M.; Moncrieffe, M. C. An Oligomeric Signaling Platform Formed by the Toll-like Receptor Signal Transducers MyD88 and IRAK-4. *J. Biol. Chem.* **2009**, *284* (37), 25404–25411. https://doi.org/10.1074/jbc.m109.022392.

(79) Bonham, K. S.; Orzalli, M. H.; Hayashi, K.; Wolf, A. I.; Glanemann, C.; Weninger, W.; Iwasaki, A.; Knipe, D. M.; Kagan, J. C. A Promiscuous Lipid-Binding Protein Diversifies the Subcellular Sites of Toll-like Receptor Signal Transduction. *Cell* **2014**, *156* (4), 705–716. https://doi.org/10.1016/j.cell.2014.01.019.

(80) Medzhitov, R. Recognition of Microorganisms and Activation of the Immune

Response. *Nature* **2007**, *449* (7164), 819–826. https://doi.org/10.1038/nature06246.

(81)  Yuk, J. M.; Jo, E. K. Toll-like Receptors and Innate Immunity. *Journal of Bacteriology and Virology*. Elsevier Inc. 2011, pp 225–235. https://doi.org/10.4167/jbv.2011.41.4.225.

(82)  Beutler, B. A. TLRs and Innate Immunity. *Blood*. 2009, pp 1399–1407. https://doi.org/10.1182/blood-2008-07-019307.

(83)  Lin, S. C.; Lo, Y. C.; Wu, H. Helical Assembly in the MyD88-IRAK4-IRAK2 Complex in TLR/IL-1R Signalling. *Nature* **2010**, *465* (7300), 885–890. https://doi.org/10.1038/nature09121.

(84)  Latty, S.; Sakai, J.; Hopkins, L.; Verstak, B.; Paramo, T.; Berglund, N. A.; Gay, N. J.; Bond, P. J.; Klenerman, D.; Bryant, C. E. Activation of Toll-like Receptors Nucleates Assembly of the MyDDosome Signaling Hub. *Elife* **2018**, *7*, 1–16. https://doi.org/10.7554/eLife.31377.

(85)  Biphenyls, C. P. HHS Public Access. *Nat Rev Immunol* **2015**, *91* (2), 165–171. https://doi.org/10.1016/j.chemosphere.2012.12.037.Reactivity.

(86)  Gay, N. J.; Symmons, M. F.; Gangloff, M.; Bryant, C. E. Assembly and Localization of Toll-like Receptor Signalling Complexes. *Nature Reviews Immunology*. Nature Publishing Group 2014, pp 546–558. https://doi.org/10.1038/nri3713.

(87)  Kagan, J. C.; Magupalli, V. G.; Wu, H. SMOCs: Supramolecular Organizing Centres That Control Innate Immunity. *Nature Reviews Immunology*. Nature Publishing Group 2014, pp 821–826. https://doi.org/10.1038/nri3757.

(88)  Moncrieffe, M. C.; Bollschweiler, D.; Li, B.; Penczek, P. A.; Hopkins, L.; Bryant, C. E.; Klenerman, D.; Gay, N. J. MyD88 Death-Domain Oligomerization Determines Myddosome Architecture: Implications for Toll-like Receptor Signaling. *Structure* **2020**, *28* (3), 281-289.e3. https://doi.org/10.1016/j.str.2020.01.003.

(89)  Balka, K. R.; De Nardo, D. Understanding Early TLR Signaling through the Myddosome. *J. Leukoc. Biol.* **2019**, *105* (2), 339–351. https://doi.org/10.1002/JLB.MR0318-096R.

(90)  Heppner, F. L.; Ransohoff, R. M.; Becher, B. Immune Attack: The Role of Inflammation in Alzheimer Disease. *Nat. Rev. Neurosci.* **2015**, *16* (6), 358–372. https://doi.org/10.1038/nrn3880.

(91)  Working, N.; Haruhiko, G.; Barger, S.; Barnum, S.; Bradt, B.; Bauer, J.; Cole, G. M.; Cooper, N. R.; Eikelenboom, P.; Emmerling, M.; Fiebich, B. L.; Finch, C. E.;

Frautschy, S.; Griffin, W. S. T.; Hampel, H.; Hull, M.; Landreth, G.; Lue, L. F.; Mrak, R.; Mackenzie, I. R.; Mcgeer, P. L.; Banion, M. K. O.; Pachter, J.; Pasinetti, G.; Salaman, C. P.; Rogers, J.; Rydel, R.; Shen, Y.; Streit, W.; Strohmeyer, R.; Tooyoma, I.; Muiswinkel, F. L. Van; Veerhuis, R.; Walker, D.; Webster, S.; Wegrzyniak, B.; Wenk, G.; Coray, T. W. *Inflammation and Alzheimer ' s Disease*; 2000; Vol. 21.

(92)   Heneka, M. T.; Golenbock, D. T.; Latz, E. Innate Immunity in Alzheimer's Disease. *Nat. Immunol.* **2015**, *16* (3), 229–236. https://doi.org/10.1038/ni.3102.

(93)   Holmes, C. Inflammation in Alzheimer's Disease. *Dementia, Fifth Ed.* **2017**, *14* (April), 508–518. https://doi.org/10.1201/9781315381572.

(94)   Tuppo, E. E.; Arias, H. R. The Role of Inflammation in Alzheimer's Disease. *Int. J. Biochem. Cell Biol.* **2005**, *37* (2), 289–305. https://doi.org/10.1016/j.biocel.2004.07.009.

(95)   Ponjavic, A.; Ye, Y.; Laue, E.; Lee, S. F.; Klenerman, D. Sensitive Light-Sheet Microscopy in Multiwell Plates Using an AFM Cantilever. *Biomed. Opt. Express* **2018**, *9* (12), 5863. https://doi.org/10.1364/boe.9.005863.

(96)   Babakinejad, B.; Jönsson, P.; López Córdoba, A.; Actis, P.; Novak, P.; Takahashi, Y.; Shevchuk, A.; Anand, U.; Anand, P.; Drews, A.; Ferrer-Montiel, A.; Klenerman, D.; Korchev, Y. E. Local Delivery of Molecules from a Nanopipette for Quantitative Receptor Mapping on Live Cells. *Anal. Chem.* **2013**, *85* (19), 9333–9342. https://doi.org/10.1021/ac4021769.

(97)   Shevchuk, A.; Tokar, S.; Gopal, S.; Sanchez-Alonso, J. L.; Tarasov, A. I.; Vélez-Ortega, A. C.; Chiappini, C.; Rorsman, P.; Stevens, M. M.; Gorelik, J.; Frolenkov, G. I.; Klenerman, D.; Korchev, Y. E. Angular Approach Scanning Ion Conductance Microscopy. *Biophys. J.* **2016**, *110* (10), 2252–2265. https://doi.org/10.1016/j.bpj.2016.04.017.

(98)   Iljina, M.; Hong, L.; Horrocks, M. H.; Ludtmann, M. H.; Choi, M. L.; Hughes, C. D.; Ruggeri, F. S.; Guilliams, T.; Buell, A. K.; Lee, J. E.; Gandhi, S.; Lee, S. F.; Bryant, C. E.; Vendruscolo, M.; Knowles, T. P. J.; Dobson, C. M.; De Genst, E.; Klenerman, D. Nanobodies Raised against Monomeric α-Synuclein Inhibit Fibril Formation and Destabilize Toxic Oligomeric Species. *BMC Biol.* **2017**, *15* (1), 1–14. https://doi.org/10.1186/s12915-017-0390-6.

(99)   Iljina, M.; Tosatto, L.; Choi, M. L.; Sang, J. C.; Ye, Y.; Hughes, C. D.; Bryant, C. E.; Gandhi, S.; Klenerman, D. Arachidonic Acid Mediates the Formation of Abundant

Alpha-Helical Multimers of Alpha-Synuclein. *Sci. Rep.* **2016**, *6* (May), 1–14. https://doi.org/10.1038/srep33928.

(100) Cremades, N.; Cohen, S. I. A.; Deas, E.; Abramov, A. Y.; Chen, A. Y.; Orte, A.; Sandal, M.; Clarke, R. W.; Dunne, P.; Aprile, F. A.; Bertoncini, C. W.; Wood, N. W.; Knowles, T. P. J.; Dobson, C. M.; Klenerman, D. Direct Observation of the Interconversion of Normal and Toxic Forms of a -Synuclein. *Cell* **2012**, *149* (5), 1048–1059. https://doi.org/10.1016/j.cell.2012.03.037.

(101) Yang, B.; Chen, X.; Wang, Y.; Feng, S.; Pessino, V.; Stuurman, N.; Cho, N. H.; Cheng, K. W.; Lord, S. J.; Xu, L.; Xie, D.; Mullins, R. D.; Leonetti, M. D.; Huang, B. Epi-Illumination SPIM for Volumetric Imaging with High Spatial-Temporal Resolution. *Nat. Methods* **2019**, *16* (6), 501–504. https://doi.org/10.1038/s41592-019-0401-3.

(102) Kim, J.; Wojcik, M.; Wang, Y.; Moon, S.; Zin, E. A.; Marnani, N.; Newman, Z. L.; Flannery, J. G.; Xu, K.; Zhang, X. Oblique-Plane Single-Molecule Localization Microscopy for Tissues and Small Intact Animals. *Nat. Methods* **2019**, *16* (9), 853–857. https://doi.org/10.1038/s41592-019-0510-z.

(103) Sapoznik, E.; Chang, B. J.; Huh, J.; Ju, R. J.; Azarova, E. V.; Pohlkamp, T.; Welf, E. S.; Broadbent, D.; Carisey, A. F.; Stehbens, S. J.; Lee, K. M.; Marín, A.; Hanker, A. B.; Schmidt, J. C.; Arteaga, C. L.; Yang, B.; Kobayashi, Y.; Tata, P. R.; Kruithoff, R.; Doubrovinski, K.; Shepherd, D. P.; Millett-Sikking, A.; York, A. G.; Dean, K. M.; Fiolka, R. P. A Versatile Oblique Plane Microscope for Large-Scale and High-Resolution Imaging of Subcellular Dynamics. *Elife* **2020**, *9*, 1–39. https://doi.org/10.7554/eLife.57681.

(104) Latty, S.; Sakai, J.; Hopkins, L.; Verstak, B.; Paramo, T.; Berglund, N. A.; Gay, N. J.; Bond, P. J.; Klenerman, D.; Bryant, C. E. Activation of Toll-like Receptors Nucleates Assembly of the MyDDosome Signaling Hub. *Elife* **2018**, *7*, 1–16. https://doi.org/10.7554/eLife.31377.

(105) Hughes, C.; Choi, M. L.; Yi, J. H.; Kim, S. C.; Drews, A.; George-Hyslop, P. S.; Bryant, C.; Gandhi, S.; Cho, K.; Klenerman, D. Beta Amyloid Aggregates Induce Sensitised TLR4 Signalling Causing Long-Term Potentiation Deficit and Rat Neuronal Cell Death. *Commun. Biol.* **2020**, *3* (1). https://doi.org/10.1038/s42003-020-0792-9.

(106) Xia, Z.; Prescott, E.; Leah, T.; Dakin, H.; Dimou, E.; Zuo, E.; Zhang, Y. P.; Lam, J. Y. L.; Danial, J. S. H.; Jiang, H.; Mortiboys, H.; Thornton, P.; Crowther, D. C.;

Holtzman, D. M.; Ranasinghe, R. T.; Klenerman, D.; De, S. Co-Aggregation with Apolipoprotein E Modulates the Function of Amyloid-β in Alzheimer's Disease. *bioRxiv* **2021**, 2021.07.13.452239.

(107) Deliz-Aguirre, R.; Cao, F.; Gerpott, F. H. U.; Auevechanichkul, N.; Chupanova, M.; Mun, Y.; Ziska, E.; Taylor, M. J. MyD88 Oligomer Size Functions as a Physical Threshold to Trigger IL1R Myddosome Signaling. *J. Cell Biol.* **2021**, *220* (7). https://doi.org/10.1083/jcb.202012071.

(108) Sideris, D. I.; Danial, J. S. H.; Emin, D.; Ruggeri, F. S.; Xia, Z.; Zhang, Y. P.; Lobanova, E.; Dakin, H.; De, S.; Miller, A.; Sang, J. C.; Knowles, T. P. J.; Vendruscolo, M.; Fraser, G.; Crowther, D.; Klenerman, D. Soluble Amyloid Beta-Containing Aggregates Are Present throughout the Brain at Early Stages of Alzheimer's Disease. *Brain Commun.* **2021**, *3* (3). https://doi.org/10.1093/braincomms/fcab147.

(109) Laine, R. F.; Tosheva, K. L.; Gustafsson, N.; Gray, R. D. M.; Almada, P.; Albrecht, D.; Risa, G. T.; Hurtig, F.; Lindås, A. C.; Baum, B.; Mercer, J.; Leterrier, C.; Pereira, P. M.; Culley, S.; Henriques, R. NanoJ: A High-Performance Open-Source Super-Resolution Microscopy Toolbox. *J. Phys. D. Appl. Phys.* **2019**, *52* (16). https://doi.org/10.1088/1361-6463/ab0261.

(110) Ovesný, M.; Křížek, P.; Borkovec, J.; Švindrych, Z.; Hagen, G. M. ThunderSTORM: A Comprehensive ImageJ Plug-in for PALM and STORM Data Analysis and Super-Resolution Imaging. *Bioinformatics* **2014**, *30* (16), 2389–2390. https://doi.org/10.1093/bioinformatics/btu202.

(111) Legland, D.; Arganda-Carreras, I.; Andrey, P. MorphoLibJ: Integrated Library and Plugins for Mathematical Morphology with ImageJ. *Bioinformatics* **2016**, *32* (22), 3532–3534. https://doi.org/10.1093/bioinformatics/btw413.

(112) Andrews, C. S.; Miyata, M.; Susuki-Miyata, S.; Lee, B. C.; Komatsu, K.; Li, J. D. Nontypeable Haemophilus Influenzae-Induced MyD88 Short Expression Is Regulated by Positive IKKβ and CREB Pathways and Negative ERK1/2 Pathway. *PLoS One* **2015**, *10* (12), 1–15. https://doi.org/10.1371/journal.pone.0144840.

(113) Liew, F. Y.; Xu, D.; Brint, E. K.; O'Neill, L. A. J. Negative Regulation of Toll-like Receptor-Mediated Immune Responses. *Nat. Rev. Immunol.* **2005**, *5* (6), 446–458. https://doi.org/10.1038/nri1630.

(114) Lee, F. F. Y.; Davidson, K.; Harris, C.; McClendon, J.; Janssen, W. J.; Alper, S. NF-b

Mediates Lipopolysaccharide-Induced Alternative Pre-MRNA Splicing of Myd88 in Mouse Macrophages. *J. Biol. Chem.* **2020**, *295* (18), 6236–6248. https://doi.org/10.1074/jbc.RA119.011495.

(115) Björkbacka, H.; Fitzgerald, K. A.; Huet, F.; Li, X.; Gregory, J. A.; Lee, M. A.; Ordija, C. M.; Dowley, N. E.; Golenbock, D. T.; Freeman, M. W. The Induction of Macrophage Gene Expression by LPS Predominantly Utilizes Myd88-Independent Signaling Cascades. *Physiol. Genomics* **2005**, *19*, 319–330. https://doi.org/10.1152/physiolgenomics.00128.2004.

(116) Hobbs, S.; Reynoso, M.; Geddis, A. V.; Mitrophanov, A. Y.; Matheny, R. W. LPS-Stimulated NF-KB P65 Dynamic Response Marks the Initiation of TNF Expression and Transition to IL-10 Expression in RAW 264.7 Macrophages. *Physiol. Rep.* **2018**, *6* (21), 1–16. https://doi.org/10.14814/phy2.13914.

(117) Jaks, E.; Gavutis, M.; Uzé, G.; Martal, J.; Piehler, J. Differential Receptor Subunit Affinities of Type I Interferons Govern Differential Signal Activation. *J. Mol. Biol.* **2007**, *366* (2), 525–539. https://doi.org/10.1016/j.jmb.2006.11.053.

(118) Wilmes, S.; Beutel, O.; Li, Z.; Francois-Newton, V.; Richter, C. P.; Janning, D.; Kroll, C.; Hanhart, P.; Hötte, K.; You, C.; Uzé, G.; Pellegrini, S.; Piehler, J. Receptor Dimerization Dynamics as a Regulatory Valve for Plasticity of Type I Interferon Signaling. *J. Cell Biol.* **2015**, *209* (4), 579–593. https://doi.org/10.1083/jcb.201412049.

(119) Löchte, S.; Waichman, S.; Beutel, O.; You, C.; Piehler, J. Live Cell Micropatterning Reveals the Dynamics of Signaling Complexes at the Plasma Membrane. *J. Cell Biol.* **2014**, *207* (3), 407–418. https://doi.org/10.1083/jcb.201406032.

(120) Chmiest, D.; Sharma, N.; Zanin, N.; Viaris De Lesegno, C.; Shafaq-Zadah, M.; Sibut, V.; Dingli, F.; Hupé, P.; Wilmes, S.; Piehler, J.; Loew, D.; Johannes, L.; Schreiber, G.; Lamaze, C. Spatiotemporal Control of Interferon-Induced JAK/STAT Signalling and Gene Transcription by the Retromer Complex. *Nat. Commun.* **2016**, *7*. https://doi.org/10.1038/ncomms13476.

(121) Lamken, P.; Lata, S.; Gavutis, M.; Piehler, J. Ligand-Induced Assembling of the Type I Interferon Receptor on Supported Lipid Bilayers. *J. Mol. Biol.* **2004**, *341* (1), 303–318. https://doi.org/10.1016/j.jmb.2004.05.059.

(122) Stark, G. R.; Kerr, I. M.; Williams, B. R. G.; Silverman, R. H.; Schreiber, R. D. How Cells Respond to Interferons. *Annu. Rev. Biochem.* **1998**, *67*, 227–264.

https://doi.org/10.1146/annurev.biochem.67.1.227.

(123) De Weerd, N. A.; Vivian, J. P.; Nguyen, T. K.; Mangan, N. E.; Gould, J. A.; Braniff, S. J.; Zaker-Tabrizi, L.; Fung, K. Y.; Forster, S. C.; Beddoe, T.; Reid, H. H.; Rossjohn, J.; Hertzog, P. J. Structural Basis of a Unique Interferon-β Signaling Axis Mediated via the Receptor IFNAR1. *Nat. Immunol.* **2013**, *14* (9), 901–907. https://doi.org/10.1038/ni.2667.

(124) Jaitin, D. A.; Roisman, L. C.; Jaks, E.; Gavutis, M.; Piehler, J.; Van der Heyden, J.; Uze, G.; Schreiber, G. Inquiring into the Differential Action of Interferons (IFNs): An IFN-A2 Mutant with Enhanced Affinity to IFNAR1 Is Functionally Similar to IFN-β. *Mol. Cell. Biol.* **2006**, *26* (5), 1888–1897. https://doi.org/10.1128/mcb.26.5.1888-1897.2006.

(125) Marijanovic, Z.; Ragimbeau, J.; Van Der Heyden, J.; Uzé, G.; Pellegrini, S. Comparable Potency of IFNα2 and IFNβ on Immediate JAK/STAT Activation but Differential down-Regulation of IFNAR2. *Biochem. J.* **2007**, *407* (1), 141–151. https://doi.org/10.1042/BJ20070605.

(126) Weimann, L.; Ganzinger, K. A.; McColl, J.; Irvine, K. L.; Davis, S. J.; Gay, N. J.; Bryant, C. E.; Klenerman, D. A Quantitative Comparison of Single-Dye Tracking Analysis Tools Using Monte Carlo Simulations. *PLoS One* **2013**, *8* (5). https://doi.org/10.1371/journal.pone.0064287.

(127) Gurard-levin, Z. A.; Kilian, K. A.; Kim, J.; Ba, K. HaloTag a Novel Protein Labeling Technology for Cell Imaging and Protein Analysis. *ACS Chem. Biol.* **2010**, *60* (9), 45–58.